Master's Thesis

3D Analysis of MAGIC Boomerang Supernova Remnant Data Using Standardized Data Formats and Open-Source Analysis Tools

Department of Physics
Ludwig-Maximilians-Universität München

Carried out at University of Padua (MAGIC/CTA group)
In association to the INFN, Section of Padua, Italy

Marine Pihet

Supervised by Prof. Dr. Thomas Kuhr and Dr. Franca Cassol

Submitted in fulfillment of the requirements for the degree of M. Sc.

June 2024

Masterarbeit

3D-Analyse von MAGIC-Daten des Boomerang-Supernova-Überrestes unter Verwendung standardisierter Datenformate und Open-Source-Analysetools

Fakultät für Physik
Ludwig-Maximilians-Universität München

Ausgeführt an der Universität von Padua
In Affiliation mit dem INFN, Sektion von Padua, Italien

Marine Pihet

Betreut von Prof. Dr. Thomas Kuhr und Dr. Franca Cassol

Vorgelegt in Erfüllung der Voraussetzungen für den Abschluss M. Sc.

Juni 2024

Abstract

Charged Cosmic Rays (CRs) reach the Earth from all directions and are not correlated with the original source direction, due to deflection by intergalactic and Galactic magnetic fields. To find out what are their sources and which mechanisms are able to produce these highly energetic particles, neutral messengers such as γ-rays have to be employed. In this thesis, I analyzed archival MAGIC data of the Boomerang Supernova Remnant (SNR) PeVatron candidate, G106.3+2.7, with a novel 3D analysis method using standardized data formats and open-source analysis tools. The source has a complex comet-shaped structure and is commonly divided into a Head and Tail region, where the Head region is associated to the pulsar PSR J2229+6114 and its Pulsar Wind Nebula (PWN) G106.6+2.9. The 3D analysis technique is the most suitable method for extended-source analyses and more precise than the approach that was previously chosen for a published study by the MAGIC collaboration [76]. In the latter, G106.3+2.7 is found to exhibit a clear energy-dependent morphology, with a multi-TeV signal from the Tail region and indications for a related hadronic emission mechanism. First, I re-analyzed the dataset with the standard analysis software of MAGIC, the `MARS`, confirming the results from the paper. Then, I set up a 3D analysis pipeline including the computation of dedicated Instrument Response Functions (IRFs), the generation of background models with the open-source package `pybkgmodel` and the data reduction and modeling and fitting routines with `gammapy`. The pipeline was tested on the well-characterized Crab Nebula. This enabled the identification of two distinct systematic effects: an asymmetric feature in the background significance histogram at low energies and a systematic shift of the mean in the significance histograms of the background. The former of these could be reduced as a consequence. The reasonable spectral results I obtained validated the pipeline for usage on other sources. I find a Gaussian spatial model to be more probable than a point-like model for the description of the Crab Nebula. I provide the most stringent Upper Limit (UL) for extended emission of the Crab Nebula ever measured by the MAGIC telescopes, with a value of $\sigma = (0.0239 \pm 0.0008)\,^\circ$. It is not only compatible with previous measurements by the *Fermi*-LAT and H.E.S.S. experiments, but of the same order of magnitude, suggesting that it is on the verge of a detection. Finally, I report on the application of the 3D analysis pipeline to Boomerang SNR data. The morphological results obtained for G106.3+2.7 in this thesis are predominantly confirming

the findings of the previous publication, with a new hint at multi-TeV emission from the Head region. The spectral results of the 3D double symmetric Gaussian fits indicate a slightly harder index for the Head region than the 1D analysis of this work and the published work, while the indices for the Tail region are all very consistent. Furthermore, all spectral results are also in agreement with the related publication by MAGIC inside uncertainty intervals. A comparison of the quality of different spatial models indicates that the emission can reasonably be explained with two distinct symmetric Gaussian emission regions, the Head and the Tail region, or with a single asymmetric Gaussian region. The most important uncertainty in this analysis is introduced by the background estimation and modeling, and it is discussed in detail. This work demonstrates that the novel 3D analysis technique is developing into a powerful tool for the analysis of γ-ray data in several ways. With dedicated 3D background models, it enables to perform the analysis of complex emission regions with simultaneous spatial and spectral fitting and possibly to detect the extension of nearly point-like sources below the angular resolution limit of an instrument. Concluding, I offer several promising prospects of future research along the lines of work treated in this thesis.

Contents

Acronyms

ADC	Analog-to-Digital Converter
AGN	Active Galactic Nuclei
AIC	Akaike Information Criterion
AMC	Active Mirror Control
AMS	Alpha Magnetic Spectrometer
CGPS	Canadian Galactic Plane Survey
CMB	Cosmic Microwave Background
CoG	Center of Gravity
`CORSIKA`	COsmic Ray SImulations for KAscade
CR	Cosmic Ray
CTAO	Cherenkov Telescope Array Observatory
DC	Direct Current
DL0	Data Level 0
DL1	Data Level 1
DL2	Data Level 2
DL3	Data Level 3
DL4	Data Level 4
DL5	Data Level 5
dof	*degrees of freedom*
DRAO	Dominion Radio Astronomical Observatory
DRS4	Domino Ring Sampler 4
DT	Discriminator Threshold
EAS	Extensive Air Shower
EGRET	Energetic Gamma Ray Experiment Telescope
EM	Electromagnetic
`FITS`	Flexible Image Transport System

FoV	Field of View
GADF	Gamma Astro Data Formats
GBM	Gamma-Ray Burst Monitor
GRB	Gamma-Ray Burst
HAWC	High Altitude Water Cherenkov
HE	High-Energy
H.E.S.S.	High-Energy Stereoscopic System
IACT	Imaging Atmospheric Cherenkov Telescope
IC	Inverse Compton
IR	Infrared
IRAM	Institut de Radioastronomie Millimétrique
IRF	Instrument Response Function
ISM	Interstellar Medium
KASCADE	KArlsruhe Shower Core and Array DEtector
L0	Level 0 Trigger
L1	Level 1 Trigger
L3	Level 3 Trigger
LAT	Large Area Telescope
LHAASO	Large High Altitude Air Shower Observatory
LIDAR	LIght Detection And Ranging system
LST-1	Large-Sized Telescope 1
LUT	Lookup Table
M1	MAGIC 1
M2	MAGIC 2
MAGIC	Major Atmospheric Gamma-Ray Imaging Cherenkov
`MARS`	MAGIC Analysis and Reconstruction Software
MC	Monte Carlo
NN	Next Neighbor
NSB	Night Sky Background
NuSTAR	Nuclear Spectroscopic Telescope Array
ORM	Observatorio del Roque de los Muchachos
PDF	Probability Distribution Function
PMT	Photomultiplier Tube

PSF	Point Spread Function
PWN	Pulsar Wind Nebula
RF	Random Forest
RMS	Root Mean Square
SED	Spectral Energy Distribution
SM	Standard Model
SNR	Supernova Remnant
ST	Synthesis Telescope
SWGO	Southern Wide-Field Gamma-Ray Observatory
TS	Test Statistic
UHE	Ultra-High-Energy
UL	Upper Limit
UV	Ultraviolet
VERITAS	Very Energetic Radiation Imaging Telescope Array System
VHE	Very-High-Energy
WCD	Water Cherenkov Detector

Chapter 1

Introduction

Particle physics is a field dedicated to the study of fundamental particles and forces that make up the matter and radiation from which our Universe is built. So far, the Standard Model (SM) of particle physics is able to describe three of the four elementary forces, known to us: the electromagnetic, the weak and the strong interactions. On Earth, we are investigating the realm of the microcosm and probing the theory of the SM with powerful particle accelerators, that are however limited in the reachable energy. Although the Standard Model has proven to be successful in providing experimental predictions on Earth, e. g., the prediction of the later discovered Higgs boson [62, 1], it leaves some physical phenomena unexplained. It is thought that the SM acts as a low-energy limit for a more general and complete theory of particle interactions. This more fundamental model could manifest itself at energies above 10^{14} GeV [95]; energies which will never be attainable in laboratories on Earth but can be observed in highly energetic processes in the vast Universe. This is where astroparticle physics plays a central role, linking the very small to the very large.

One of many definitions of astroparticle physics goes as follows: astroparticle physics, like astrophysics, seeks to ascertain the nature of objects in our universe. However, the techniques of these two fields and the measured messengers are distinct. While astrophysics is mostly dealing with electromagnetic radiation, astroparticle physics is concerned with the measurement of Cosmic Rays (CRs), neutrinos and γ-rays [95]. In the broad domain of high-energy astroparticle physics, γ-rays have always been intimately connected to CRs. The latter are highly energetic charged and stable particles, mostly made up of protons and smaller percentages of heavy nuclei, electrons/positrons (e^+/e^-) and antiparticles. These are called primary CRs, whereas secondary CRs also include products of interaction and can therefore contain neutral particles, such as neutrinos and γ-rays [95]. γ-rays are the most energetic photons of the electromagnetic spectrum, starting around tens of MeV and extending up to a few PeV [29], as of current knowledge.

The reason for the connection between CRs and γ-rays is simple: Accelerated in the presence of strong magnetic fields in the environment of an astrophysical object, highly energetic CRs emit γ-ray radiation.

More than 100 years after the discovery of CRs, attributed to Victor Hess in 1912 [61], the production sites and acceleration mechanisms of highly energetic primary CRs are still a major unsolved question. This is because, compared to γ-rays, they are not carrying directional information any more when arriving at Earth, having been deviated by magnetic fields while traveling. It is therefore a challenging task to identify sources of CRs. To accomplish this, one first has to gain an understanding of the properties of CRs, which will be done in the first part of chapter 2. The second part will explain how the connection between CRs and γ-rays can be and has been exploited in this thesis, introducing the field of γ-ray astronomy and its detection techniques. In chapter 3, I will summarize the current knowledge about one potential CR accelerator that was treated in the presented work, the Boomerang Supernova Remnant (SNR) G106.3+2.7. The analysis of an extended Galactic source such as the mentioned SNR is a complex undertaking. Thus, in chapter 4, I will carefully define the faced challenge and explain the characteristics of the causing element, the background. Subsequently, the chapter will offer possibilities to handle that difficulty, presenting the methodology and software tools of the performed data analysis. In the main chapter of this thesis, chapter 5, I will report about the principal lines of work: the development of a 3D and 1D analysis pipeline, its test run on Crab Nebula data and its application to the Boomerang SNR. Results will be discussed and compared with other approaches and previous measurements, referring to G106.3+2.7 as a possible source of CRs. Finally, I will conclude with chapter 6 and give an outlook on possible studies to be conducted in the future, to contribute to the search for the origin of CRs.

Chapter 2

γ-Ray Astronomy

This chapter will convey the basics of γ-ray astronomy, starting with an introduction of the broader cosmic radiation from which the field is born. Then, I will introduce the sources, physical mechanisms and detection techniques of γ-ray astronomy. In the end, I will focus on one specific ground-based instrument: the Major Atmospheric Gamma-Ray Imaging Cherenkov (MAGIC) telescopes.

2.1 Cosmic Rays

There is a close connection between charged CRs and γ-rays originating in space. It lies in a shared origin. CRs accelerated in astrophysical environments of Galactic or extragalactic type are the parent particles for the production of γ-rays via radiative processes and particle interactions. Therefore, the properties of CRs and γ-rays are strongly coupled and knowledge of either of the two can be used to derive information about the other.

Since the discovery of CR radiation, attributed to Victor Hess in 1912 [61], the production sites and acceleration mechanisms of highly energetic primary CRs are a major unsolved question. As explained, this is because the charged primary CRs get deflected by Galactic and intergalactic magnetic fields on the way to Earth and do not directly point back to the source [95]. To solve the mystery of CRs and establish a link between incoming particles and the setting from which they emerge, neutral messengers like γ-rays or neutrinos are required. Since this work is concerned with γ-ray observations, the focus will lie on them here. Although γ-rays can be attenuated or absorbed on the way [95], they travel in a straight line and can reach our detectors carrying directional information about their origin. Using the direct link between the properties of highly energetic astrophysical photons and CRs, it becomes clear that measurements of γ-rays at Earth can help to infer characteristics of possible CR accelerators. Ultimately, follow-

ing the described detour, information from neutral messengers is believed to lead back to the origin of charged CRs.

The observed CR spectrum spans more than ten decades, extending up to several 10^{20} eV $= 10^{11}$ GeV, as shown in Fig. 2.1. Measurements by numerous experiments are

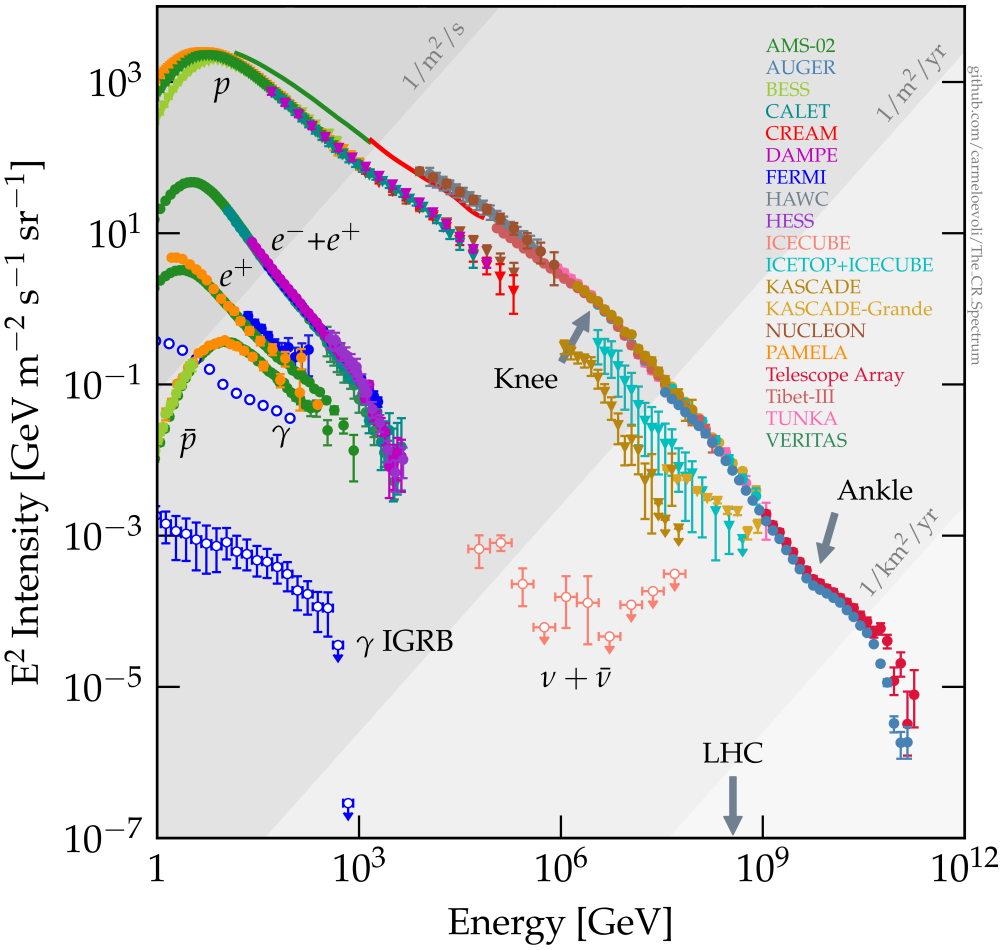

Figure 2.1: The CR spectrum 2023. A collection of measurements of the CR flux arriving at Earth, carried out by numerous experiments for high-energy astrophysics. The energy is given in GeV, the flux in GeV m^{-2} s^{-1} sr^{-1}. Spectra of individual components of the primary and secondary CR flux, such as protons, antiprotons, electrons, positrons, neutrinos, γ-rays, as well as the all-particle spectrum covering the whole range of energies are plotted. The *knee* and the *ankle* are indicated with gray arrows and labeled. From [42].

shown, among which AMS-02[1], the Pierre Auger Observatory[2], KASCADE[3], IceCube[4], HAWC[5], H.E.S.S.[6], VERITAS[7] and *Fermi*[8]. Some of these are able to distinguish the incoming particle type and measure the contribution of only one component of the overall CR spectrum. For instance, the flux of protons, antiprotons, electrons and positrons has been measured at energies between 1 GeV and 100 TeV, see Fig. 2.1. From there, it is evident that protons are the dominant particle type of CRs. The so-called CR all-particle spectrum corresponds to the spectral curve extending from low-energy measurements by AMS-02 (dark green) to the high-energy data points from the Pierre Auger Observatory (gray-blue) and the Telescope Array[9] (dark red). Two prominent features, called the *knee* and the *ankle*, according to their shapes, appear in the spectrum at several 10^{15} eV (PeV) and several 10^{18} eV (EeV), respectively. At the *knee*, the spectral index of the broken power law spectrum changes from ~ 2.7 to ~ 3.1 [95]. A definite physical explanation for the breaks, supported by observations, does currently not exist, although there are promising approaches. The two changes in the steepness of the power law spectrum are thought to be transitions between different kinds of emitters. Above the *ankle* the contributing sources are probably of extragalactic origin, as CRs of such high energy are not confined in our galaxy and improbable to reach us from Galactic objects. The *knee* on the other hand, could be explained by a population of Galactic CR emitters reaching their maximum acceleration capability around 10^{15} eV. Such a Galactic source, postulated to accelerate CRs up to PeV energies, is called a PeVatron source and it is the type of source we are looking for in the quest for the origin of Galactic CRs [95].

Having introduced CRs and some of their properties, we can now have a look at the current paradigm of potential PeVatron candidates. There are several good arguments suggesting the SNR population of the Milky Way to represent at least a significant fraction of the postulated PeVatron sources. SNRs are the shell-like leftovers of stellar explosions, either triggered by the core collapse of a massive star or by a white dwarf accreting material from a companion star and exceeding a critical mass limit, making it unstable against collapse. The material ejected from the explosion is transported by an expanding shock wave of high speed which propagates through the ambient medium [95]. It poses a suitable environment for particle acceleration in the first hundred to thousand years, following the disruption [18]. The arguments for SNRs as PeVatron candidates are the following:

- SNRs provide sufficient kinetic energy per explosion and a sufficient explosion rate (a few per century in the whole galaxy) to sustain the energy budget of the

[1] https://ams02.space/
[2] https://www.auger.org/
[3] https://cr.iap.kit.edu/kascade/
[4] https://icecube.wisc.edu/
[5] https://www.hawc-observatory.org/
[6] https://www.mpi-hd.mpg.de/HESS/
[7] https://veritas.sao.arizona.edu/
[8] https://fermi.gsfc.nasa.gov/
[9] http://www.telescopearray.org/

observed CR flux. The latter has been observed to be stable over several decades. This means that there has to exist a compensatory process to the loss of CRs due to their escape out of the Milky Way via diffusion. The kinetic energy provided by the shock waves of SNRs, created several times per century, is sufficient to accelerate the amount of new particles necessary to keep the flux of CRs at Earth constant. It is therefore realistic to assume that this could be the balancing process.

- Conditions for an effective acceleration mechanism of particles, the first-order Fermi acceleration, are fulfilled inside of the expanding shock front of SNRs [95]. Fermi, in 1949, realized that particles can be accelerated by collisions with moving clouds of gas [45]. The process is called second-order Fermi acceleration, due to its quadratic dependence on the cloud velocity. Some years later he refined his theory, and discovered a more efficient mechanism depending linearly on the cloud velocity, the first-order Fermi acceleration [44]. Being related to the shock front of astrophysical violent events, it is also called diffusive shock acceleration.

- With the given acceleration capabilities, the remnants have a maximum attainable energy for accelerated protons around several hundred TeV, close to the *knee* of the CR spectrum, as derived in section 6.4. of [95].

- The spectral index of the energy spectrum of particles accelerated within the framework of the diffusive shock acceleration model can be estimated following the work of Longair [74]. It was found that acceleration in SNR shock waves produces a power law particle spectrum with spectral index ~ 2. The latter is in agreement with the measured CR spectrum.

A particular SNR and PeVatron candidate has been the topic of this master's thesis and will be introduced in chapter 3. Before, I will give an overview of the field of γ-ray astronomy.

2.2 Very-High-Energy γ-Rays

γ-rays make up the most energetic part of the electromagnetic spectrum and are produced by various astrophysical sources that have enough power to accelerate particles beyond the X-ray regime. They can roughly be divided into three different energy ranges:

- **High-Energy (HE)**: tens of MeV to 100 GeV
- **Very-High-Energy (VHE)**: 100 GeV to 100 TeV
- **Ultra-High-Energy (UHE)**: above 100 TeV

This section is dedicated to the introduction of γ-ray emitting sources, ongoing production mechanisms and the detection techniques employed by space-borne and ground-

based detectors to directly and indirectly observe such sources.

2.2.1 Sources of Very-High-Energy γ-Rays

Generally, sources of VHE γ-rays can be divided into two categories: Galactic and extragalactic sources. Among the Galactic sources there are pulsars (fast-rotating neutron stars) and their Pulsar Wind Nebulae (PWN), γ-ray binary systems (interacting binary systems with a star and a heavy object, such as a neutron star or black hole) and SNRs. SNRs are usually surrounding a pulsar or black hole, created during the supernova explosion, and featuring a slowly expanding shock front made of ejecta material from the explosion. In the first thousands of years after a supernova, the developing remnant is a suitable environment for particle acceleration and γ-ray production, before the density of particles and their energy becomes too low for efficient γ-ray emission mechanisms to take place [18]. The most abundant type of extragalactic sources seen in γ-rays are various representatives of Active Galactic Nuclei (AGN). These are the center of galaxies, composed typically of a supermassive black hole and other material surrounding it, structured in different elements such as the accretion disk and the powerful jets, mostly oriented perpendicularly to the accretion plane [101, 27]. Based on the viewing angle of the jet, AGN are classified into different subclasses, of which blazars are the most prominent ones. Their jet is directly pointing towards Earth, rendering their detection more favorable than representatives of other classes of AGN. Apart from that, there are starburst galaxies and transient extragalactic events that can be observed by γ-ray experiments, for instance the afterglow emission of a Gamma-Ray Burst (GRB).

2.2.2 Production of γ-Rays

In astrophysical source environments there are four main kinds of processes leading to the production of γ-rays, each of them either of leptonic or hadronic nature, based on the particle type emitting them:

- **Synchrotron Radiation** (a in Fig. 2.2): In the presence of a magnetic field charged particles are accelerated on curved tracks and emit photons. This electromagnetic emission is called synchrotron radiation and is predominantly coming from electrons in the environment of an astrophysical source.

- **Bremsstrahlung** (b in Fig. 2.2): Again predominantly emitted by electrons, bremsstrahlung is produced when a charged particle interacts with the Coulomb field of an atomic nucleus. For light particles, the emissivity of such electromagnetic radiation is higher than for heavy particles, since the process' efficiency is inversely proportional to the mass squared of the particle.

- **Inverse Compton (IC) scattering** (c in Fig. 2.2): The diagram depicts an up-scattering of a low-energy photon (for instance from the Cosmic Microwave Background (CMB)) on a high-energy electron that was accelerated up to γ-ray energies by accelerating processes in the source environment. This leptonic process

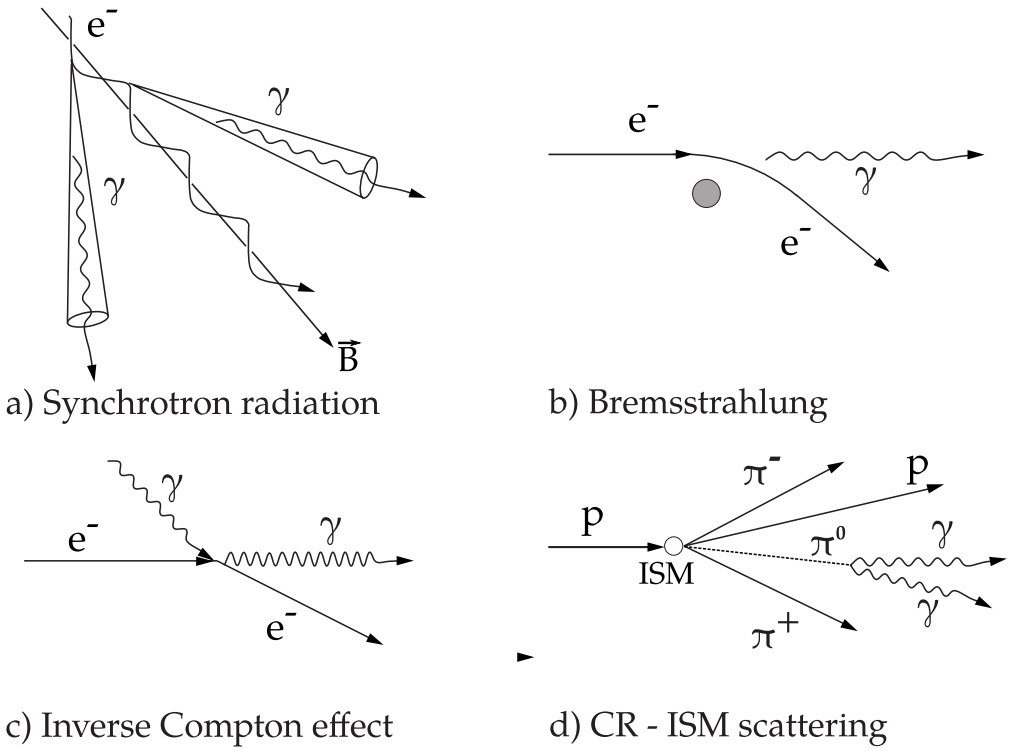

Figure 2.2: γ-ray production mechanisms of leptonic and hadronic nature. Synchrotron radiation (a), bremsstrahlung (b), and the Inverse Compton effect (c) are predominantly involving leptons, while the scattering of accelerated CRs on molecules in the ISM (d) is a hadronic process. From [96].

is known as IC scattering and transforms kinetic energy of the electron into photon energy of the γ-ray.

- π^0-**Decay** (d in Fig. 2.2): VHE photons can also be produced via hadronic interactions. Similar to electrons, a source with enough energy budget can accelerate hadronic particles, mostly protons, to VHE energies. When these particles collide with protons from the Interstellar Medium (ISM), such as found in cold molecular clouds, hadron-nucleon or proton-proton (pp) interactions result in the creation of charged (π^+/π^-) and neutral pions (π^0). The neutral ones immediately decay into two γ-ray photons of half the π^0 energy.

2.2.3 Detection Principles

Fig. 2.3 gives an overview over the field of astroparticle physics. Produced at the source or in the source environment, various messengers, such as CRs, γ-rays and neutrinos (in blue, green and red in Fig. 2.3) travel towards the Earth. While traveling, charged particles and γ-rays are subject to absorption and attenuation by dust clouds (in the

source region or in the interstellar environment). Note that the crucial feature of γ-rays (and neutrinos) is their neutrality. Missing charge accounts for their straight propagation in space, undisturbed by the influence of intergalactic magnetic fields, compared to charged CRs (see curved blue tracks in Fig. 2.3). Once reaching the Earth, particles and light can be detected by dedicated instruments, located in space (satellites), on the ground (Cherenkov telescopes or air shower arrays) or underground (large-volume detector arrays). Apart from the various instrument designs, the section will introduce the concept of Cherenkov radiation, and the imaging technique of a ground-based type of detector referred to as Imaging Atmospheric Cherenkov Telescope (IACT).

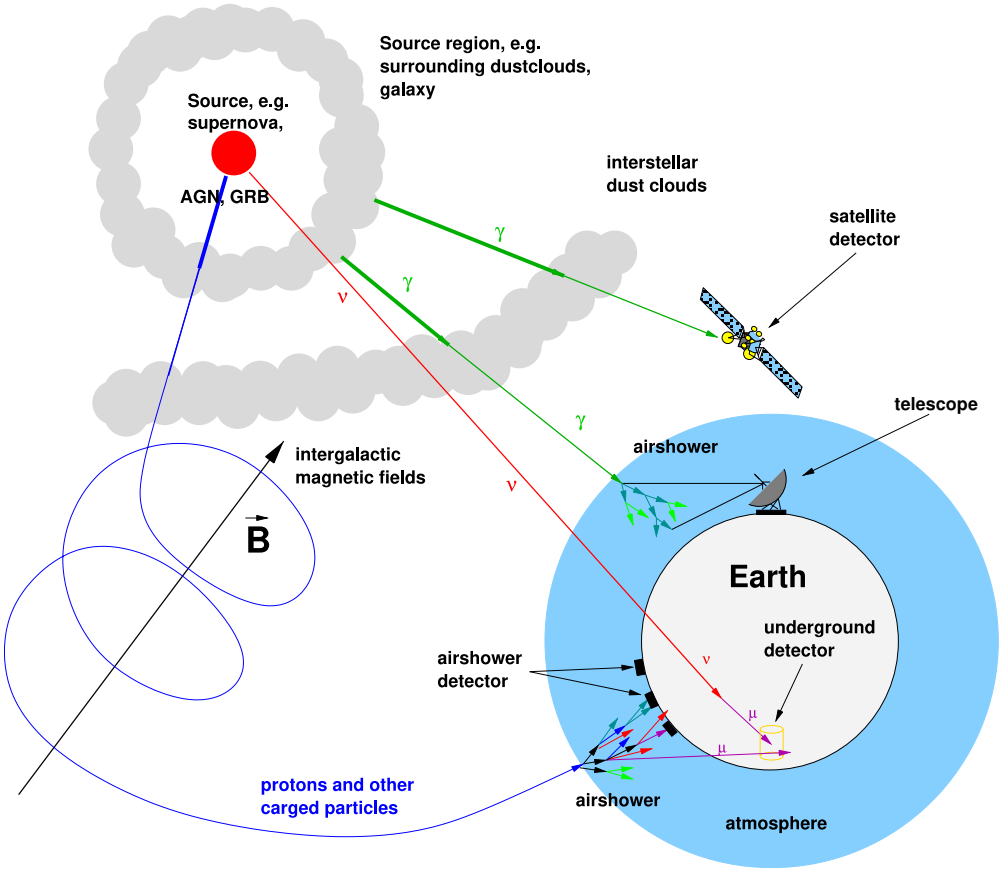

Figure 2.3: Illustration summarizing the field of astroparticle physics. Produced at the source or in the source environment, various messengers, such as CRs (blue), γ-rays (green) and neutrinos (red) travel towards the Earth until they are detected by one of the dedicated instruments, located in space (satellites), on the ground (Cherenkov telescopes or air shower arrays) or underground (large-volume detector arrays). Charged particles and γ-rays can be absorbed or attenuated by dust clouds in the source region or while traveling to the Earth. In addition, CRs are deviated by intergalactic magnetic fields. From [104].

2.2.3.1 Space-Based γ-Ray Astronomy

Direct interaction between a γ-ray and a detector (direct detection) is only possible if the experiment is located in space, due to the absorption of γ-rays in Earth's atmosphere. Currently, the most impactful mission, is the satellite *Fermi*[10] [17], hosting two instruments on board with the Gamma-Ray Burst Monitor (GBM)[11] and the *Fermi* Large Area Telescope[12] (*Fermi*-LAT). The former is dedicated to the discovery and study of GRBs, whereas the latter executes a continuous monitoring program of the sky. Hereby, the LAT is able to cover the whole sky in three hours due to its wide Field of View (FoV) (equal to 20 % of the entire sky). γ-rays are detected inside the instrument in two stages. The first is a precision converter-tracker, which triggers pair production of an e^+e^- pair and reconstructs the shower particles' path to extract directional information about the photon; the second is a calorimeter for energy determination, surrounded by an anti-coincidence detector to reject CR background events. The instruments sensitivity spans the energy range from around 20 MeV to 300 GeV, establishing a link and overlap region with the higher energy range of ground-based instruments for γ-ray astronomy. Therefore, the two kinds of instruments play an important role in mutually confirming and completing each others scientific findings.

2.2.3.2 Cherenkov Radiation

As visualized in Fig. 2.4, a charged particle moving in a dielectric medium temporarily polarizes the medium molecules along its path. This can lead to the emission of an electromagnetic (EM) type of radiation called Cherenkov radiation (bottom panels in Fig. 2.4), discovered by Čerenkov (in English adapted to Cherenkov) [32], if the relation

$$v = \beta c > c_{medium} = \frac{c}{n} \tag{2.1}$$

is fulfilled. v is the velocity of the particle, c is the speed of light in vacuum and c_{medium} is the speed of light in a medium of refractive index n. In both scenarios, surrounding molecules are polarized (top left and bottom left in Fig. 2.4) and generate wavelets of electromagnetic dipole transitions (top right and bottom right in Fig. 2.4) when returning to their original state. However, in the bottom setup, the single wavelets interfere constructively and create a wavefront that leads to the emission of Cherenkov radiation. Due to the geometric properties of the polarization propagation, it is emitted only under a specific angle θ and propagates in form of a conical-shaped wavefront (bottom right panel in Fig. 2.4). Cherenkov radiation lies in the blue and Ultraviolet (UV) regime of the spectrum.

[10] https://fermi.gsfc.nasa.gov/
[11] https://gammaray.nsstc.nasa.gov/gbm/
[12] https://glast.sites.stanford.edu/

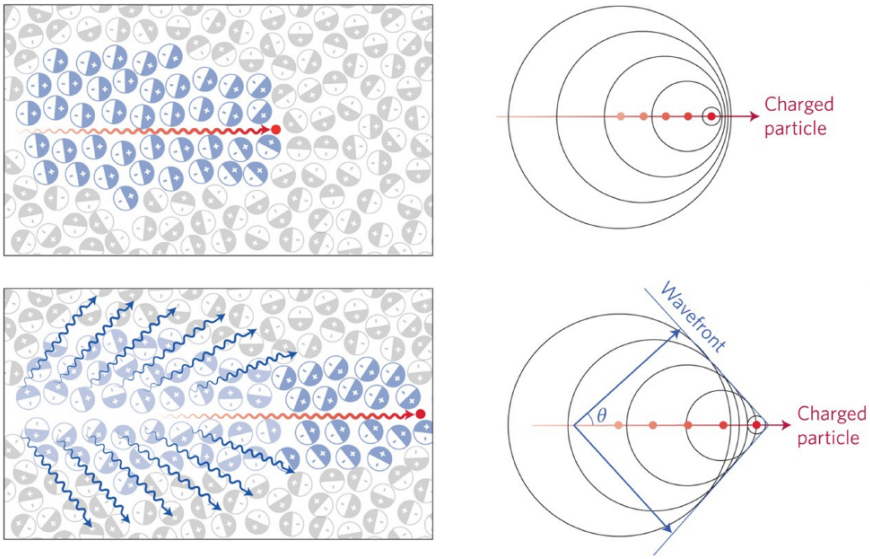

Figure 2.4: A charged particle moving inside a dielectric medium. Top panels display the particle's passage with a velocity smaller than the phase velocity of light in the medium $v < c_{medium}$. Bottom panels show the complementary case with $v > c_{medium}$. From [92].

2.2.3.3 Ground-Based γ-Ray Astronomy

Above 100 GeV, the γ-ray flux decreases rapidly and makes large detector volumes necessary for a detection, larger than volumes that can be accommodated on satellites nowadays. Hence, γ-rays can be detected by space-based experiments only up to certain energies. Beyond that, the atmosphere itself, opaque to γ-rays due to its absorbing properties, can be used as a detector volume and instruments become ground-based, relying on indirect detection methods.

If not detected in space, VHE photons as well as incoming relativistic CR particles interact with molecules in Earth's atmosphere and initiate a cascade of processes, thereby producing further particles and radiation [50, 51]. The multiplication of particles ends when the individual energy of the particles reaches a critical value. Any such air shower is generally referred to as Extensive Air Shower (EAS). Based on the nature of the primary particle, and by consequence the properties of the shower, EAS are differentiated into electromagnetic showers (initiated by γ-rays or electrons/positrons) and hadronic showers (initiated by protons or heavier nuclei), as depicted in Fig. 2.5. The left particle avalanche in Fig. 2.5 is induced by a γ-ray and grows to a shower of electrons/positrons and γ-rays through pair production of e^+/e^- and emission of bremsstrahlung by the leptons. The shower is approximately of ellipsoidal shaped. In the second case (right in Fig. 2.5), the participating particles and processes are more variegated. The initiating particle is a CR, for instance a proton, α-particle, or other heavy nucleus. The secondary products include particles of the same type, as well as muons, pions and Electromagnetic

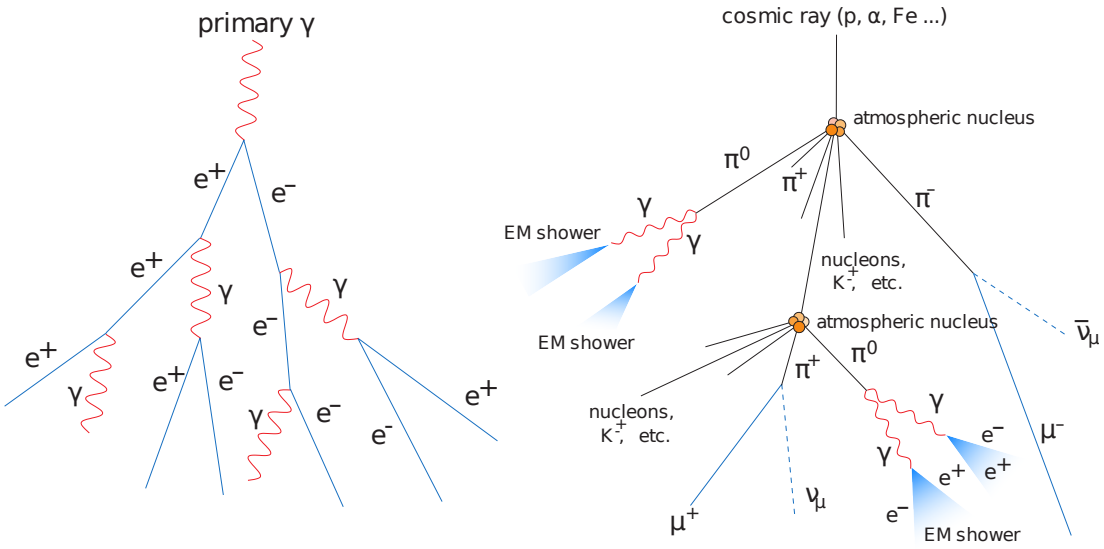

Figure 2.5: Illustration of an EM (left) and a hadronic (right) air shower, induced by a γ-ray and CR, respectively. In the first case the particle avalanche of electrons/positrons and γ-rays is initiated by a γ-ray or electron and grows through pair production of e^+/e^- and emission of bremsstrahlung by the leptons. In the second case, where the diversity of participating particles and processes is larger, the initiating particle can be any CR, including protons, α-particles, or other heavy nuclei. The secondary products are of the same particle type, as well as muons, pions and through π^0-decay into two γ-rays also EM subshowers. From [103].

(EM) subshowers from π^0-decays. The hadronic shower is characterized by a large lateral extension due to the transmission of transverse momentum of particles through collisions. It has a less regular shape as an EM shower.

Due to the very energetic primary γ-rays or particles, secondary products of interactions in the shower receive enough kinetic energy to exceed the phase velocity of light in air and produce the aforementioned Cherenkov radiation. This essential process enables indirect observations of γ-rays by IACTs and is also employed by EAS arrays, e. g., Water Cherenkov Detectors (WCDs). For an EM shower, the individual ring-shaped emission of Cherenkov light by single leptonic particles superposes to generate a circular light pool on Earth's surface. How IACTs, located inside the cone of light, can image the Cherenkov flashes of showers will be explained in the next section.

Compared to IACTs, EAS array experiments are able to directly intercept the particles of the shower, due to their placement at high-altitudes ($\sim 4000\,\mathrm{m}$ a.s.l.). WCDs, consisting of large volumes of purified water, provide a medium for the generation of Cherenkov light by charged particles of EAS and its subsequent detection. Among the currently

active EAS arrays, there are the High Altitude Water Cherenkov (HAWC)[13] [93] and Large High Altitude Air Shower Observatory (LHAASO)[14] [28] detectors. Both of them have studied the source of interest of this thesis, the Boomerang SNR, as we will see in chapter 3. The future Southern Wide-Field Gamma-Ray Observatory (SWGO)[15] [9] will further push current limits of sensitivity and make accessible new parts of the sky as seen by WCDs, being the first large-sized EAS array projected for the Southern hemisphere of the Earth [65]. SWGO will cover an area of $220,000\,\mathrm{m}^2$, corresponding to ten times the surface operated by HAWC.

At present, there are also three major IACT arrays in operation:

- The Very Energetic Radiation Imaging Telescope Array System (VERITAS)[16] [106] is an array of four 12 m telescopes, located at the Fred Lawrence Whipple Observatory in Arizona, USA. Its most sensitive energy band spans from 100 GeV to 10 TeV, while its FoV is 3.5 ° wide.

- The High-Energy Stereoscopic System (H.E.S.S.)[17] [64] comprises five telescopes of two different sizes and mirror dish shapes, stationed in Namibia, Africa. The original four IACTs have hexagonal mirror dishes and measure 12 m in diameter, while the more recently integrated central rectangular reflector has an equivalent circular diameter of 28 m. They have FoVs of 5 ° and 3.2 °, respectively.

- MAGIC provided the data for the presented work and will be introduced in section 2.3.

The future of Cherenkov telescopes is represented by the next-generation Cherenkov Telescope Array Observatory (CTAO)[18] [34], the northern array (CTAO-North) of which is starting to be deployed at its site in La Palma, a few meters from the MAGIC telescope site. It will be completed by a second array in the southern hemisphere (CTAO-South).

2.2.3.4 Imaging Technique of IACTs

The imaging technique of IACTs has its roots in a first investigation by Galbraith and Jelley in 1953 [52]. They discovered the potential of this method, installing a single Photomultiplier Tube (PMT) above a parabolic mirror and measuring a correlation between the signal from light pulses and incoming CRs. After that and until the first detection of a source by the Whipple telescope located in Arizona [105], more than three decades passed, in which the technique was explored and improved.

[13] https://www.hawc-observatory.org/
[14] http://english.ihep.cas.cn/lhaaso/
[15] https://www.swgo.org/
[16] https://veritas.sao.arizona.edu/
[17] https://www.mpi-hd.mpg.de/hfm/HESS/
[18] https://www.ctao.org/

As illustrated in Fig. 2.6, an IACT with its reflector dish and PMT camera, images both EM (label 1, 2 and 3 in Fig. 2.6) and hadronic showers (label 0 in Fig. 2.6), seen via their emitted Cherenkov radiation. While EM cascades have regular elliptical (2 and 3 in Fig. 2.6) or circular (1 in Fig. 2.6) shapes in the imaging camera, hadronic cascades of particles exhibit more complex irregular shapes (0 in Fig. 2.6), typically characterized by patches of different size and intensity. The precise shape and orientation of the shower image is based on the viewing angle under which the shower is seen by the IACT. A circular light spot (1 in Fig. 2.6) is detected by the camera if the shower development (dashed blue line in Fig. 2.6) happens on the optical axis of the telescope. In the case

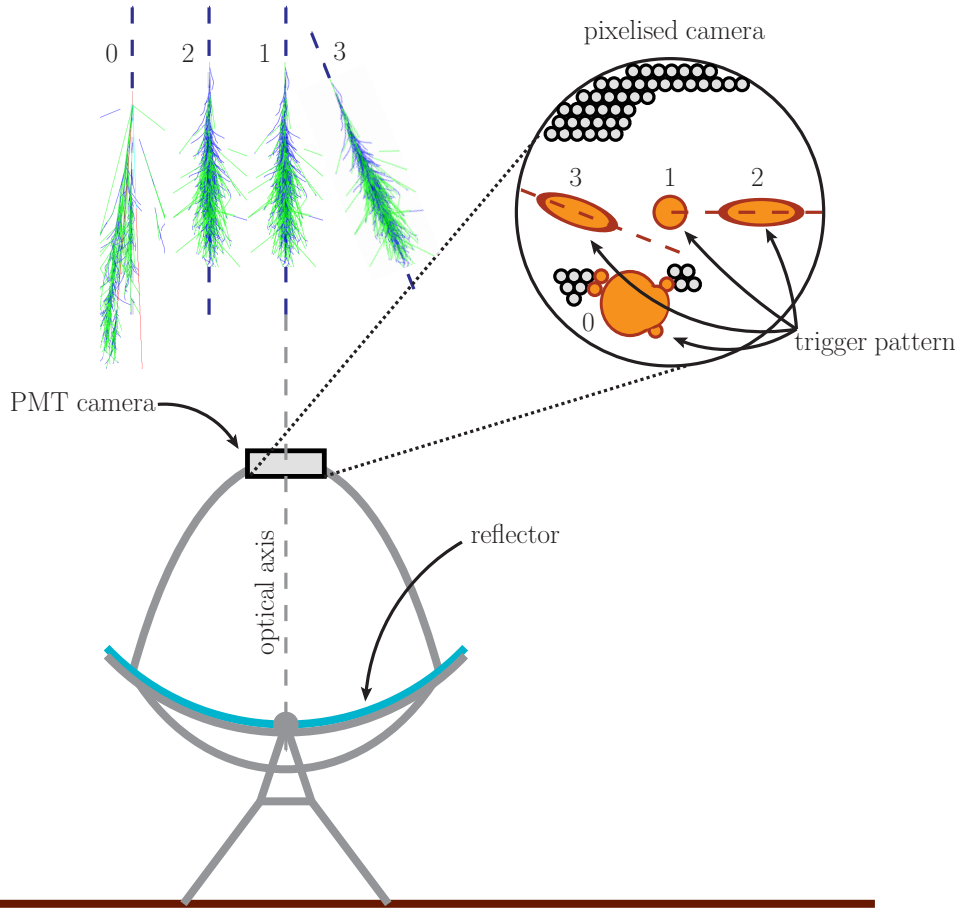

Figure 2.6: Schematization of the imaging technique of IACTs. γ-ray showers (1, 2, 3), developing inside the FoV of a Cherenkov telescope, cause regular elliptical patterns in the pixelised PMT camera. CR showers (0) produce patched irregular images, due to the numerous EM subshowers and the involved muonic particles. The image patterns of the four shower examples are represented by orange shapes in the camera, and labeled accordingly. From [84].

of a development parallel to the optical axis, the recorded light pool has an elliptical pattern and a major axis (dashed brown line in the camera image of Fig. 2.6) crossing the camera center (2 in Fig. 2.6). For a misaligned shower axis (3 in Fig. 2.6), the elliptical image is oriented in such a way for its principal axis to not intercept the center of the detector. Due to the above explained geometry of the imaging technique, the major axis of an elliptical shower image points back to the sky location of the γ-ray emitting source inside the camera FoV. IACTs typically observe in the stereoscopic mode. If the Cherenkov light pool of an EAS shower hits the entire IACT array, several telescopes record the same Cherenkov flash from different viewing angles. Combining the multiple recorded shower images, one can estimate the directional origin of the γ-ray. It corresponds to the interception point of the major axes of the shower, in the case of MAGIC seen by two telescopes. This is called stereoscopic direction reconstruction and employs an image parametrization technique called Hillas parametrization, introduced by Hillas [63]. It defines a set of geometrical quantities to characterize the elliptical shower images, the most important ones of which are listed here:

- *Size*: Total charge content of a shower in number of photoelectrons.
- *Length* and *width*: Indicators of Root Mean Square (RMS) spread of the signal parallel and perpendicular to the cluster major axis.
- *Center of Gravity (CoG)*: Centroid position of the weighted mean signal in the camera.
- *Distance*: Distance of the *CoG* to the expected source position in the detector FoV.

Given that the Hillas parameters on average differ for γ-ray- and hadron-induced shower images, they are also used as a major indicator for γ/hadron separation (see section 4.3.1).

2.3 The MAGIC Telescopes

The Major Atmospheric Gamma-Ray Imaging Cherenkov (MAGIC) telescopes (MAGIC 1 and MAGIC 2) are two IACTs with a diameter of 17 m each, based at the Observatorio del Roque de los Muchachos (ORM) at $\sim$ 2200 m altitude on the Canary Island of La Palma, Spain (see Fig. 2.7). While the initial design report for an array of two IACTs dates back to 1998 [20], the first telescope was commissioned in 2003. MAGIC 1 (M1) carried out scientific observations in standalone mode (mono mode) until 2009. After that, MAGIC 2 (M2), assembled 85 m apart from M1, started operating and the system was ready for the stereoscopic mode of scientific observations [13]. In 2011 and 2012, it underwent a major revision involving the camera and trigger of M1 and the full readout system, upgrading the performance and unifying the components of the telescopes [14]. The MAGIC telescopes operate between tens of GeV and tens of TeV, reaching a lower energy threshold of 50 GeV [15]. The following section is dedicated to a description of

the hardware components and the data taking mode of MAGIC.

2.3.1 Hardware

The MAGIC 1 and MAGIC 2 telescopes both rely on an Alt/Az mount, consisting of a steal base structure for stability and a rail system for positioning the telescopes with a pointing accuracy of $< 0.02\,^\circ$ [24]. The segmented 17 m reflector dish of each telescope is installed on a light-weight support frame, made of carbon-fiber tubes and therefore weighing only ~ 5.5 t. 247 individual square spherical-curved tiles measuring $1\,\mathrm{m}^2$ make up the tessellated parabolic mirror, resulting in a focal length f equal to the diameter $\mathrm{D} = \mathrm{f} = 17\,\mathrm{m}$. Each of the segments is mounted on three fastening points, of which one is fixed and two are movable actuators featuring step motors to focus the mirror segment to its assigned position in the camera. The Active Mirror Control (AMC) subsystem [22] acts on these individual motors to focus the telescope on a whole and counteract the weight-induced zenith-dependent deformation of the carbon-fiber structure during

Figure 2.7: The two Major Atmospheric Gamma-Ray Imaging Cherenkov (MAGIC) telescopes, on site at around ~ 2200 m altitude on the Canary Island of La Palma. They represent one of the three worldwide currently operative IACT arrays. Each telescope features a reflector dish of 17 m diameter, supported by a light-weight structure and connected to a PMT-based camera via an arc. Photo from `https://magic.mpp.mpg.de/gallery/pictures/tn/IMG_2520.JPG.html`.

the telescope movement.

In the focal point of the reflector sits the camera of approximately circular shape (see Fig. 2.8) with a FoV of 3.5 °. It is composed of 1039 individual Photomultiplier Tube (PMT) pixels that are grouped in clusters of seven (see thick black lines in Fig. 2.8), enclosed by an aluminum housing. To entirely fill the camera plane, each of the round PMTs is equipped with a hexagonal light-guiding Winston cone. Moreover, this has the advantageous effect of suppression of stray light during observations. The camera's total weight measures $\sim$ 850 kg and it is held in position by an aluminum arc. The latter is completed by another 180 ° arc behind the structure, acting as a rail for the altitude movement and powered by a central motor below the reflector dish. Steel cables connecting the camera to the dish structure stabilize the construction.

Conclusively summing the individual components' weight, one telescope weighs less than 70 t. Therefore, MAGIC can perform a rotation of 180 ° in azimuth in less than $\sim$ 25 s, which was projected and realized with the intention of enabling fast repositioning of the telescopes to catch the emission of short-duration transient events such as GRBs. 15 years after the construction of M1, the first event of such nature was incontrovertibly detected when MAGIC observed significant TeV emission of GRB 190114C [80, 75].

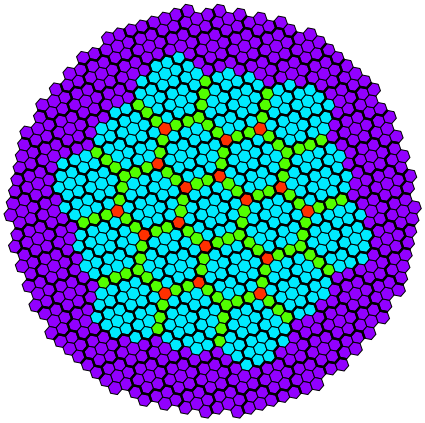

Figure 2.8: Layout of the circular-shaped PMT camera of MAGIC, constructed from 1039 individual round PMTs. The PMTs are vested with hexagonal light-guiding Winston cones to maximize the light collection area by filling the whole camera plane. They are grouped in clusters of seven (thick black hexagons). The hexagonal region enclosed by the purple pixels is the trigger region. Inside it, there are 19 overlapping macrocells (cyan hexangons), each of which contains 37 pixels. Pixels belonging to two (three) macrocells are highlighted in green (red). From [14].

In order to reject spurious events from the Night Sky Background (NSB) (stars, the Moon, and other natural or artificial light sources) the readout electronics of the experiment are equipped with three levels of trigger [14]:

- Level 0 Trigger (L0): An L0 is issued, when the signal in a single PMT exceeds a (programmable) Discriminator Threshold (DT). The default DT is $\sim$ 5 photoelectrons for extragalactic sources and scaled up by 15 % for Galactic sources [14]. The event rate for this trigger level is $\sim$ 800 kHz.

- Level 1 Trigger (L1): The L1 evaluates the signal of n compact Next Neighbor (NN) pixels on a grid of 19 overlapping macrocells (see Fig. 2.8), and triggers

if it finds an L0 for all n neighbors. During standard stereo observations, the trigger operates with 3NN multiplicity, although 2NN and 4NN (for mono mode observations) are also implemented. The typical rate is reduced to $\sim$ 15 kHz [14].

- Level 3 Trigger (L3): The stereoscopic L3 takes as input the L1 of both telescopes, expands the signal time windows to 100 ns width and delays them, based on the changing telescope pointing, in order to match the events recorded by M1 and M2. If the search for a coincident signal is successful, the readout is activated and saves the corresponding event. This final readout trigger happens at a rate of $\sim$ 250 - 350 Hz [14].

During offline analysis the trigger rates recorded for each observation run can be used to apply a selective cut on the data, based on expected rates. Thus, data strongly affected by moon light or including accidental triggers, e. g., from car flashes[19] can be rejected.

A Domino Ring Sampler 4 (DRS4) chip represents the core element of the MAGIC readout system (specifications can be found in [94, 23]). It is a ring buffer with a cycle of $\sim$ 200 ns storing PMT pulses in an analogue memory with a sampling frequency of 1.64 GSample/s. Only in case of an issued L3 trigger the memory is read out and the corresponding event is saved before being overwritten by the ring sampler. The dead time of the readout after the upgrade in 2012 is 27 μs [14]. The offline analysis chain of MAGIC (see section 4.3.3) applies a correction for that dead time, calculating the effective observation time.

The operating system of MAGIC also comprises several subsystems, of which one will be mentioned here for later reference:

- The LIght Detection And Ranging system (LIDAR) [47] is a 60 cm optical reflector telescope with an integrated laser, operated simultaneously to stereoscopic observations. Following the pointing direction of MAGIC while shooting, the laser light back scatters on aerosols and air molecules in the atmosphere and is redetected by the LIDAR's camera sensor. By this means, the atmospheric absorption and scattering effects affecting both the back-scattered laser light and the Cherenkov light from EAS can be quantified with a transmission value. The transmission measurements can be used to select good quality data and improve the energy reconstruction of the primary γ-rays.

2.3.2 Data Taking

Initially, IACTs were conducting observations exclusively in ON/OFF mode. It designates a strategy in which data is acquired pointing directly to the source (ON) and additionally pointing to a source-free region in the sky (OFF), from which the back-

[19] With car flashes, we refer to temporary strong increases of the trigger rates due to the (partly) illumination of telescope camera or reflector plane by cars passing by the ORM site during night.

ground rate can be determined. Observation times of ON and OFF should be similar in duration. The ON/OFF mode holds the risk to record data with non-matching observing conditions and loose the ability to correctly estimate the background. Additionally, a fundamental disadvantage of such an approach is the significant loss of observation time during OFF data taking, that could be spent on VHE sources. Especially intervals of so-called dark time, where the moon is absent, represent valuable observation time for the detection of the faint Cherenkov flashes from γ-rays. Today, the method has largely been replaced by wobble mode observations (see Fig. 2.9), also implemented by the MAGIC telescopes. During data taking the stereoscopic system is centered on a sky location offset from the expected source position (by $\sim 0.4\,^\circ$ during standard observations) and changing wobble position after each run of 20 min duration. On the left side of Fig. 2.9, the pattern of observations generated by wobbling around the source (black star) is shown for the case of four wobble positions (W1, W2, W3 and W4), indicated along with the respective FoVs. The corresponding wobble angles are $0\,^\circ$, $180\,^\circ$, $90\,^\circ$ and $270\,^\circ$. To give an example for later reference, a wobble position that is offset from the source by $0.5\,^\circ$ and has a wobble angle of $270\,^\circ$ can be written in the notation W0.50+270. The new strategy eliminates the need for dedicated OFF observations, as it leaves half of the camera without source for simultaneous background estimation. On the right panel of Fig. 2.9, three OFF regions on the source-free part of the FoV are indi-

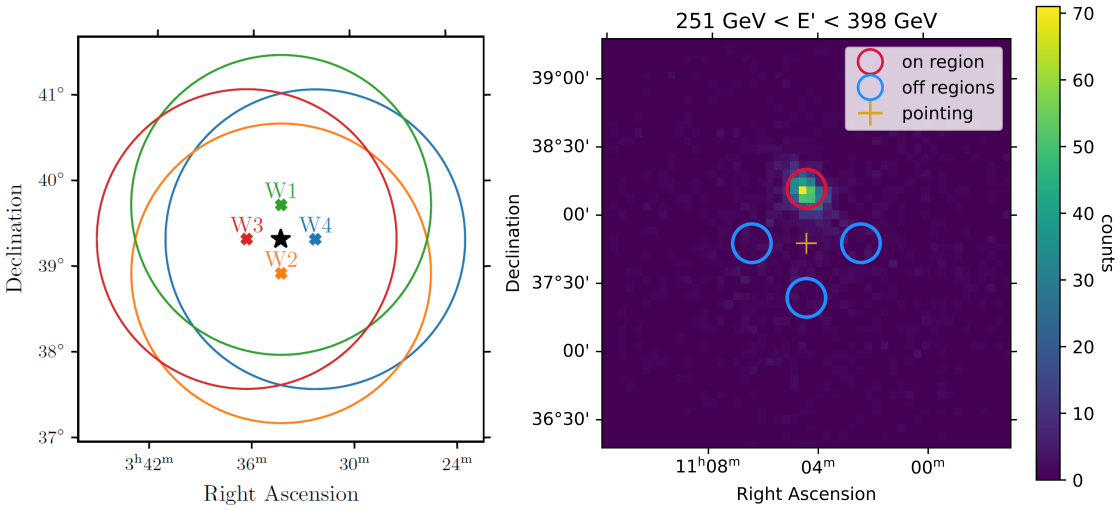

Figure 2.9: Visualizations of the strategy of wobble mode observations. Left: The source sits at the position of the black star inside the coordinate field. Four symmetric wobble positions around it are marked with green (W1), yellow (W2), red (W3) and blue (W4) crosses along with the correspondingly colored FoVs of MAGIC. From [78]. Right: Sky map with a single run of observations of the blazar Mkr421 in an energy range from 251 GeV to 398 GeV. The yellow cross indicates the pointing position in wobble mode for that run. The respective ON (red) and OFF (blue) regions are superposed with circles at a certain offset from the pointing. Credit: C. Nigro.

cated with blue circles, while the ON region, containing the source counts from a single wobble run, is shown in red. The wobble mode ensures that the background is estimated from observations taken under the same atmospheric and instrumental conditions. In the right panel of Fig. 2.9, the position of the source and therefore the ON and OFF regions will rotate around the pointing position (yellow cross). This way the background is sampled from all sections of the camera and systematic effects due to inhomogeneities in the camera are smeared out.

Chapter 3

The Boomerang Supernova Remnant G106.3+2.7

The Boomerang SNR G106.3+2.7 is the residue of a Galactic supernova explosion, located in the constellation of Cepheus in the northern sky. It covers around $60' \times 24'$ with a complex comet-shaped structure featuring two distinct regions, today commonly called the Head and Tail region. A composite image of the source is displayed in Fig. 3.1. It shows a 1420 MHz radio temperature brightness map as presented in [89], extracted from the observations of the Canadian Galactic Plane Survey (CGPS) [99] made available at the Canadian Astronomy Data Centre[1]. The Head and Tail regions, enclosed by green dashed lines and labeled, are distinguishable by high and low surface brightness in the 1420 MHz radio continuum. The remnant is associated with the pulsar PSR J2229+6114 and its PWN, the Boomerang PWN G106.6+2.9, which are both located at the far north-eastern edge of the complex and marked with a green cross and a green dashed circle in Fig. 3.1, respectively. In addition, emission centroids of the HE and VHE emission measured by the *Fermi*-LAT [107], HAWC [10] and LHAASO [29] as well as the extended emission region observed by VERITAS [5] are superimposed and labeled accordingly.

The first ever mention of G106.3+2.7 can be found in an article of 1990 by Joncas and Higgs [66]. They described the source in the following way:

> **G106.30+2.76:** This object seems to consist of two "lobes" of irregular outline and was initially thought to be a normal HII region. The discovery that it had no associated infrared emission prompted an analysis of the survey data of Kallas and Reich (1980) in order to determine the flux density at 1420 MHz. The value found, 4.69 ± 0.014 Jy, indicates a spectral index of

[1] https://www.cadc-ccda.hia-iha.nrc-cnrc.gc.ca/en/

> 0.45 ± 0.05. Again, this object appears to be a supernova remnant that has previously been undetected. It is of large angular size and high-resolution observations would be very worthwhile.

The short record names several of the characterizing properties of this source for the first time, e. g., the double-component structure, the large angular extension and its probable nature as a SNR without a counterpart in the Infrared (IR). The discovery was made as part of a survey of the northern Galactic plane carried out at 408 MHz (74 cm) with the Canadian Dominion Radio Astronomical Observatory (DRAO). While this was the first time it was listed, it had actually been mapped by Kallas and Reich in the 1420 MHz (21 cm) radio continuum with the Effelsberg 100 m radio telescope ten years prior to its detection [67]. At that time the Boomerang SNR was not identified, because the publication focused on structures with an angular size smaller than $30'$, whereas G106.3+2.7 has a maximum extension of around 1° along its major axis. As stated in the quote, the 1420 MHz observations by the Effelsberg telescope have also

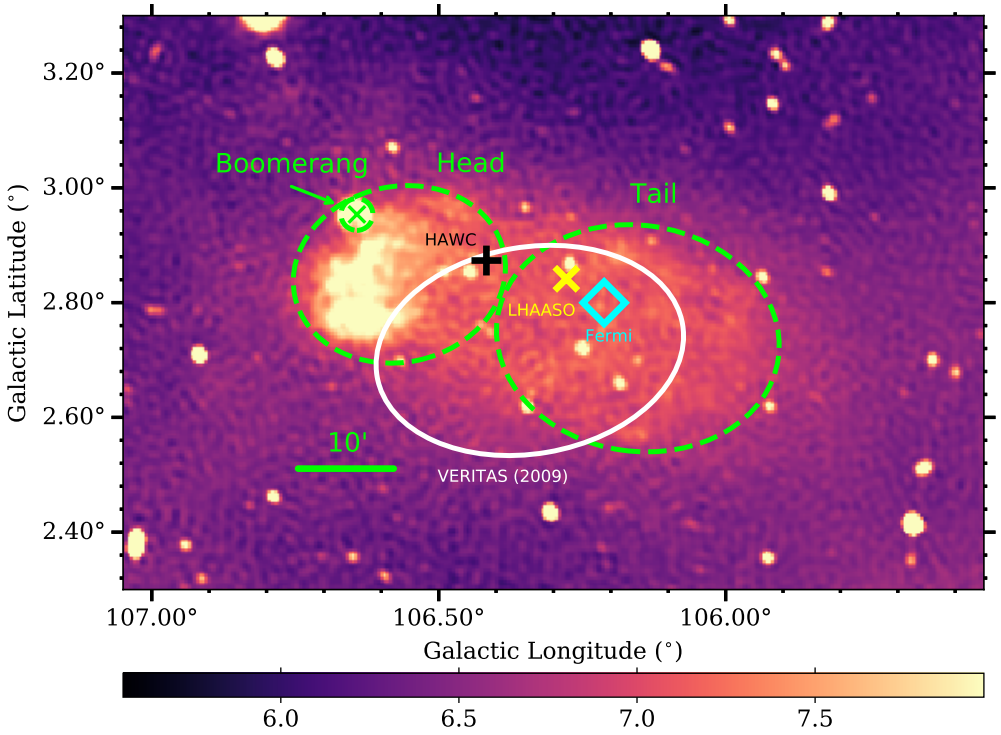

Figure 3.1: Multi-wavelength view of the of the Boomerang SNR G106.3+2.7. Colors indicate levels of the 1420 MHz radio temperature brightness [K] from archival CGPS data. Head and Tail region are marked with green dashed lines and labeled, as well as the Boomerang PWN at the north-eastern edge of the complex. The pulsar PSR J2229+6114 is located at the green cross. The map is superimposed with several emission centroids of γ-ray observations by HAWC, LHAASO, *Fermi*-LAT and VERITAS. From [89].

been used to complement the investigation presented in [66]. Fig. 3.2 shows the first depiction of the source from 1980 [67] (elongated structure in the top right corner of the field) and the map related to its detection from 1990 [66] (elongated structure located to the right of the center). Both images display the spatially elongated source shape with a rather modest angular resolution, compared to later measurements. The double-component nature in the radio regime, hypothesized by [66], was confirmed by another survey carried out with the Effelsberg telescope at 2695 MHz (11 cm) [49].

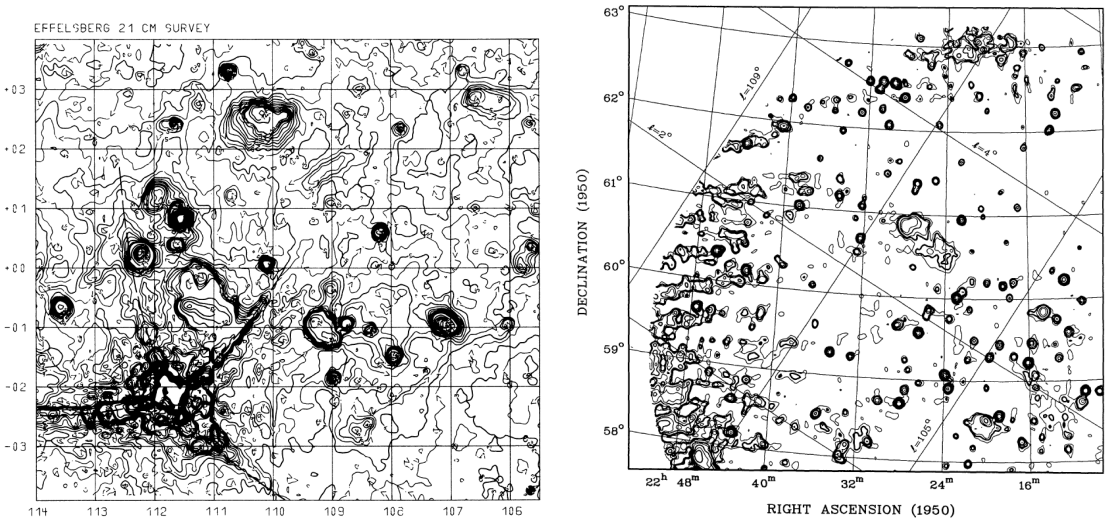

Figure 3.2: Earliest radio maps of the Boomerang SNR. Left: First image of the remnant from a 1980 survey at 1420 MHz carried out with the Effelsberg telescope. The elongated structure in the top right corner of the field was discarded due to a maximum extension selection criterion. From [67]. Right: Image of detection of the remnant from a 1990 survey at 408 MHz carried out with the DRAO. The elongated SNR is visible to the right of the field center, composed of two lobes. From [66].

The first dedicated study was done some years later by Pineault and Joncas [88], again using one of the radio telescopes of the DRAO, the Synthesis Telescope (ST). They observed the Boomerang SNR in the continuum both at 408 and 1420 MHz. Additionally, they carried out 21 cm line observations of neutral hydrogen (HI), thereby providing neutral hydrogen spectral information and HI channel maps. With their data, they were able to confirm the general morphology and spectral index of the object, supporting the theory that it is an SNR. Moreover the absence of significant IR emission related to the complex is affirmed. Pineault and Joncas derive a maximum kinematic distance of 12 kpc from the 408 MHz flux. According to them, the source is consistent with an shell-type SNR in the late phases of its isothermal evolution, considering the determined properties. The reader can consult [91, 18] for more details about the evolution of SNRs. The authors of [88] use the term "boomerang-like shape" to describe a compact feature

located at the north-eastern corner of the elongated radio emission region. They mention that it could be an extragalactic object of type radio galaxy, but note that the spectral index does not differ much from the rest of the SNR complex. At this point unknown, the feature was later associated to the PWN G106.6+2.9, dubbed Boomerang PWN due to its boomerang-like shape.

In 2001, Halpern et al. were the first to bring X-ray and γ-ray data into the picture of the Boomerang complex [57]. They explored the possibility of an association of the γ-ray source 3EG J2227+6122 from the third Energetic Gamma Ray Experiment Telescope (EGRET) catalog [59] with counterparts in the radio and X-ray regime. To this end, they took archival and dedicated radio, optical and X-ray data from several instruments and discussed possible associations and related implications for the nature of the source. Inside of the 95 % error circle of 3EG J2227+6122, the authors found the radio shell V2229.0+6114 and a point-like X-ray counterpart RX/AX J2229.0+6114 to be the only feasible counterparts. The possibility of the radio source being an HII region was found to be very unlikely, due to the high degree of linear polarization throughout the radio shell, the absence of Hα emission, and the absence of a star able to excite the ambient medium and provoke that emission. Due to the large X-ray measured column density of hydrogen, a distance of $\sim$ 3 kpc is estimated. A scenario in which RX/AX J2229.0+6114 is not related to the radio source and instead consistent with an extragalactic or distant Galactic object is not ruled out but disfavored, also because of a missing optical counterpart. On the whole, the paper concludes that an association of the three sources is more likely than unlikely, where RX/AX J2229.0+6114 would be an energetic X-ray pulsar counterpart of 3EG J2227+6122 and V2229.0+6114 a linked nebula powered by the pulsar. The possibility of a bow-shock nebula [26] compared to a nebula driven by the pulsar wind [87] is investigated but not conclusive.

While the search for an X-ray pulsation was without results in [57], the second paper by Halpern et al. was already in preparation and shortly after reported the detection of pulsed emission in the radio and X-ray range [58]. The study established the EGRET source to likely be a pulsar and the surrounding radio and X-ray emission as originating from a PWN, assigning the catalog name G106.6+2.9 to it. The measured pulsation period of 51.6 ms was discovered at 1412 MHz and subsequently found in archival X-ray data. A characteristic age of the pulsar of 10 kyr was derived.

In the same year, Kothes et al. were the first to do a combined review of the entire region containing the SNR, the pulsar and the related nebula [69]. They suggested that these elements are resulting from the same supernova explosion. The paper also provides the highest resolution radio maps of the Boomerang SNR and PWN so far. The authors present and discuss a scenario for the formation of the complex, supporting it with additional neutral hydrogen and carbon monoxide (^{12}CO) observations around the region. In the obtained maps (combined in Fig. 3.3), it is visible that the Head region seems to be wrapped in dense HI material to the east and could be created by the interaction of the shock wave of the explosion with this dense gas. The expansion

of the Tail region into the western direction can be explained with an outbreak of the expanding shock wave into a large HI bubble, visible in Fig. 3.3 as a circular region of low density open towards the south. Cold molecular material (^{12}CO) is detected to the northern and eastern edge of the HI bubble, as well as coinciding with the Tail region for radial velocities $> -6\,\mathrm{km\,s^{-1}}$ in Fig. 4 of [69]. The latter opens up scenarios for hadronic γ-ray production in the Tail region, since the molecular ^{12}CO poses a target material for *pp* interactions driven by accelerated protons from a shock wave hitting the cold cloud. From the radial velocities of the atomic hydrogen and the molecules a distance of 800 pc is derived, in conflict with previous measurements of several kpc. Again, a bow-shock nebula scenario is investigated, however confirming previous indications that the scenario is less probable than a PWN. A deeper study of the Boomerang PWN's polarization properties and magnetic field structure is presented in [68].

The era of ground-based γ-ray experiments started in the first years of the 21st century. The Milagro γ-ray observatory was the first to measure a hint of multi-TeV emission at 20 TeV from a candidate region thereupon named MGRO C4, coincident with the Boomerang complex [2]. This was confirmed with an 8-year dataset of the same experiment [4], focusing on the search for counterparts to Galactic entries of the Fermi Bright Source List. It lead to a significant detection of emission around 35 TeV at the level of $6.8\,\sigma$. The related *Fermi* source is 0FGL J2229.0+6114. The position error ($\sim 0.36_{\mathrm{stat}}\,^\circ$) of the maximum excess and angular resolution ($\sim 1\,^\circ$) of Milagro do not allow tracing back the TeV emission to a certain part of the Boomerang SNR, although the publication states that the emission centroid is close to PSR J2229+6114 with a signal of $6.6\,\sigma$ at the pulsar position.

In 2009, the detection of extended VHE γ-ray emission from G106.3+2.7 in the energy range from 900 GeV to 16 TeV was reported by VERITAS [5]. VERITAS was able to measure a source (VER J2227+608) with an extension of around $0.6\,^\circ \times 0.4\,^\circ$ and found that the peak VHE emission is well compatible with the cold molecular cloud situated in the Tail region. A powerlaw spectrum with a spectral index of $\Gamma = 2.29$ and a flux of $\mathrm{N_0} = 1.15 \times 10^{-13}\,\mathrm{cm^{-2}\,s^{-1}\,TeV^{-1}}$ is found to be in agreement with the flux at 35 TeV, reported by Milagro [4]. The latter suggests that the emission from MGRO C4 and VER J2227+608 are in fact resulting from a single mechanism. The coincidence of the VHE emission with the location of a molecular cloud, as well as the fact that the combined spectrum does not show a curvature at the highest energies, favors partly hadronic instead of purely leptonic models for γ-ray production [5]. This is one of the first hints at the Boomerang SNR being a PeVatron candidate for CR acceleration. In the same year, *Fermi*-LAT reported the first measurement of pulsed γ-ray emission from the pulsar PSR J2229+6114 [3], complementing the earlier detection of pulsations in radio and X-ray.

From 2019 to date, several more γ-ray experiments studied the Boomerang SNR complex, such as *Fermi*-LAT [107] (3 GeV to 500 GeV), HAWC [10] (40 TeV to 110 TeV), LHAASO [29] (up to 500 TeV) and Tibet ASγ [100] (above 10 TeV). All of them con-

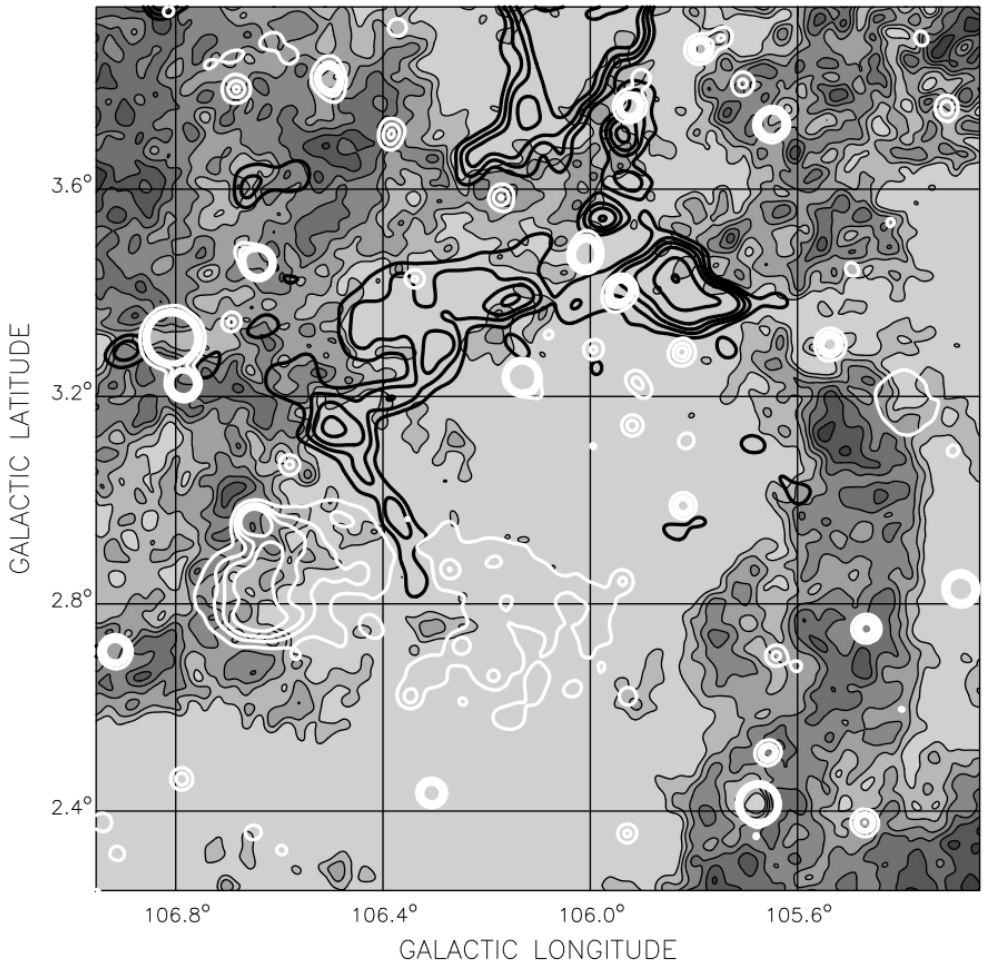

Figure 3.3: Gray-scale plot of neutral hydrogen distribution in the vicinity of G106.3+2.7. Overlaid black contours indicate the presence of molecular ^{12}CO and white contours the radio continuum contours at 1420 MHz. For the plot, neutral hydrogen and molecular carbon monoxide have been averaged over three channels at -5.6, -6.4, and $-7.2\,\mathrm{km\,s^{-1}}$. From [69].

firmed HE/VHE/UHE emission from the position of G106.3+2.7. Xin et al. [107] found evidence for GeV γ-ray emission, again coinciding with the molecular cloud complex in the Tail region. A lepto-hadronic model was preferred over the purely leptonic case. HAWC confirmed the spectrum and position of VHE emission described by VERITAS [5]. They also raise an unsolved question, that could contradict the PeVatron nature of the Boomerang complex: While the characteristic age of the pulsar and possibly the whole system is around 10 kyr, a SNR is expected to act as a PeVatron only in the first few hundred years after its explosion, which makes it difficult to explain the observed emission. They offer two explanations to resolve this discrepancy. If the SNR is actually

as old as the pulsar, particles able to emit VHE photons could have been accelerated in the young SNR, while they are now diffusing out and interacting, e. g., with a molecular cloud. If the SNR is younger and able to currently accelerate particles, the derived characteristic age approximation for the real age of the pulsar could be invalid for this system. They also mention the unlikely but still not ruled out possibility that the SNR and the pulsar/PWN system are after all not connected. With LHAASO's detection of UHE photons from 12 Galactic γ-ray sources [29], among which LHAASO J2226+6057 coinciding with the Boomerang SNR, the source became an even more promising PeVatron candidate. LHAASO J2226+6057 was claimed to emit photons as energetic as 500 TeV and have a flux comparable to the Crab Nebula flux at 100 TeV. While a measurement of emission at hundreds of TeV has been unprecedented and so far not been reproduced by any other experiment, the spectrum found by LHAASO connects well with other measurements. Another two publications strengthening the picture as a PeVatron candidate came with [100] by the Tibet ASγ detector and with an X-ray search [55]. In the former, the authors report an additional measurement of VHE emission from a region spatially corresponding to the molecular ^{12}CO material, favoring the hadronic model, but also raising the issue about the age of the SNR. In the latter, with an extensive X-ray study using a large dataset composed of data from the experiments Suzaku, *Chandra* and XMM-Newton, it was the first time that diffuse non-thermal X-ray emission from an SNR was detected [55]. The article states that the hard spectrum and spatially constant flux they obtain for the tail region is yet another indication for a PeVatron source, invoking the following argument: Their overall X-ray surface brightness profile for the SNR shows a multiple-component broken power law shape, with a transition to constant intensity moving from the Head to the Tail region. It suggests two different radiation processes for the parent electron populations of the synchrotron radiation. The SNR shock is the most probable accelerator in the Tail region to transfer energy to electrons in situ. They have to be accelerated locally since electrons cool efficiently and would not reach another region before radiating too much of their energy budget. If this is the case, the shock should have a high speed. On the one hand, this challenges the picture of G106.3+2.7 as a middle-aged or even old SNR. On the other hand, assuming a fast shock entails the necessary conclusion that also hadronic particles are efficiently accelerated by the shock in the Tail region, and therefore favors hadronic emission mechanisms for the VHE emission.

Apart from the above mentioned, many more works have explored leptonic and hadronic production scenarios for the multi-wavelength emission observed by experiments operating along the whole electromagnetic spectrum. The radio and X-ray emission close to the PWN and in the Head region has been found to be compliant with a non-thermal electron population in several cases [48, 73, 55]. For the VHE signal, some early modeling results partly disfavor leptonic and favor hadronic models, although they are not conclusive about the nature of the emitting process in the Boomerang SNR region [107, 10, 73]. Successively taking into account more sensitive flux measurements covering a larger range of the energy scale and including results by LHAASO [29], modeling results

became more constraining. Several results are now clearly selecting the lepto-hadronic models as the more probable ones for the Tail region [55, 43, 76].

In [72] a recent dedicated study of the ^{12}CO emission around the region of the remnant with the IRAM[2] 30 m telescope is presented. The authors are aiming to investigate how solid the association to the ^{12}CO molecular cloud complex is. According to them an illumination of a cloud with energetic hadronic particles is uncertain, although they find some nearby clouds in the same velocity range as [69]. Due to the cool temperature and similarity of the molecular cloud to ordinary clouds in the ISM of the galaxy, they state that it is unclear whether the molecular cloud is really heated by the SNR shock.

The study done by MAGIC in [76] will serve as a frequent reference later on, since this work is based on the same dataset of observations. It was the first measurement revealing details in the energy-dependent morphology of the source at VHE (see Fig. 5.2 in chapter 5). In the Tail region, the MAGIC collaboration found a strong preference for hadronic emission models, again hinting at a PeVatron. Detected γ-ray emission from the Head region meanwhile can be explained both with leptonic and hadronic processes. The flux and significance of the excess measured with MAGIC is consistent with previous measurements, for instance VERITAS [5].

Recently several articles concentrated more on the PWN of the system to constrain the possibilities of VHE emission originating from the surroundings of the pulsar, instead of the Tail region [71, 39]. So far, the PWN as a PeVatron cannot be ruled out. Latest results on this also include a combined multi-wavelength study by VERITAS and *NuSTAR*[3] [89]. In addition to their data and HE data from *Fermi*-LAT, they also used archival radio and *Chandra* X-ray data to constrain the emission properties of the Boomerang PWN. Compared to [69], the analysis indicates a larger distance of ~ 8 kpc, supported by three independent arguments and two decades more of spectral data in various wavelengths. Lastly, an article concerned with the ISM density derivable from X-ray and γ-ray observations was made public [19]. The authors intended to further probe the hypothesis of γ-ray emission involving processes with gaseous material in that region. Their conclusions are neither strongly supporting nor rejecting theoretized hadronuclear interactions between CRs and the ISM, although they confirm the presence of a low-density cavity, into which the SNR seems to be expanding (as in [69]).

Summarizing, the Boomerang SNR G106.3+2.7 can be considered one of the established most promising PeVatron candidates. The exact spatial and phenomenological origin of the VHE γ-ray emission, however, is still strongly debated. As described, there are attempts to explain this emission with the Boomerang PWN or with the older hypothesis of the SNR as a PeVatron. So far, both theories are encountering inconsistencies with observational evidence or current theoretical models of emission. Thus, current spatial measurements between several GeV and tens of TeV seem to indicate the SNR rather

[2] https://iram-institute.org/observatories/30-meter-telescope/
[3] https://www.nustar.caltech.edu/

than the PWN as a PeVatron. At the same time, it is not clear how an SNR of the estimated age of the Boomerang SNR can accelerate particles to such high energies. Ongoing and future investigations, e. g., with the MAGIC/LST-1 telescopes and with the upcoming CTAO, will help to reject or confirm these theories and simultaneously clarify if leptonic or hadronic production processes are the main reason for VHE emission from the Boomerang SNR complex.

Chapter 4

Data Analysis and Methodology for Extended Sources

The goal of this chapter is to familiarize the reader with concepts of the data analysis of IACT observations and methods implemented by the softwares adopted by the presented thesis, the MAGIC Analysis and Reconstruction Software (`MARS`) (see section 4.3.3) and `gammapy` (see section 4.3.2.6). I will explain all the necessary prerequisites for the subsequent presentation and discussion of my results in chapter 5, starting with a brief introduction of the main challenge faced in extended-source analyses (section 4.1). It will motivate the efforts invested in the following section, where I carefully explain the aforesaid key element, posing the challenge: the background (see section 4.2). Finally, I will discuss established tools and methods for the analysis of IACT data, as well as new software and methodologies that can contribute to solving the above challenge in IACT data analysis (section 4.3).

4.1 Introduction

Compared to the point-like nature of the majority of sources observed by the MAGIC telescopes, Galactic sources can be spatially extended. This is due to their proximity to the Earth inside the Galaxy. Even though MAGIC is located on the Northern hemisphere, observing mostly the Northern sky while the brightest part and the center of our Galaxy can be found in the Southern hemisphere, there are some extended sources visible from the observing site of the MAGIC telescopes in La Palma, Spain. Similar to any other telescope experiment, when pointing to a γ-ray source MAGIC does not only measure a source signal but also a background signal. Extended sources can cover larger areas on the sky and in the FoV of an IACT. Hence, in comparison to observations of point sources, observations of extended sources are more strongly affected by the background because they include more background signal inside the relevant analysis region.

Due to the complex nature of processes happening in the atmosphere, in and around the detector, this background is a priori unknown and depending on many factors. The non-trivial task posed for the analysis of extended sources is to correctly estimate the background, taking into account as many factors as possible. In order to understand the challenge in more detail we move to the second section, dedicated to the background.

4.2 Theory of the Background

Observations with IACTs are subject to different sources of noise. In the case of γ-ray observations, the background signal of various types is by far the most influential disturbance and needs to be estimated to extract the source signal. In what follows, we will dedicate some thought to the nature and impact of the background signal on the analyzed data. It is useful to distinguish between two important terms before starting:

- The *camera acceptance* of an IACT system is defined as the systemic response for the detection of Cherenkov events [46] in the camera FoV. It is different for γ-ray and hadronic events and depends on numerous parameters, among which the energy and the zenith angle [21]. As explained in [90], the acceptance for a single IACT is expected to be radially symmetric in the first approximation. The maximum detection efficiency for light lies in the center of the camera and gradually decreases towards the outer edge. With more than one instrument, the dependency of the *camera acceptance* will be dominated by the intersection of the trigger telescope FoVs. This will become more clear in section 4.2.2.1.

- The *background* is any measured signal adding up to the source signal and therefore considered a nuisance effect that has to be taken into account (rejected in real time, removed during low-level analysis or modeled during high-level analysis if still influential). The *background* inherits all the dependencies of the *camera acceptance*, as the response of the given system governs how many γ-ray and hadronic events are measured from which part of the camera and therefore determines the measured background signal.

4.2.1 Types of Backgrounds

For IACTs there is a conceptual difference between several kinds of backgrounds, of which the three most important ones will be mentioned here: the NSB (section 4.2.1.1), the diffuse γ-ray background (section 4.2.1.2) and the event-like hadronic background (section 4.2.1.3). Note that these types of backgrounds act differently on the measured signal and do not all have the same relevance, as explained below.

4.2.1.1 The Night Sky Background

The NSB is present in every recorded event and takes the form of an underlying base level of signal in every PMT of the camera, depending on the sky brightness. The

strongest influence on the NSB is determined by the intensity of the moon light. Also bright stars within the FoV of observations can have a strong effect on the NSB. Then, there is a contribution by artificial light sources, e g. from cities. Observations close to or in the Galactic plane are also affected by the stellar optical emission of a denser stellar background. All three contributions of the NSB are an additional source of noise in γ-ray data and influence the measured background [21].

4.2.1.2 The Diffuse γ-Ray Background

The diffuse γ-ray background refers to a background originating from additional triggered γ-ray events, that are not coming from the observed source. These showers stem from VHE γ-rays that are emitted by CRs propagating inside our Galaxy or by unresolved astrophysical sources in the FoV. The diffuse γ-ray background between 0.5 TeV and 2 TeV was studied with *Fermi*-LAT in [83], in which it was found that the majority of the diffuse flux lies in or close to the Galactic plane. Additionally, LHAASO has detected diffuse emission in the VHE to UHE regime, between 10 TeV and 1 PeV [31], confirming the measurement by Tibet ASγ in a similar energy range [16].

4.2.1.3 The Hadronic Background

The hadronic background, similarly to the diffuse γ-ray background, is constituted by additional triggered events from a background process. In this case, the showers are not induced by γ-rays but by all kinds of CR particles, leading to hadronic air showers. However, there is no influence on other recorded γ-ray events. On average, IACTs record one γ-ray event in a thousand hadronic events (mostly protons) for bright sources like the Crab Nebula [12], whereas the domination of hadronic showers can be even stronger for other sources. For that reason, analysis pipelines have to include powerful γ/hadron separation algorithms to reject this background.

In MAGIC, the γ/hadron separation is typically done estimating a parameter called hadronness and then introducing a cut in the events based on that parameter. The hadronness gives the probability for a shower to be induced by a hadronic particle instead of a γ-ray photon. Consequently, it should be close to 0 for a γ-ray shower and close to 1 for a hadronic shower. For the classification, a Random Forest (RF) is trained on the reconstructed image parameters (Hillas parameters explained in section 2.2.3.4) of simulated γ-ray events and hadronic events from OFF observations. It is then tested on a different dataset of simulated γ-ray events. Fig. 4.1 shows the final product of such a classification; the hadronness distributions for simulated γ-ray and real hadronic events in four different energy bins. Note, that the distributions have their expected peaks around hadronness values of 0 and 1 for γ-ray and hadronic showers, respectively. Depending on the energy, they show a more or less pronounced tail towards larger and smaller hadronness values. This implicates that a fraction of both γ-rays and CRs was misclassified in terms of the hadronness estimate. The effect is stronger at lower energies, where it is more difficult to distinguish between the two types of showers. It also means

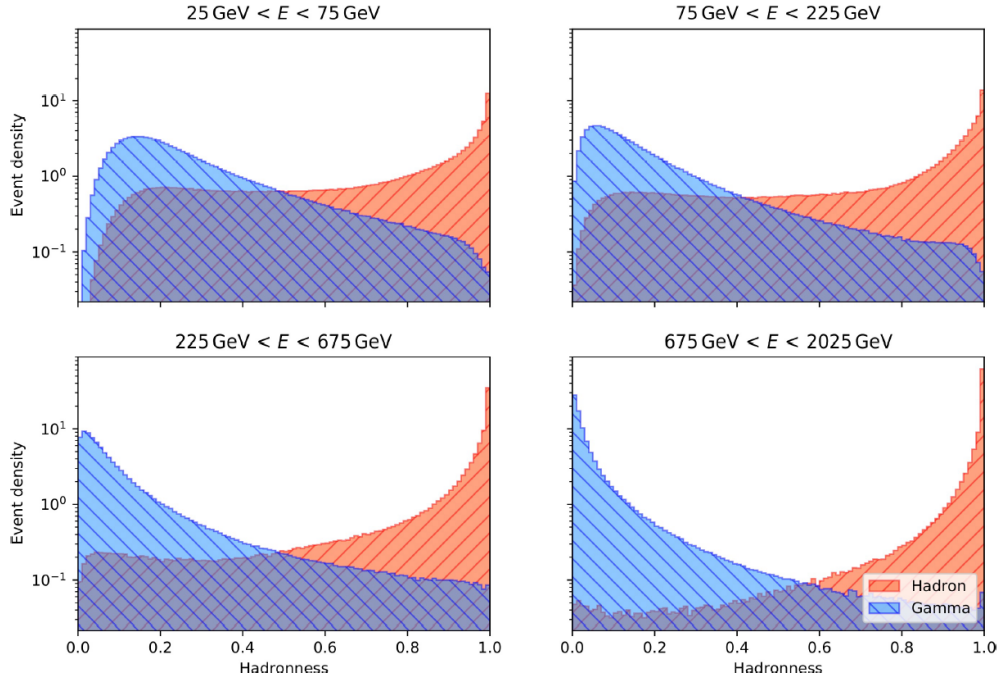

Figure 4.1: Hadronness distributions of simulated γ-ray data (in blue) and real CR data (in red) from Off observations for four energy bins between 25 GeV and 2025 GeV. From [33].

that a cut in hadronness, however strict, will never remove all hadronic events. To ensure a correct measurement of the flux of a source the remaining flux of background events has to be modeled.

4.2.2 Systematic effects on the Background Shape and Rate

The shape and rate of the background depend on numerous different parameters, e. g., the energy, the zenith and azimuth angle, the observational conditions and the instrumental performance. However, these can be traced back to four main elements at the origin of the dependencies: The MAGIC telescope system, the atmosphere, variations in the NSB and the geomagnetic field.

4.2.2.1 The MAGIC Telescope System

The MAGIC telescopes are subject to variable conditions, affecting the hardware or software and causing changes in efficiency during the data taking process. They are exposed to all weather conditions, causing a degradation of the mirror reflectivity and a non-constant Point Spread Function (PSF) of the system. The PSF is defined in section 4.3.2.4. The telescopes also undergo hardware interventions that result in changing performance. In order to take into account different periods of instrumental perfor-

mance, several steps in the data analysis are relying on dedicated MC simulations (see section 4.3.1), produced to suit the instrumental conditions of each period. For the same reason, the measured background of CRs can be different for different analysis periods [21].

Another effect stemming from the camera design of the telescopes is the geometry of macro cells that define the trigger region in the camera. As can be seen farther down in Fig. 4.5, the hexagonal trigger region (compare Fig. 2.8) shows up in the shape of the background in the two lower energy bins.

The geometry of the MAGIC telescope system during operations determines the dependence of the background on three different parameters: zenith angle, azimuth angle and event energy [21, 46]. The former two determine the shape and size of the overlapping region of the MAGIC view cones depicted in Fig. 4.2. In general the overlapping region has an eye-shaped form and events have to lie inside it to be triggered and recorded. As a consequence, the shape of the background is not expected to be radially symmetric, as would be the case for single telescopes or a symmetric 4-telescope system, but rather elliptical [78]. Looking at Fig. 4.3, note that the principal axis of the background is expected to be rotated around a rotation angle γ with respect to the horizontal, depending on the azimuth pointing. The amount of rotation is connected to the projected inter-telescope distance $d_{\text{projected}}$, which is the MAGIC 1 - MAGIC 2 inter-telescope distance of 83 m projected to the sky. It can be written as

$$d_{\text{projected}} = \frac{|(\boldsymbol{M}_1 - \boldsymbol{M}_2) \times \boldsymbol{n}|}{|\boldsymbol{n}|} \tag{4.1}$$

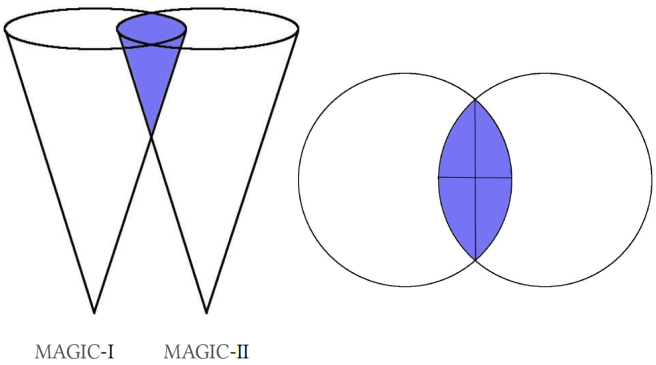

Figure 4.2: Schematic representation of the view cones of the MAGIC telescopes and their eye-shaped overlap region (marked in blue), seen from the side (left) and from above (right). From [78].

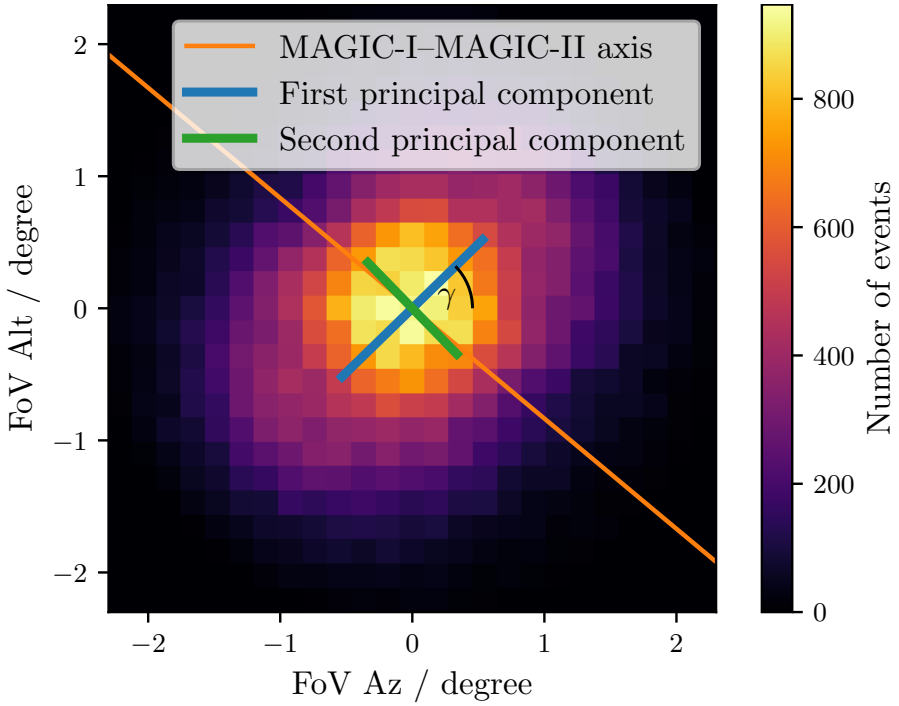

Figure 4.3: 2D histogram of γ-ray-like events from MAGIC OFF data, binned in FoV altitude and azimuth, in the azimuth range from 69 ° to 99 ° and the energy range from 0.05 TeV to 10 TeV. Indicated are the MAGIC 1 - MAGIC 2 telescope axis projected to the sky (orange), the first principal component (blue) and the second principal component (green) of the elliptically-shaped background, as well as the rotation angle γ, defined as the angle between the first principal component and the horizontal. From [79].

where $\boldsymbol{n}$ is the projection vector defined as

$$\boldsymbol{n} = \begin{pmatrix} \sin(Zd) \cdot \cos(-Az) \\ \sin(Zd) \cdot \sin(-Az) \\ \cos(Zd) \end{pmatrix} = \begin{pmatrix} -\sin(Zd) \cdot \cos(Az) \\ \sin(Zd) \cdot \sin(Az) \\ \cos(Zd) \end{pmatrix} \tag{4.2}$$

and $\boldsymbol{M}_1$ and $\boldsymbol{M}_2$ are the position vectors of MAGIC 1 and MAGIC 2 in an arbitrary coordinate system. Assuming we do a sweep of the whole azimuth range at a fixed zenith angle, looking at the top and bottom panel of Fig. 4.4, $d_{\text{projected}}$ and the rotation angle γ display a periodic change. The top panel of Fig. 4.4 demonstrates that the effect is negligible at small zenith distances but becomes increasingly dominating at larger zenith distances. Along with $d_{\text{projected}}$ the orientation γ of the elliptically-shaped background is expected to change, which was studied in [90] and confirmed in [79, 78] for the MAGIC telescopes and is visualized in the bottom panel of Fig. 4.4.

The dependence on energy can be explained considering that the size and therefore the elliptical image of the showers increases with energy. At energies above several TeV,

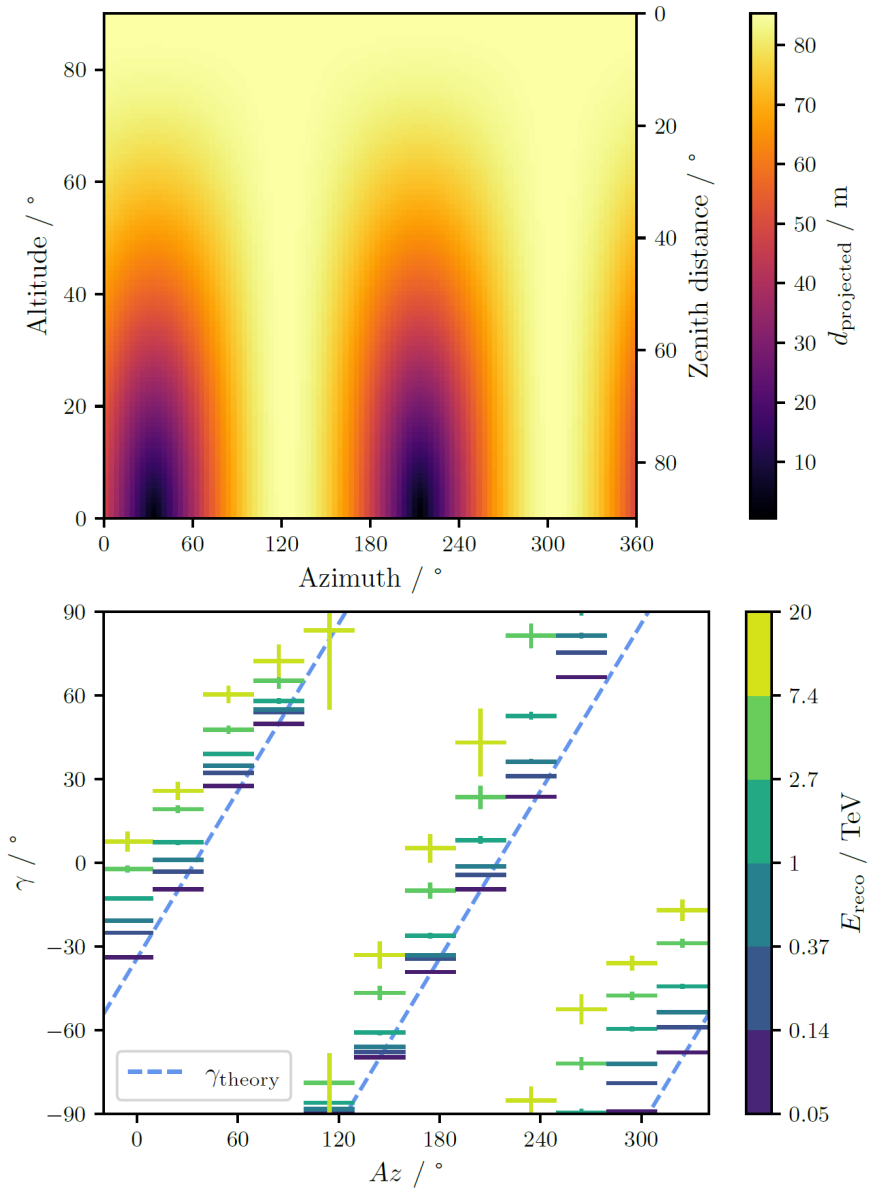

Figure 4.4: Graphs visualizing the influence of the pointing coordinates on the background. Both graphs are from [78]. Top panel: Dependency of the projected inter-telescope distance $d_{\text{projected}}$ on altitude/zenith and azimuth angle. It is visible that the amplitude of the change of $d_{\text{projected}}$ along the azimuth axis is larger for lower altitudes/larger zenith angles. Bottom panel: Measurements of the rotation angle γ of the elliptical background plotted against the azimuth angle for six logarithmic bins of the reconstructed energy from 0.05 TeV to 20 TeV. The blue dashed line is the relation expected from theoretical calculations.

shower images originating from the center of the camera in most cases are not fully contained in the camera any more, because the development of the shower happens towards the border of the camera. However, showers from the edge of the camera that develop into the direction of the camera center, even if large, can be contained entirely which makes the reconstruction of the event possible. For the highest energies the result is therefore a ring-shaped background for combined data from all azimuth angles and a dipole-shaped background for data covering only a certain azimuth range (considering a superposition with the elliptical shape of the background mentioned in the last paragraph). The first case is illustrated in the highest energy bins of Fig. 4.5 and the second case can be recognized in the background models, produced for this work. An example of these is shown farther down in Fig. 4.10 and the remaining background maps are attached in appendix A (Fig. A.1, A.2 and A.3 for the Crab Nebula and Fig. A.4, A.5, A.6 and A.7 for the Boomerang SNR). A similar ring-shaped background at high energies is also reported by other IACTs, such as the H.E.S.S. in [81]. However, in their case the background shape is circular even for data exclusively taken within a narrow azimuth bin. This can be explained by the multiple-telescope configuration, leading to multiple differently oriented baselines for all the possible combinations of two telescopes. Observing the sky at a fixed azimuth angle this results in several superimposing elliptical backgrounds with unequal rotation angle γ. The study by H.E.S.S. confirms that the depletion of the background rate in the camera center at high energies is an intrinsic feature originating from the imaging technique with more than one telescope. It is independent of the background estimation technique and the specific detecting array of IACTs.

4.2.2.2 The Atmosphere

The measured background flux also depends on the atmospheric conditions during an observation. It is expected to be higher for good observation conditions, including high transmission values of the atmosphere. Additionally, the airmass between the first point of interaction of the shower and the detector increases for large zenith distances. It follows that also absorption and effective area strongly increase, meaning that Cherenkov light from low-energy showers is progressively absorbed up to the point of total absorption for increasing zenith distance. Above $70\,^{\circ}$, this effect starts to become so strong that it varies within the FoV of MAGIC and can modify the shape of the background [78].

4.2.2.3 Variations of the Night Sky Background

The contributing factors to the NSB were listed in section 4.2.1.1. Depending on the pointing position of the telescopes and the absence or presence of the moon and other light sources, variations in the NSBthat affect the background measured by IACTs are introduced.

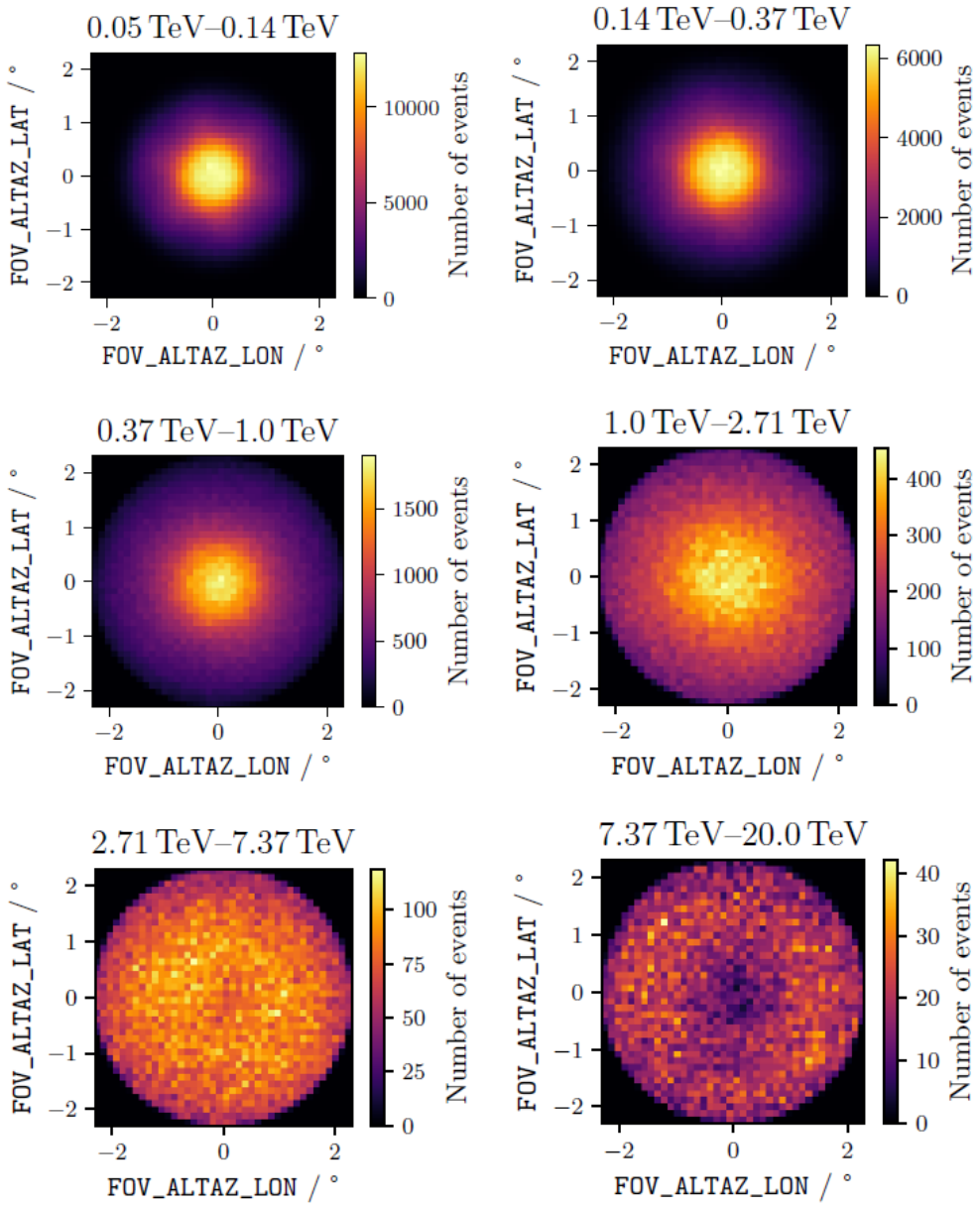

Figure 4.5: Background 2D histograms containing events from OFF data, showing the flux of CR showers inside the camera FoV of MAGIC, displayed in six logarithmic bins of the reconstructed energy from 0.05 TeV to 20 TeV. In the two lowest energy bins the hexagonal trigger region of the MAGIC telescopes is visible in the shape of the background, whereas at highest energies the camera acceptance becomes ring-shaped. This is due to an increasing number of showers originating from the center but exceeding the camera FoV and not being reconstructed. From [78].

4.2.2.4 The Geomagnetic Field

There are only a few studies of the influence that the geomagnetic field has on EAS. It is known that the geomagnetic field is not stable over time and it is deflecting charged particles by a non-neglectable amount in comparison to the dispersion of particles caused by Coulomb scattering [35, 46]. According to [78], the degradation of the event reconstruction due to the geomagnetic field might be an important effect. It should be lower for hadron-induced than for γ-ray-induced air showers.

4.2.3 Definition of the Background

Henceforth in this work, the term **γ-ray-like background** or **background** in general will be used according to the following definition. The background is composed of

- all the hadronic showers remaining in the final event selection after the low-level analysis because of misidentification as γ-ray showers,
- all the EM showers from the diffuse γ-ray background remaining in the final event selection because our methods do not allow to distinguish between these and γ-ray events from our source of interest.

4.3 IACT Data Analysis

This section explains the techniques for the analysis of IACT data, with a focus on methodology for extended-source analysis. It starts with a word on the importance and usage of Monte Carlo simulations (section 4.3.1) and concludes with a section about the systematic uncertainties of measurements with MAGIC (section 4.3.4). In between comes an introduction of the related software applied in a standardized and open framework, e. g., `gammapy` [41], the science tool of the future CTAO (section 4.3.2), or in a proprietary framework, e. g., the MAGIC Analysis and Reconstruction Software (`MARS`) [82, 108] of MAGIC (section 4.3.3). I will explain the standardized and open approach first since it is the main method applied in this master's thesis. In that case, the analysis is based on standardized data levels, from Data Level 0 (DL0) to Data Level 5 (DL5), denoting data in different stages of the analysis process [86]. A short description of the data levels will be given in section 4.3.2.1, on the example of the MAGIC analysis workflow. As we will see, the respective products of each analysis step in `MARS` do not always coincide with the standardized data levels. However, it will be shown that the analysis principles are shared between the proprietary and open workflows.

4.3.1 Monte Carlo Simulations

One essential task of IACT data analysis is to correctly identify γ-ray-induced air showers among the vast amount of background from hadron-induced air showers and to reconstruct their original energy and direction. To accomplish this, data, labeled as hadron- or γ-ray-like, is needed to train machine learning algorithms, in this case an RF. Real data

from IACTs can provide large hadronic data samples from regions without signal, but pure γ-ray data has to be simulated. Additionally, IACTs require simulations to compute IRFs to understand the response of the detector system (explained in section 4.3.2.4). Monte Carlo (MC) simulations solve this as they can imitate and be analyzed alongside real data. The general way to produce them is to simulate the development of showers in the atmosphere (for the MAGIC telescopes this is done with COsmic Ray SImulations for KAscade (`CORSIKA`) [60]), count the emitted Cherenkov photons, simulate the reflector response and finally simulate the camera response and the trigger and readout systems. The final output emulates real raw data and can be processed with the standard analysis software `MARS`.

The majority of required MC simulations in MAGIC are produced with a certain fixed offset from the camera center, related to the most common wobble offset employed for standard data taking (see section 2.3.2). However, this only makes sense for point sources, for which γ-rays are originating exclusively from positions with that offset in the camera. For extended sources or wobble observations at special offsets dedicated simulations have to be produced. In general, there exist two kinds of MCs:

- **Ringwobble MCs** contain simulated events from a single offset in the camera FoV. In MAGIC observations this offset typically is $0.4\,^\circ$.
- **Diffuse MCs** contain simulated events from multiple offsets up to a maximum offset in the camera FoV and are used for extended sources that cover a certain region in the camera. The maximum offset typically is at $1.5\,^\circ$ or $2.5\,^\circ$.

MCs are separately produced for multiple bins in zenith distance to account for a variable detector response at different zenith pointings. It has been mentioned before that the mirror reflectivity and PSF of the telescopes can degrade or change due to exposure to extreme weather conditions (see section 4.2.2.1). For this reason, different analysis periods are defined, in which the response of the system was constant, and MCs are produced for each period.

4.3.2 Standardized and Open Framework - Gammapy

The biggest part of this thesis work was done exploiting the standardized and open data formats and programs available to date. The following section is dedicated to the introduction of these standards and the software and routines applied in its framework.

4.3.2.1 Standardized Data Levels

Since the construction and commissioning of the first ground-based γ-ray telescopes, the γ-ray community has been applying proprietary data and software policies for the scientific exploitation of observational data. More recently, there are inter-collaborational efforts towards standardizing data formats and developing open-source software, to enable fully reproducible and multi-instrument analyses in the field. The first prototype

definition of standardized data formats is given in [36]. Further documentation of the effort is presented in [40] and the evolution of data formats and software in γ-ray astronomy has been reviewed and described more recently in [86]. The last article puts a special focus on the creation of the data formats for γ-ray astronomy, shortly referred to as the Gamma Astro Data Formats (GADF). The GADF [38, 37] sets standards for the name, content and metadata of high-level data files from γ-ray observations.

The most up-to-date standardized data levels used in `gammapy` and in this thesis are defined as follows: the raw output of a data acquisition software is called DL0; calibrated and cleaned data, containing the image parameters of the shower ellipses is called DL1; stereoscopic data containing the shower parameters of every event (reconstructed energy, direction and γ/hadron-separation information) corresponds to DL2; DL3 incorporates data in the form of event lists and the corresponding IRFs for each observation; DL4 represents data in the form of binned `Datasets` (as introduced in section 4.3.2.6); the final science products, like spectra or sky maps, belong to DL5. A schematic overview of these levels can be found in Fig. 4.6 for the low-level part of the analysis and in Fig. 4.11 for the high-level part.

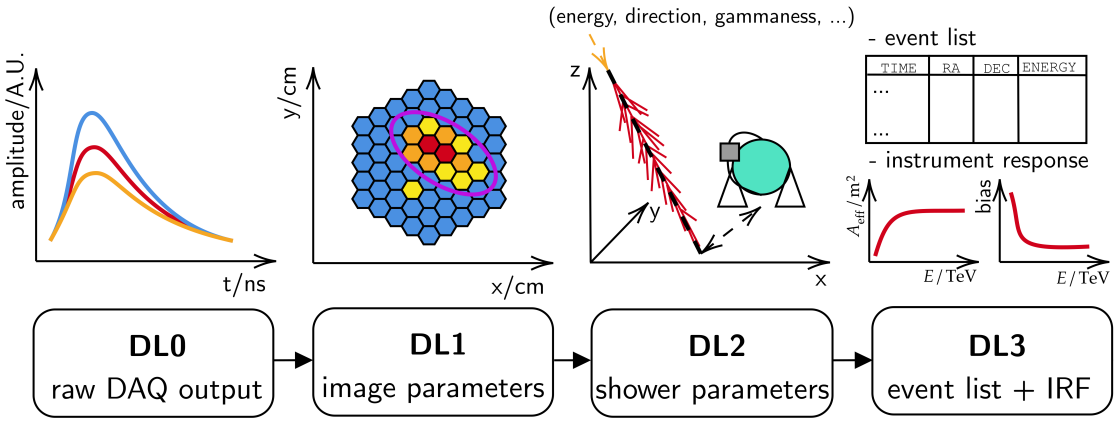

Figure 4.6: Schematic diagram of standardized data levels defining content and format of low-level products of IACT data analysis. Partly reprinted from [86].

Data Level 0 (DL0) is equivalent to the raw output of the data acquisition of the telescopes, amounting to 1 TB of binary files per telescope per night in the case of MAGIC. As shown in Fig. 4.6, it contains the sampled waveform of a pulse for each camera pixel of each L3 trigger, as well as each interleaved pedestal and calibration event. In the first step of the analysis these files are merged with the MAGIC subsystem reports and converted to `ROOT` files.

To produce data at Data Level 1 (DL1) it is necessary to compute the integrated charge in photoelectrons from the measured ADC counts and the arrival time of each event for both telescopes. This procedure is called calibration. Then, image cleaning is applied to remove all the pixels that do not contain any signal from the imaged shower, but only

background signal from the NSB. Finally, the Hillas parameters are derived for each event and stored in the data files, now at Data Level 1 (DL1). The information about single pixels is lost in this step.

In the following step Data Level 2 (DL2) is produced. It embodies data in the form of the reconstructed stereoscopic parameters, namely the energy, the direction and the hadronness parameters, which are estimated with RFs that have been produced using MC simulations (see Fig. 4.6). In MAGIC, this data level is produced by the program `melibea` (see section 4.3.3.2) and it is the direct starting point for any high-level analysis, that has science products as an outcome. This means that there is no intermediate step between DL2 and DL5 in `MARS`, but the programs which take `melibea` data as an input combine the computations described in the next three paragraphs.

After the transition to Data Level 3 (DL3), the data contains a list of γ-ray candidate events and their IRFs. The selection of events is done via a cut in the hadronness parameter (and depending on the projected type of analysis also a cut in the angular offset from the camera center θ) and the response of the system is computed using MC simulations, as explained in section 4.3.2.4.

Data reduction applies additional cuts in the data to be used for the final science products and imposes a geometry on the data, depending on the desired high-level product. The resulting DL4 files contain binned data products (see Fig. 4.11), ready for fitting and modeling procedures.

The final transition to Data Level 5 (DL5) makes different science products available, e. g., a Spectral Energy Distribution (SED), the significance of a signal, a light curve or a flux map, depending on the interest of the analyzer.

4.3.2.2 Spectral (1D) and Spectro-Morphological (3D) Analyses

There exist different types of high-level analyses, based on the corresponding objective and the desired high-level products, as well as the type of analyzed source. The most common cases are the 1-dimensional (1D) and 3-dimensional (3D) analyses, although the diagram in Fig. 4.7 also depicts the 2-dimensional (2D) analysis for completeness. The objectives and concepts of the 1D and 3D analysis will be exposed in the paragraphs below, while the actual methods for their realization will follow in section 4.3.2.3, 4.3.2.5 and 4.3.2.6.

1D Spectral Analysis: Estimating the flux of one or several γ-ray sources in a FoV is the common objective shared by all analyses of γ-ray observations. In the case of a 1D analysis, this is achieved by neglecting the extension of a source and applying a simple aperture photometry method [41]. Any spatial dependency of the flux is eliminated and the only remaining dimension of binning is the energy of the events (see first row in Fig. 4.7), hence the name 1-dimensional analysis. The flux is estimated inside a circular

aperture centered on the source called ON region, whereas the background rate is taken from one or multiple OFF regions inside the same FoV. They are typically positioned symmetrically to the ON region with respect to the pointing position, see Fig. 2.9, so that the following can be defined: Given a test region and a background control region, which contain a number of counts $N_{ON,i}$ and $N_{OFF,i}$, respectively, the number of γ-ray excess events inside the i-th energy bin E_i is

$$N_{excess,i} = N_{ON,i} - \alpha\,(E_i) \cdot N_{OFF,i}. \tag{4.3}$$

In this, the normalization factor α is in general a complex function taking into account differences between the test region and the background control region. These differences can originate from the size of the ON and OFF regions, the zenith angle and exposure time of the observation and the camera acceptance of CR events compared to γ-ray events. Applying a model to the data then means trying to reproduce the counts, taking into account all energy bins E_i.

3D Spectro-Morphological Analysis: Compared to the point-like appearance of single VHE γ-ray sources, Galactic sources are often extended and situated in FoVs with more than one γ-ray emitting object. The so-called 3-dimensional or spectro-morphological analysis [41] is the appropriate technique for extended-source analyses, more sophisticated and complex than the 1-dimensional analysis.

A 3D analysis analysis is able to account for the position and morphology of different (potentially overlapping) sources in the FoV. To this end, the data is binned in a data cube of three dimensions (see last row in Fig. 4.7), namely the two sky coordinates and the energy of the events, hence the name 3-dimensional analysis. It requires an estimate of the γ-ray background over the whole FoV because the emitting source is spread over a region in the camera with different offsets to the center and therefore different sensitivities. Re-interpreting Eq. 4.3 in the framework of a 3D analysis, the following changes have to be made: $N_{ON,i}$, binned in energy, becomes a set of quantities $N_{ON,i,j,k}$, binned in energy and two spatial coordinates, and analogous for the OFF counts. The normalization factor α is now also depending on two sky coordinates x_j and y_k, so that the three parameters fulfill

$$N_{excess,i,j,k} = N_{ON,i,j,k} - \alpha\,(E_i, x_j, y_k) \cdot N_{OFF,i,j,k}. \tag{4.4}$$

Equation 4.4 yields an excess value for each bin. The estimation of the background normalization function α is part of the main challenge mentioned in section 4.1 and very complex in the case of a 3D analysis due to the increased number of parameters. Additionally, knowledge of the PSF of the telescope is crucial to understand how a source "looks through the telescope" and to be able to distinguish the flux contributions from different sources overlapping at a certain sky location. Fitting a model to the data then implies reproducing the counts from the whole 3D data cube, which means simultaneously fitting spatial and spectral properties.

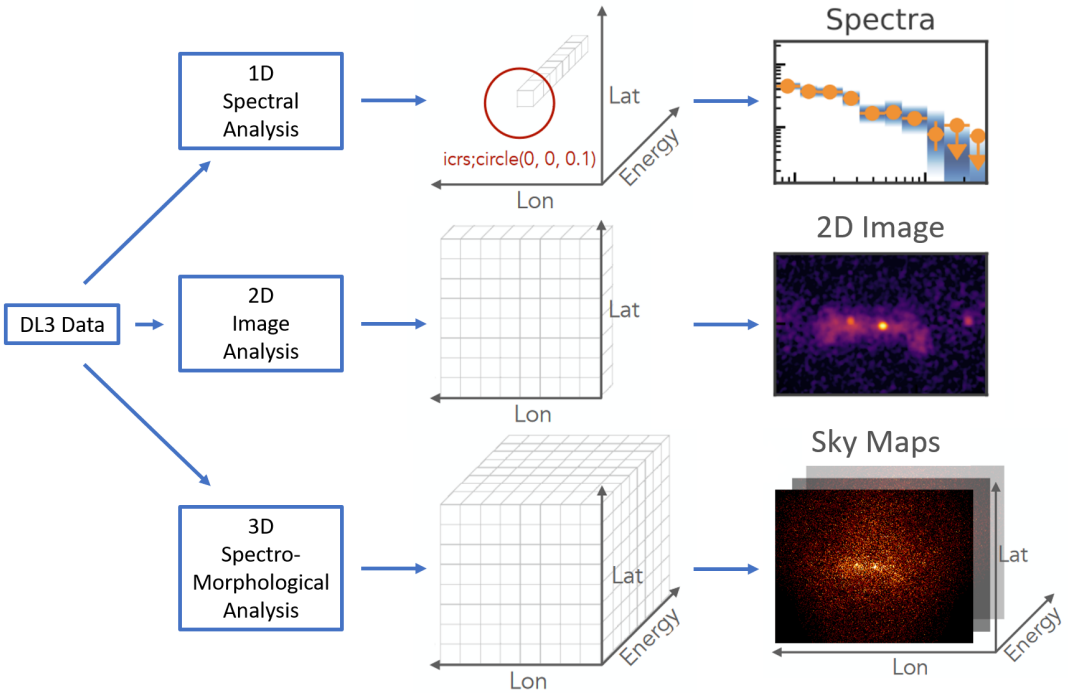

Figure 4.7: Scheme of different kinds of analyses in `gammapy`, based on the dimension of binning and the resulting data cube after reducing `Observations` to `Datasets`. The respective high-level products of a 1D, 2D and 3D analysis are spectra, 2D images, and energy-binned sky maps. Part of the elements is reprinted from [53].

The 3D analysis technique is a promising and potentially powerful tool to analyze extended sources observed by IACTs in the near future, but it is also a technique still in development. It has to be kept in mind that only a few 3D analyses have been realized in the field up to date [79, 81] and its characterization and validation is not concluded but rather an ongoing effort in the community of high-energy astrophysics.

4.3.2.3 Background Estimation Methods

Concerning the methods to estimate the background, Fig. 4.8 displays three ways to sample events from a dataset to construct a background model, using the source-free regions left free due to wobble mode strategy:

- for the **wobble map** (top panels in Fig. 4.8), individual camera exposures are separated in halves, in a way that the source will lie in the masked half. The underlying assumption is that the γ-ray emission connected to the source is confined to a maximum radius around the source position equal to the wobble offset angle and not leaking into the other half of the camera. Summing and normalizing the contributions of all source-free halves one can obtain a background model.

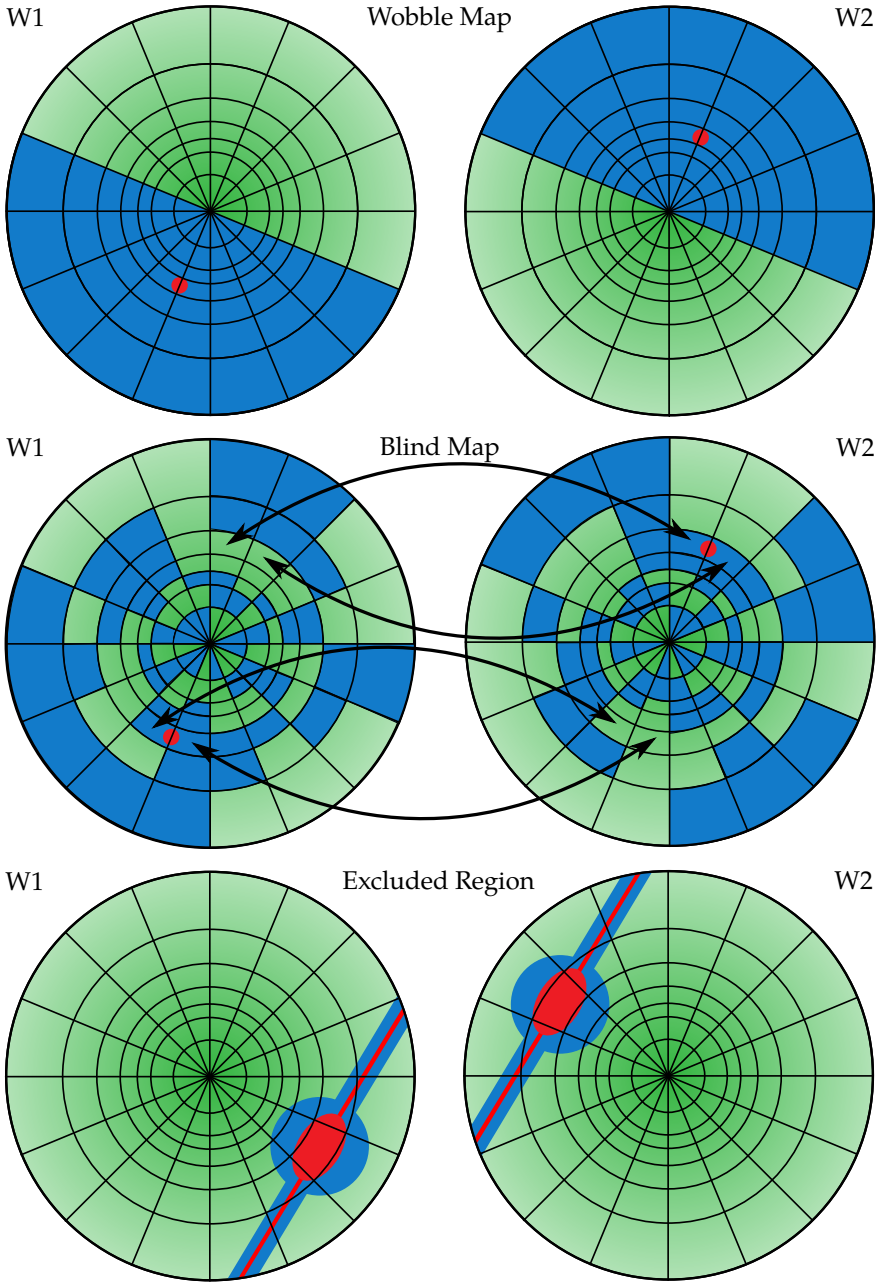

Figure 4.8: Visualization of wobble, blind and exclusion method to construct a background model using wobble observations, in this case for a wobble pair. Red and blue shaded areas indicate the source position/extension in the shape of a point, ellipse, or stripe and the wobble-wise bins excluded from the reconstruction of the background map. From [102].

- a **blind map** (center panels in Fig. 4.8) is created comparing the counts from wobble 1 (W1) and wobble 2 (W2) and taking the minimum values in each pixel. For more than two wobble positions the median value of each pixel is used, ruling out possibly high values due to a source. The method uses no information about the location of potential γ-ray emission (it works "blindly") and can be applied to sky fields in which the source position is not well-known. Inherent to the method, there is an effect of underestimation of the background in case of two wobbles, entailing a necessary modification by a correction factor to account for the introduced bias.

- the **exclusion method** (bottom panels in Fig. 4.8) relies on the knowledge of the source position in the camera and the definition of one or multiple exclusion regions (marked in blue in Fig. 4.8) by the analyzer. The diversity in shape of the available exclusion regions depends on the program, for instance `SkyPrism` (see below) can only handle circular or line-shaped regions, whereas `gammapy` provides several additional shapes, e. g., an ellipse and a rectangle. The background map is computed from the remaining free region in the camera.

4.3.2.4 DL3 Converter - Conversion to DL3 and Production of IRFs

The `DL3 Converter` is a program of MAGIC realizing the conversion of the MAGIC proprietary `ROOT` files, at an equivalent level of DL2, to standardized `FITS` files at DL3. Due to the proprietary software policy in MAGIC there is no public release but the reader can refer to [86] and [85] for more information. Apart from converting into another format, the main task of the `DL3 Converter` is the utilization of analysis cuts on the data, e. g., cuts in hadronness, and the generation of so-called Instrument Response Functions (IRFs) using MCs. They are instrument-specific functions mapping the estimated quantities of each photon to their true quantities. Hence, they need to be known to compute the physical values from the measured values and to fit physical source models to the observed data. Owing to the fact that for MC events the knowledge about true and estimated quantities is given at the same time, the IRFs can be constructed from simulations. There are three main elements:

- the **Energy dispersion**, which is the mathematical relation between true and estimated (E_t and E) energy $E_\mathrm{disp}\,(E|p_\mathrm{t}, E_\mathrm{t})$, represented by the Probability Distribution Function (PDF) of the estimated energy. It also depends on the true direction of the primary γ-ray p_t.

- the **PSF**, describing the spatial distribution function $PSF\,(p|p_\mathrm{t}, E_\mathrm{t})$ of the estimated event coordinates of photons from a point source, as seen through the telescope, where p is the reconstructed direction of the incoming γ-ray.

- the **Effective area**, embodied by the effective collection area of the telescopes $A_\mathrm{MC,total}$, corrected with an energy-dependent efficiency originating from energy-

dependent analysis cuts as

$$A_{\text{eff}}\left(p_{\text{t}}, E_{\text{t}}\right) = \frac{N_{\text{MC,final}}\left(p_{\text{t}}, E_{\text{t}}\right)}{N_{\text{MC,total}}\left(p_{\text{t}}, E_{\text{t}}\right)} \cdot A_{\text{MC,total}}, \tag{4.5}$$

where $N_{\text{MC,final}}\left(p_{\text{t}}, E_{\text{t}}\right)$ and $N_{\text{MC,total}}\left(p_{\text{t}}, E_{\text{t}}\right)$ are the numbers of events, which survived the analysis cuts and which were simulated in total, respectively.

With the above ingredients, the complete instrument response can be written as

$$R\left(p, E|p_{\text{t}}, E_{\text{t}}\right) = A_{\text{eff}}\left(p_{\text{t}}, E_{\text{t}}\right) \times PSF\left(p|p_{\text{t}}, E_{\text{t}}\right) \times E_{\text{disp}}\left(E|p_{\text{t}}, E_{\text{t}}\right), \tag{4.6}$$

and the predicted counts $N\left(p, E\right)$ in a spectral and spatial bin $\mathrm{d}p\mathrm{d}E$ can be calculated as

$$N\left(p, E\right)\mathrm{d}p\mathrm{d}E = t_{\text{obs}} \int_{E_{\text{t}}} \mathrm{d}E_{\text{t}} \int_{p_{\text{t}}} \mathrm{d}p_{\text{t}}\, R\left(p, E|p_{\text{t}}, E_{\text{t}}\right) \times \Phi\left(p_{\text{t}}, E_{\text{t}}\right) + b\left(p, E\right) \tag{4.7}$$

where $\Phi\left(p_{\text{t}}, E_{\text{t}}\right)$ is the source model, composed of spatial and spectral components, t_{obs} is the observation time and b are the background counts. N is mapped from the true model quantities with the IRFs. The `DL3 converter` computes the IRFs in terms of a single offset parameter, instead of two coordinates described by the direction p. The underlying assumption of radial symmetry of the system response is at the moment predetermined by the definition in the GADF, which does not allow asymmetric IRFs.

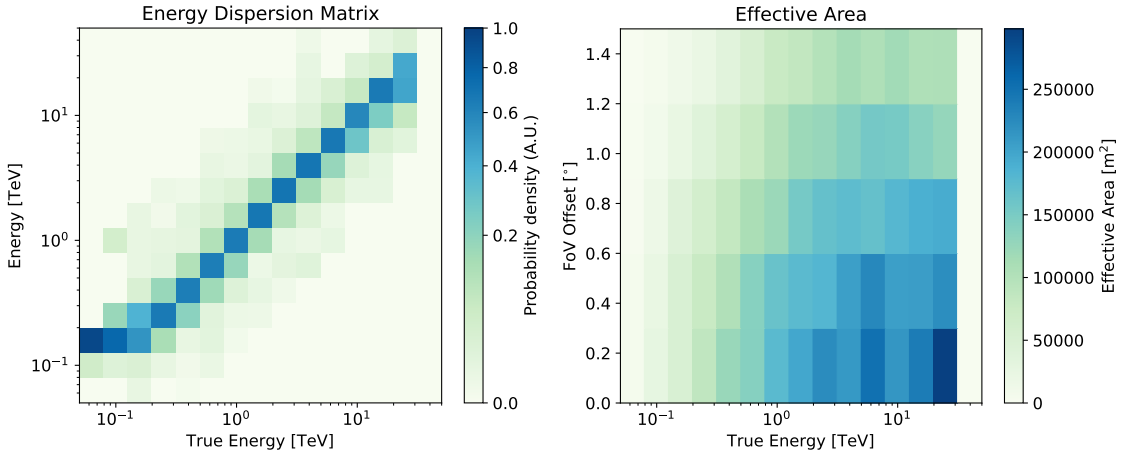

(a) (b)

Figure 4.9: Examples of two IRFs, computed from a single run of Boomerang SNR observations: energy dispersion (a) and effective area (b). In (a) the plotted quantities are the reconstructed energy E and the true energy E_{t} in a range from 50 GeV to 50 TeV. The events' energy is correctly reconstructed for $E = E_{\text{t}}$. In (b) the effective area is given in m^2, depending on the true energy E_{t} and the FoV offset from the camera center.

In Fig. 4.9 I show two example IRFs, the energy dispersion matrix and effective area, produced with a single run of Boomerang SNR observations. Fig. 4.9a plots the reconstructed energy E with respect to the true energy E_t of all events in an energy range of 50 GeV to 50 TeV. For correctly reconstructed events the relation $E = E_\mathrm{t}$ is expected to be fulfilled. As can be seen on Fig. 4.9a, this is the case for all events which lie in an energy range from $\sim$ 200 GeV to $\sim$ 30 TeV. From this fact, the need for a lower energy threshold in the analysis can be justified. Fig. 4.9b on the other hand, is a histogram of the effective area values given in units of m^2 and plotted in bins of the true energy E_t and the FoV offset from the camera center. The effective area decreases for increasing offset and decreasing energy.

4.3.2.5 Pybkgmodel - Production of Background Models

In the previous sections it became clear why a dedicated background model of the FoV is crucial for accurate extended-source analyses and necessary for a 3D analysis. One of the existing tools for that task is `pybkgmodel` [98], a python package designed for the CTAO, but usable in a slightly modified version also with MAGIC DL3 data. The program takes DL3 `FITS` files as an input and estimates the background from the data. Available methods for background estimation are the exclusion and wobble methods as introduced in section 4.3.2.3. Moreover, `pybkgmodel` can be run in two modes: stacking and run-wise mode. In the first, the output of the program is set to be a stacked background model, averaged over all input runs; in the second a separate background model for each run is computed, which is more accurate but can be problematic in terms of statistics. Apart from this, settings that have to be specified in the input card include the desired energy and spatial binning and in case the program is run with the exclusion method also an exclusion region in ds9 format[1].

The visualization of an example 3D background model, as obtained with `pybkgmodel` is shown in Fig. 4.10. It displays 2D histograms of the background rate in 12 logarithmic energy bins from 50 GeV to 50 TeV. The background rate is given in units of $\mathrm{MeV}^{-1}\,\mathrm{s}^{-1}\,\mathrm{sr}^{-1}$ and the camera plane is divided in spatial bins of FoV longitude and latitude. The program was run on Boomerang SNR observations from the MC period ST.03.11 for these plots. Apart from the limited statistics at high energies, two effects mentioned in section 4.2.2.1 can be verified in the histograms. The first is the asymmetry of the measured background due to the eye-shaped region in which events inside the MAGIC view cones are preferentially triggered. The second is the energy-related depletion of the background rate in the center of the camera, when moving to higher energies. It can also be seen that the available statistics in the highest energy bins is very low in general, although the final .

[1] https://ds9.si.edu/doc/ref/region.html

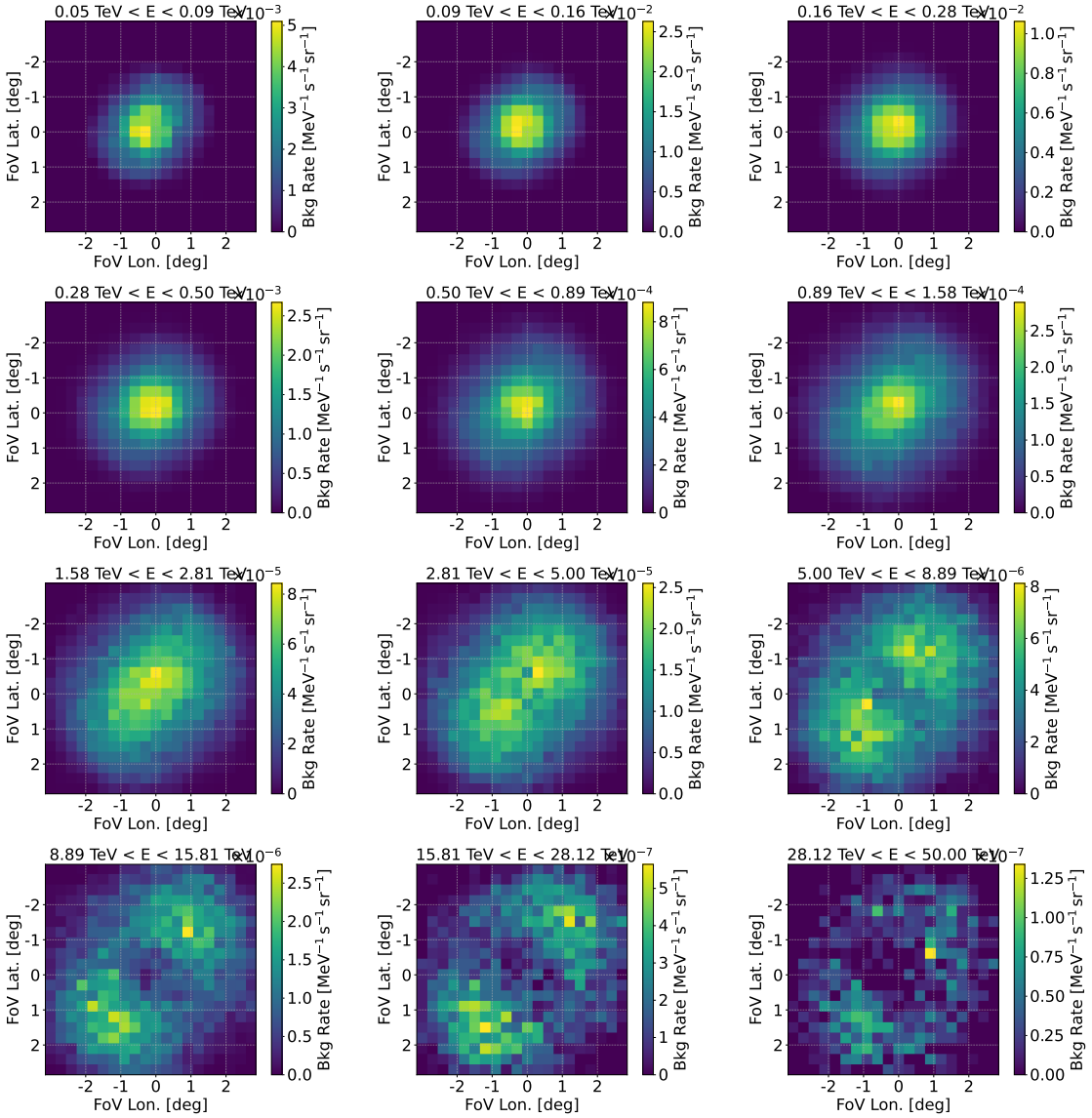

Figure 4.10: Example for a 3D background model from observations of the Boomerang SNR. It is a background model produced with `pybkgmodel` for the period ST.03.11. It contains 2D histograms of the background rate inside the camera FoV in 12 logarithmic energy bins between 50 GeV and 50 TeV. The background rate is given in units of $\mathrm{MeV}^{-1}\,\mathrm{s}^{-1}\,\mathrm{sr}^{-1}$ and the camera plane is plotted in degrees of the FoV longitude and latitude. Both the ellipticity of the background shape as well as the dipole-shaped feature in the highest energy bin have been explained in section 4.2.2.1.

4.3.2.6 Gammapy

`Gammapy` is an open-source software package written in `python`, designed for γ-ray astronomy [41] and adopting the standardized data level policy defined in the `GADF` [37].

Data Storage - `Observations` and `Datasets` The two main classes for data storage in `gammapy` are called `Observation` (DL3) and `Dataset` (DL4), both included in the scheme in Fig. 4.11. The first corresponds to a single observing run and stores the information about the energy, original direction, time of arrival and IRFs of all events. The second contains reduced data of a certain kind, depending on the desired high-level product. For instance, for a 1D analysis the `SpectrumDataset` and for a 3D analysis the `MapDataset` are required and have been used for the corresponding parts of this work.

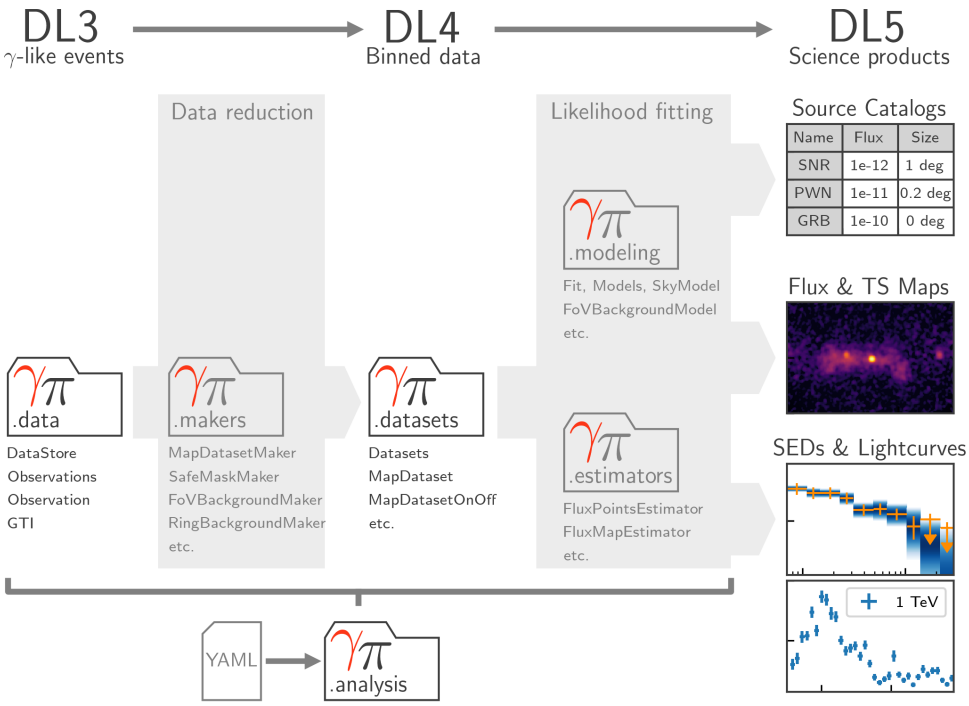

Figure 4.11: Scheme of the high-level data flow in `gammapy`, displaying the relevant classes for data storage (first column, DL3), data reduction (second column), binned data products (third column, DL4), modeling and fitting routines (fourth column) and science products (last column, DL5). From [54].

Data Reduction - `SpectrumDatasetMaker` and `MapDatasetMaker` Makers in `gammapy` are classes applied for the data reduction (see second column in Fig. 4.11), converting `Observations` to `Datasets`. Corresponding to the desired high-level product, the `SpectrumDatasetMaker` and the `MapDatasetMaker` are used to reduce `Observations`, such that the events are binned in energy (and in sky coordinates for the `MapDataset`)

and prepared for modeling and fitting. The makers also interpolate the exposure, background, PSF and energy dispersion on the chosen analysis geometry (for instance 1D or 3D) for each `Observation`. To make sure that only reliably reconstructed data is used, the `SafeMaskMaker` can introduce further cuts in the considered data cube, for instance based on the maximum offset to consider or the minimum desired effective area.

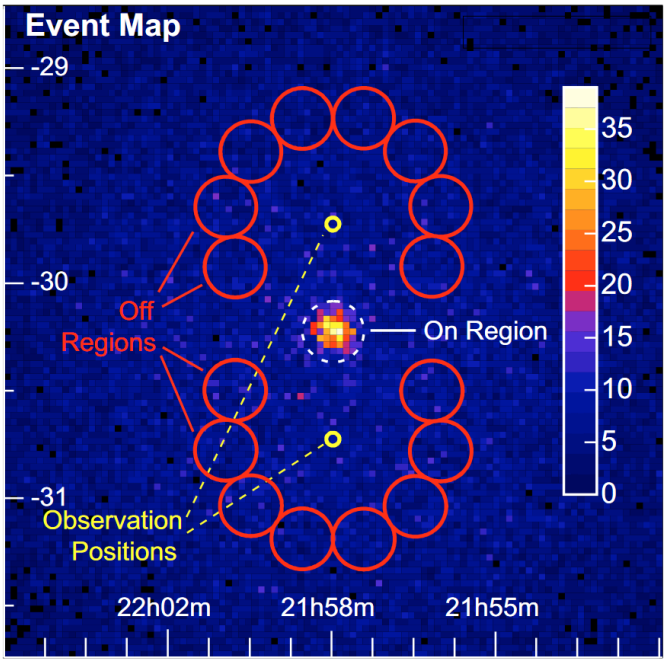

Figure 4.12: Illustration of the reflected regions background construction on an example source, centered in the FoV of the event map. The ON region is drawn with a dashed white circle, wobble positions are marked with two yellow circles and OFF regions, constructed by the `ReflectedRegionsFinder`, are overlayed as red circles. From [21].

Background - `ReflectedRegionsBackgroundMaker` and `FoVBackgroundMaker` The reflected regions background is a classical technique in γ-ray astronomy to estimate the background in a 1D spectral analysis (in `gammapy` it is applied with the `ReflectedRegionsBackgroundMaker`). As illustrated in Fig. 4.12, an ON region is defined around the source position and reflected on the two wobble positions with the `ReflectedRegionsFinder` to obtain the OFF regions from which the background counts are taken. It is important to create exclusion regions that cover the expected emission regions to avoid a γ-ray signal in the background falsifying the estimate. The underlying assumption of this method is the approximate radial symmetry of the background. For the case of a 3D analysis where the primary high-level products are sky maps instead, I applied the `FoVBackgroundMaker` to the template background models, previously produced with `pybkgmodel`. This step enables a re-normalization of the background cube to the data cube, and also an adaptation of the spectral distribution of the

`FoVBackgroundModel` that is a `PowerLawNormSpectralModel` by default (defined in the last paragraph of the section). Background estimation routines are applied in the form of their corresponding makers during data reduction in `gammapy` (see second column in Fig. 4.11).

Producing Spectra and Maps - `FluxPointsEstimator` and `ExcessMapEstimator` The `gammapy` estimator classes make use of algorithms for hypothesis testing (meaning that a reference model is evaluated against a null hypothesis) to realize flux and significance estimation on datasets. The step corresponds to the transition from DL4 to DL5 (see fourth column in Fig. 4.11). The presented analysis of this thesis contains flux points and flux maps in bins of the reconstructed energy that have been estimated with the `FluxPointsEstimator` and the `ExcessMapEstimator`, respectively. The `ExcessMapEstimator` thereby uses a `Tophat2DKernel` function to correlate the signal inside a certain radius and calculate a significance value for each point of the sky map.

Likelihood fitting routines - Spectral and Spatial Models The `gammapy` modeling and fitting routines (using the package `iminuit`) are based on a binned maximum likelihood approach, explained generally in [77]. During a fit, the quantity calculated in Eq. 4.7 is fitted to the data cube of a dataset binned in one or three dimensions (1D and 3D analysis), resulting in an optimization of the model parameters on the given data. In a 3D analysis data is binned in energy (i) and in two sky coordinates (j and k) so that any bin is labeled with three indices ijk. The number of observed counts $n_{\mathrm{obs},ijk}$ in the ijk-th bin is expected to follow a Poisson distribution, yielding the probability density

$$P_{ijk} = \frac{N_{ijk}^{n_{\mathrm{obs},ijk}} e^{-N_{ijk}}}{n_{\mathrm{obs},ijk}!}. \tag{4.8}$$

It represents the probability to observe $n_{\mathrm{obs},ijk}$ counts given the expected counts N_{ijk} from a model, where the latter corresponds to the predicted source counts in one bin as calculated in the continuous form in Eq. 4.7 (different notation). The likelihood is defined as the probability to observe the data $\mathcal{D}$, assuming model parameters Λ to be true [77]. It can be computed as the product of the individual Poisson distributions in all bins according to

$$\mathcal{L}(\mathcal{D} \mid \Lambda) = \prod_{i,j,k} P_{ijk} = \prod_{i,j,k} \frac{N_{ijk}^{n_{\mathrm{obs},ijk}} e^{-N_{ijk}}}{n_{\mathrm{obs},ijk}!}. \tag{4.9}$$

Often the log-likelihood is used instead of the likelihood because the equation simplifies to

$$\ln \mathcal{L}(\mathcal{D} \mid \Lambda) = \sum_{i,j,k} \left(n_{\mathrm{obs},ijk} \ln N_{ijk} - N_{ijk} - \ln(n_{\mathrm{obs},ijk}!)\right) = \sum_{i,j,k} \left(n_{\mathrm{obs},ijk} \ln N_{ijk} - N_{ijk}\right) \tag{4.10}$$

if one takes the natural logarithm and omits the last term, which is independent of the model parameters and therefore not useful in the estimation [77]. Varying the assumed model parameters Λ, the log-likelihood is maximized to find the optimized parameters Λ_{opt} describing the data best. Repeating this procedure for different models, they can be compared in terms of how well they describe the data. The Akaike Information Criterion (AIC) is an indicator of the relative quality of statistical models applied to a given set of data. It can be calculated from the maximized value of the likelihood function $\mathcal{L}_{\mathrm{max}}$ and the number of free parameters called *degrees of freedom (dof)* q [8]. Supposing a set of candidate models to describe the data, the minimum AIC value will indicate the preferred model. The AIC is computed as

$$\mathrm{AIC} = 2q - 2\ln \mathcal{L}_{\mathrm{max}}. \tag{4.11}$$

Given the AIC values of two models, where $\mathrm{AIC}_{\mathrm{min}}$ is the criterion for the preferred model (model 1) and $\mathrm{AIC}_{\mathrm{i}}$ the criterion for the other model (model 2), the relative probability p_{21} can be calculated. It is the probability of model 2 compared to model 1 and it is defined as

$$p_{21} = e^{\frac{\mathrm{AIC}_{\mathrm{min}} - \mathrm{AIC}_{\mathrm{i}}}{2}}. \tag{4.12}$$

The significance of that probability can also be estimated via

$$\sigma_p = \sqrt{\Delta\mathrm{AIC}} \tag{4.13}$$

where $\Delta\mathrm{AIC} = \mathrm{AIC}_{\mathrm{i}} - \mathrm{AIC}_{\mathrm{min}}$.

As mentioned before, the predicted model counts N_{ijk} depend on the chosen spectral and spatial parametrization ϕ_{spec} and ϕ_{spat} of the source. In my thesis, I relied on several spectral and spatial models of `gammapy` for the modeling of the background and the two analyzed sources (Crab Nebula and Boomerang SNR), which are defined in the following:

- `PowerLawSpectralModel`: Used for the spectral modeling of the Boomerang SNR, a simple power law spectral model is defined as

$$\phi_{spec}(E) = \phi_0 \cdot \left(\frac{E}{E_0}\right)^{-\Gamma}, \tag{4.14}$$

  containing the flux amplitude ϕ_0, the reference energy E_0 and the spectral index Γ.

- `PowerLawNormSpectralModel`: It is equivalent to the `PowerLawSpectralModel` with a normalized amplitude ϕ_0, then called *norm*. In the parameter naming system in `gammapy` the *index* is also replaced with the *tilt* parameter, which will be necessary knowledge in section 5.3.3. The `PowerLawNormSpectralModel` acts as a spectral model for the 3D background in this work, being the default background spectral model for such analyses in `gammapy`.

- `LogParabolaSpectralModel`: The log parabola is defined as

$$\phi_{spec}(E) = \phi_0 \left(\frac{E}{E_0}\right)^{-\alpha-\beta\log\left(\frac{E}{E_0}\right)} \tag{4.15}$$

with the flux amplitude ϕ_0, the reference energy E_0 and the spectral indices α and β. It is the model best describing the well-characterized Crab Nebula spectrum [15].

- `PointSpatialModel`: The model for a point source mathematically corresponds to a δ-function defined as

$$\phi_{spat}(lon, lat) = \delta(lon - lon_0, lat - lat_0) \tag{4.16}$$

where lon_0 and lat_0 are the two coordinates indicating the source position.

- `GaussianSpatialModel`: A Gaussian-shaped source emission is the most common non-point-like case. The normalized function is defined as

$$\phi_{spat}(lon, lat) = \frac{1}{2\pi\sigma^2} \exp\left(-\frac{1}{2}\frac{\theta^2}{\sigma^2}\right). \tag{4.17}$$

With the two coordinates lon and lat of a reference frame (*icrs* or *galactic*), the length of the semi major axis of the Gaussian σ and the sky separation to the model center θ, this 2D Gaussian is of symmetric nature. It can be adapted to an asymmetric Gaussian In `gammapy`. In that case, one has two additional dimensions of freedom, the eccentricity e ($0 < e < 1$) and the rotation angle ϕ of the semi major axis. Both versions have been employed for the modeling of the Boomerang SNR, the symmetric function also for the Crab Nebula.

4.3.3 Proprietary Framework - MARS

The MAGIC Analysis and Reconstruction Software (`MARS`) [82, 108] is a proprietary software of the MAGIC collaboration used for the reduction and analyses of data taken with the stereoscopic system of IACTs. It is a collection of programs and scripts written in `C++` and built on the `ROOT` framework [25]. The programs belonging to `MARS` that are of importance for this work are listed and explained below, referring to the corresponding standardized data levels as introduced in section 4.3.2.1. The automatic part of the analysis takes care of raw data, performing the calibration and image cleaning, equivalent to DL0 and DL1.

4.3.3.1 Quate

The application of data quality cuts is the first step of the analysis that is typically done by an analyzer. It has the objective to select only good quality data and exclude data taken under bad observing conditions, e. g., with poor atmospheric transmission.

In MARS, this is done with the program `quate`, typically running on data at `superstar` level (corresponds to DL1), but also applicable to `melibea` data (see next paragraph). `superstar` is part of the automatically executed routine, while its output corresponds to the first data level of Crab Nebula data processed in this work. For the selection, cuts can be applied in transmission (measured by the LIDAR subsystem), in run duration (to exclude runs with short exposure time), and in the measured Direct Current (DC) of the pixels, based on the expected value during standard data taking. The latter can reject accidentally triggered events, because it distinguishes in which case the measured signal was unexpectedly bright, too bright for a Cherenkov light flash.

4.3.3.2 Melibea

The last step of low-level data analysis in MARS is done with a subroutine called `melibea`. It has to be run both on the MC test data and the real data and uses RFs produced with the dedicated program `coach` (and optionally a Lookup Table (LUT)) to reconstruct direction, energy and hadronness parameters of all simulated and real events. The output `ROOT` files correspond to DL2 in the standardized framework.

4.3.3.3 Odie

`Odie` is a program that produces so-called θ^2-plots for an observation, which means it estimates the significance of the signal coming from the source region. It also calculates the aforementioned effective observation time (see section 2.3.1). A θ^2-plot is made counting the number of signal and background events in bins of the angular distance from the reconstructed source position θ squared (example in Fig. 4.13a). Subsequently, a cut in θ^2 is applied to select an ON region centered on the source inside of which to estimate the signal significance. The background counts are estimated from OFF regions as explained in section 4.3.2.2 and the significance is then computed with Eq. 17 from Li & Ma [70], assuming that ON and OFF counts follow Poisson distributions:

$$\mathcal{S} = \sqrt{2\left\{N_{\mathrm{ON}} \ln\left[\frac{1+\alpha}{\alpha}\left(\frac{N_{\mathrm{ON}}}{N_{\mathrm{ON}}+N_{\mathrm{OFF}}}\right)\right] + N_{\mathrm{OFF}} \ln\left[(1+\alpha)\left(\frac{N_{\mathrm{OFF}}}{N_{\mathrm{ON}}+N_{\mathrm{OFF}}}\right)\right]\right\}}, \tag{4.18}$$

where N_{ON} is the number of signal counts observed in the signal region, N_{OFF} is the number of background counts from the OFF regions, and α is the ratio of the OFF and ON exposures, called normalization factor α (see Eq. 4.3).

Note that this specific high-level product is mostly useful for point-like sources with a precisely known location, on which to center the ON region. In case of unknown location or multiple sources in the FoV, the squared property of the x-axis makes the interpretation of the result outside of the source region difficult. A different approach for visualization is more convenient, as pointed out in the next paragraph.

4.3.3.4 Caspar and SkyPrism

The two programs in MARS, which can be used to produce sky maps as high-level products are called `caspar` and `SkyPrism`. A sky map is a 2D representation of the observed region of the sky and can have multiple forms:

- **Count map**: Represents in which location in the sky the detector sees something.
- **Significance map**: Shows how significant the signal is in which region of the FoV, where the significance is $\sigma = \sqrt{\text{TS}}$, expressed in terms of the Test Statistic (TS) value.
- **Flux map**: Displays the measured signal in the sky region in physical quantities.

The necessity of this complementary representation of high-level data becomes clear, looking at Fig. 4.13. The two plots are produced for a simulated sky region with three bright point-like sources, which is immediately clear looking at the count map (Fig. 4.13b), but difficult or impossible to recognize in the θ^2-plot (Fig. 4.13a). Usually, additional sources in the FoV are much fainter than the main source of interest, therefore they are not detectable in a θ^2-plot and might spoil the background normalization.

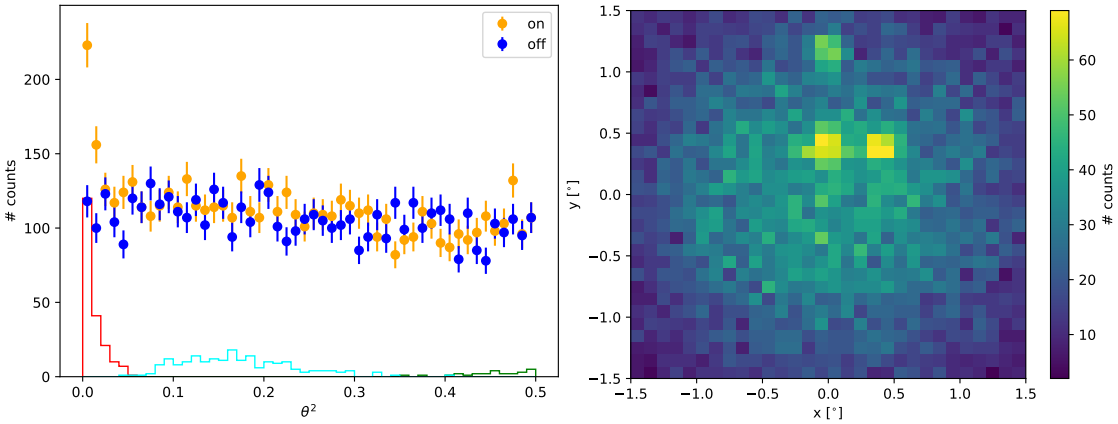

(a) (b)

Figure 4.13: θ^2-plot (a) and sky map (b) of a simulated FoV containing three point-like sources. To the right of the sky map a color bar indicates counts. The comparison demonstrates the importance of sky maps as a high-level complementary product for source detection, seeing as the three sources can easily be recognized in the sky map but are smeared out in the θ^2-plot if not located at the ON region center. From [97].

`Caspar` is a high-level program of MARS written in `C++` capable of producing sky maps starting from `melibea` files. Instead of accurately computing IRFs, it takes a more simplified approach. From the OFF regions in the data, `caspar` computes a background model and then randomly samples it to create a simple background expectation map [96].

The latter is smoothed with a symmetric 2D Gaussian kernel σ, in most cases chosen to be equal to the PSF of the system in the concerned energy range. Then, the background map is confronted with the smoothed event map, yielding sky maps of different types. The significance for each pixel is computed integrating the signal inside a Gaussian PSF, centered on that pixel. In `caspar`, the two available background estimation methods are the wobble and the blind method.

`SkyPrism` is a set of tools, based on `C++` and `python`, aimed at the analysis of γ-ray data with complex FoVs in an approach that considers and fits multiple spatial and spectral source models simultaneously [96, 102]. Compared to `caspar`, it uses a more advanced spatial likelihood approach for fitting and produces a complete set of IRFs for the observations. It realizes asymmetric MC-based IRFs and includes a background model that is not relying on an approximation. In comparison to `caspar`, it implements one additional background method, the exclusion method. `SkyPrism` was not used in this thesis, but is relevant to be mentioned for two reasons. Firstly, the analysis technique is based on a likelihood approach, similar to `gammapy`. Secondly, a cross check of the analysis published in the MAGIC paper about the Boomerang SNR [76] was performed with `SkyPrism`.

4.3.4 Systematic Uncertainties

Apart from the statistical uncertainties propagating through the analysis chain there are several systematic effects that require dedicated studies in IACT analysis. They arise not only from the finite knowledge of certain important detector or ambient factors, such as the light collection efficiency, the PMT performance, the atmosphere and the NSB but also from the techniques inherent to data analysis, for instance the background estimation and the conversion of ADC counts. Considering all these effects, the systematic uncertainties on spectral measurements with the MAGIC telescopes and `MARS` as studied in [15] are $\lesssim 15\,\%$ for the energy scale, $11 - 18\,\%$ on the flux normalization and ± 0.15 on the spectral slope. The systematic uncertainty on the reconstructed source position is $\lesssim 0.02\,^\circ$. The MAGIC collaboration states a systematic uncertainty on the 1D background estimation of $\lesssim 1\,\%$, which is reduced by a factor of two compared to before the enlargement of the trigger region in 2012 [15]. For this specific analysis there are two main additional systematic factors to consider. The first is the systematic uncertainty arising from the computation of background models for the 3D analysis. An example for a specific effect was found and shortly investigated in this work. It will be presented and discussed in sections 5.3.3 and 5.5. The second is induced by the asymmetric nature of the IRFs, which is however not yet realized as such in the GADF [38] and `gammapy`. Instead, IRFs are treated as radially symmetric quantities for the moment, although there are ongoing efforts to include the feature in the GADF. One has to be aware of these systematic uncertainties when evaluating and interpreting the results. Further studies testing their effect on the results would be necessary to quantify the global impact they have, but go beyond the scope of this thesis.

Chapter 5

Results and Discussion

This chapter is dedicated to the presentation of my results from the analysis of Boomerang SNR data taken with the MAGIC telescopes and their subsequent discussion. The leading idea of the project was to re-do the high-level analysis of archival data from a previous publication about the Boomerang SNR [76] using a novel and improved technique that is more appropriate for the analysis of extended sources, the 3D analysis. Additionally, I set up a 1D analysis pipeline to cross check spectral results of the novel method with a standard validated approach. I will present outcomes of a spectral and morphological study, obtained with the analysis tools `gammapy` and `pybkgmodel`. The new elements of this analysis were that I adopted a **standardized data** format (DL3) to execute a novel **3D analysis** with next-generation **open-source analysis software**. This makes it one of the first full spectro-morphological (3D) analyses with MAGIC data. The chapter can be divided into three main lines of work: A high-level re-analysis of Boomerang SNR data with `MARS` (section 5.1), testing the 3D analysis pipeline on Crab Nebula data (section 5.3) and applying it to the Boomerang SNR (section 5.4). Finally, I will discuss the impact of systematic uncertainties on my results, which are arising from the background estimation.

5.1 High-Level Re-Analysis of Boomerang SNR Data with MARS

The starting point for this work was to reproduce previously published results from [76] with the standard analysis software `MARS` of the MAGIC collaboration. The most recent versions of the software `MARS` and `ROOT` were used, being `MARS`-V3-1-0 and `ROOT6`. I re-analyzed the dataset from the published study amounting to ~ 122 h effective observation time. For this purpose, I used `melibea` files (see section 4.3.3.2) provided by the analyzer of the publication, directly employing the high-level programs `odie` (see section 4.3.3.3)

and `caspar` (see section 4.3.3.4) instead of going back to DL1 data and running the entire `MARS` analysis chain.

The dataset is composed of MAGIC data taken between 2017 and 2019. Correspondingly, the observations belong to the analysis periods ST.03.07, ST.03.08, ST.03.09, ST.03.10 and ST.03.11. Observational conditions in ST.03.09 were similar enough to ST.03.07 that MCs were only produced for one of those periods. All data taken in ST.03.09 will therefore also be intended when talking about ST.03.07 in the following, since the sample was effectively divided in four periods, combining ST.03.07 and ST.03.09. The data covers a zenith range of 30 ° to 50 ° and an azimuth range of approximately 0 ° to 50 ° and 320 ° to 360 °. Diffuse MCs, provided by the previous analyzers, have a maximum offset of 1.5 ° for ST.03.07, ST.03.08, and ST.03.10 and 2.5 ° for ST.03.11. They are for the zenith ranges 5 ° to 35 ° (low zenith distance) and 35 ° to 50 ° (medium zenith distance) enclosing the zenith range of the data sample. In 2017 (ST.03.07) several nights of data were taken with one single wobble pair (W0.50+158 and W0.50+338), amounting to $\sim$ 10 h. After that there was a slight change in the wobble angle of the pair and a third wobble position was added to be observed in ON mode, interleaved with the wobble pair (W0.50+160 and W0.50+340, W3). This detail about the wobble configuration will become important later. The configuration with a single wobble pair will be called wobble configuration 1 in the following. The three-wobble setup, used for the majority of the observations, will be called wobble configuration 2.

5.1.1 Signal Significance with Odie

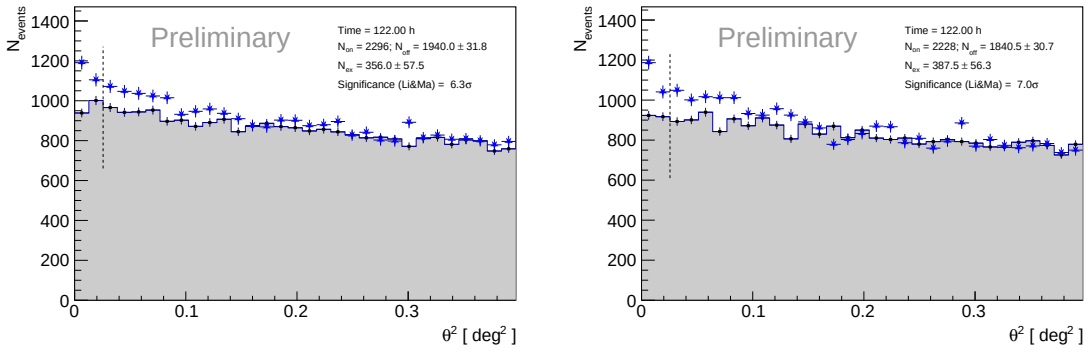

(a) (b)

Figure 5.1: θ^2-plots of the reference Head (a) and Tail (b) region above 0.2 TeV, plotting measured signal counts in blue in comparison to counts from the estimated background in black. The background contribution below the black data points is shaded in gray. A signal cut of 0.0256 deg^2 was applied and is indicated with a dashed black line, yielding a signal significance of the Head and Tail region above 0.2 TeV of 6.3 σ and 7.0 σ, respectively.

`Odie` was run on the two substructures of the source identified in the previous study

at energies above 0.2 TeV and specified in Tab. 1 of [76] (also relisted in the last rows of Tab. 5.10 and 5.11). In the following, they will be denoted as reference Head and Tail to distinguish from the positions and extensions obtained in this work, the Head and Tail (this work). Following the steps of the publication, the goal was to estimate the combined signal of each of these distinct emitting regions to assess the significance of it. I show two reproduced θ^2-plots in Fig. 5.1, containing the significance of the signal of the reference Head and Tail region from my re-analysis. The plots are both for energies above 0.2 TeV and a signal cut of $(0.16\,\mathrm{deg})^2 = 0.0256\,\mathrm{deg}^2$ (dashed black line in Fig. 5.1), corresponding to the signal inside a circular aperture defined as the extension of the reference Head and Tail positions in [76]. With these settings, the reference Head region reaches a signal significance of $6.3\,\sigma$ and the reference Tail region reaches $7.0\,\sigma$. Both are above the detection threshold of $5\,\sigma$ and in agreement with the $6.2\,\sigma$ (reference Head) and $6.9\,\sigma$ (reference Tail) in [76]. Note that the θ^2-plots show a clear indication for extended emission since the signal visibly stays elevated above the background beyond the chosen cut for signal integration.

5.1.2 Sky Maps with Caspar

With `caspar`, I introduced a slight change in the analysis, as compared to [76]. The dataset is split into two parts (wobble configuration 1 and 2 mentioned in section 5.1), and treated separately to assure that the complex wobble setup is correctly taken into account. Subsequently, the sky maps are stacked with an additional run of the program. While the energy threshold in [76] was set at 0.2 TeV, I here present results obtained with 0.2 TeV and additionally with a higher energy threshold of 0.4 TeV, as applied in the `gammapy` analysis. The reason for this change in energy threshold is that the original one was found to introduce visible systematic features in the significance histograms of the `gammapy` analysis, as will be seen below. On the other hand, the effect of a higher threshold on the morphology was found to be minimal. In Fig. 5.2 one can find the reprinted significance maps from [76]. Two significance maps for the old threshold of 0.2 TeV, as produced in this work, are shown in Fig. 5.3. The reproduced significance maps for the new threshold that will be compared to the `gammapy` maps are shown in Fig. 5.4. They are for the energy ranges 0.4 - 30 TeV (top left), 0.4 - 1.06 TeV (top right), 1.06 - 5.65 TeV (bottom left) and 5.65 - 30 TeV (bottom right). Note that there is a small but negligible difference compared to the energy ranges in Fig. 5.2, because I chose to use classic logarithmic energy binning, as was done for the `SkyPrism` cross check by the previous analyzers. Tab. 5.1 lists the PSF values used for the computation of the significance maps in the MAGIC publication and in this work. As can be seen in the table, the PSF is larger for low energies and smaller for high energies, at which the spatial resolution of the telescopes is enhanced. The Gaussian smoothing kernel σ was set to be equal to the PSF in each energy bin, therefore it is not listed separately. The color gradient for indicating the significance in `caspar` is not continuous, e. g., see Fig. 5.4). Instead, it is tuned such that a pixel with a significance below $3\,\sigma$ is drawn in blue, a pixel with a significance between $3\,\sigma$ and $5\,\sigma$, corresponding to a hint of emission, is colored red and a pixel with a significance above the detection threshold of

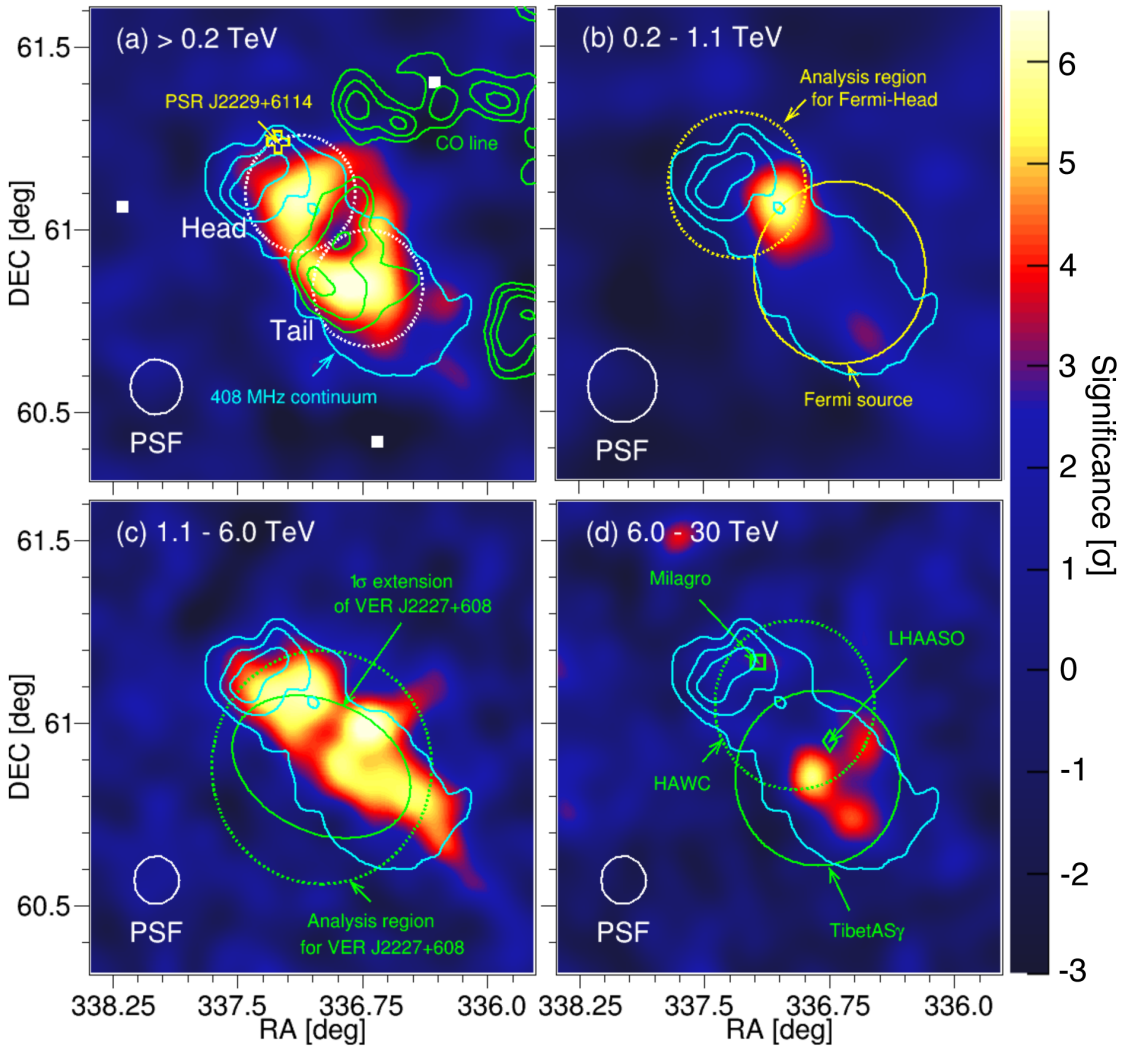

Figure 5.2: `Caspar` significance maps of the Boomerang SNR reprinted from the MAGIC publication [76]. The four maps are for energy ranges > 0.2 TeV (a), 0.2 - 1.1 TeV (b), 1.1 - 6.0 TeV (c) and 6.0 - 30 TeV (d). The PSF is indicated as a white circle at the bottom left of each panel. The three pointing positions of wobble configuration 2 are indicated with white rectangular markers in the top left panel. In the same panel, the position of the Boomerang pulsar PSR J2229+6114 is indicated with an empty yellow cross while the reference Head and Tail positions are enclosed in white dashed circles. Cyan contour lines in all panels trace the radio continuum emission at 408 MHz from [88], while green contour lines represent CO^{12} $(J = 1 - 0)$ line emission in the radial velocity range from -6.41 to $-3.94\,\mathrm{km\,s^{-1}}$ [69]. Several more emission centroids and regions, as reported by other γ-ray experiments, are indicated with yellow and green markers and shapes. For more detailed information the reader can consult [76].

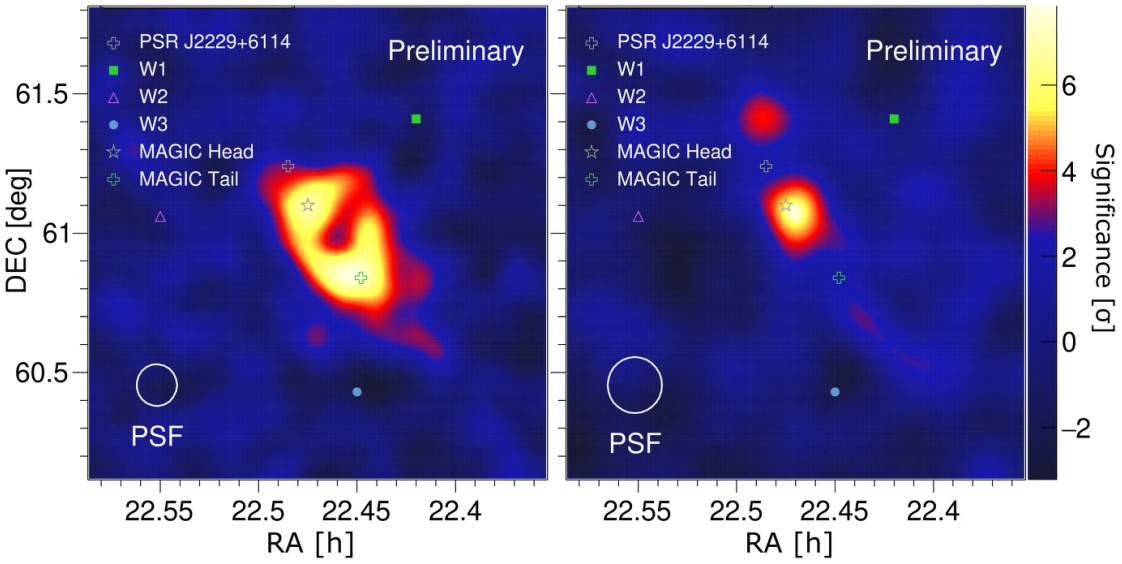

Figure 5.3: `Caspar` significance maps of the Boomerang SNR produced in this work for an energy threshold of 0.2 TeV: the full range between 0.2 TeV and 30.0 TeV (left panel) and the low energies between 0.2 TeV and 1.06 TeV (right panel). The PSF is indicated as a white circle at the bottom left of each panel. The three pointing positions of wobble configuration 2 are marked in each panel with a filled green square (W1), empty purple triangle (W2) and filled blue circle (W3). The position of the Boomerang pulsar PSR J2229+6114 is indicated with an empty gray cross while the reference Head and Tail positions are shown with an empty gray star and an empty green cross, respectively.

	0.4 - 30 TeV	0.4 - 1.06 TeV	1.06 - 5.65 TeV	5.65 - 30 TeV
`caspar` PSF [°] / smoothing kernel	0.053	0.071	0.046	0.046
`gammapy` correlation radius [°]	0.078	0.104	0.068	0.068

Table 5.1: PSF values (`caspar`) and correlation radii (`gammapy`) used for the computation of the significance maps in Fig. 5.3, 5.4, 5.5 and 5.11. They are listed together with the corresponding energy interval. Correlation radii were computed based on the PSF values according to section 5.2.

$5\,\sigma$ is displayed in yellow. This will become relevant for a comparison with the `gammapy` sky maps.

In the left panel of Fig. 5.3 and the top left panel of Fig. 5.4 both the reference Head and Tail regions, indicated with an empty gray star and an empty green cross, respectively, show a significant signal in the form of two hot spots at the respective positions. The signal reaches a maximum of $8\,\sigma$ around these locations. The two maps above 0.2 TeV in

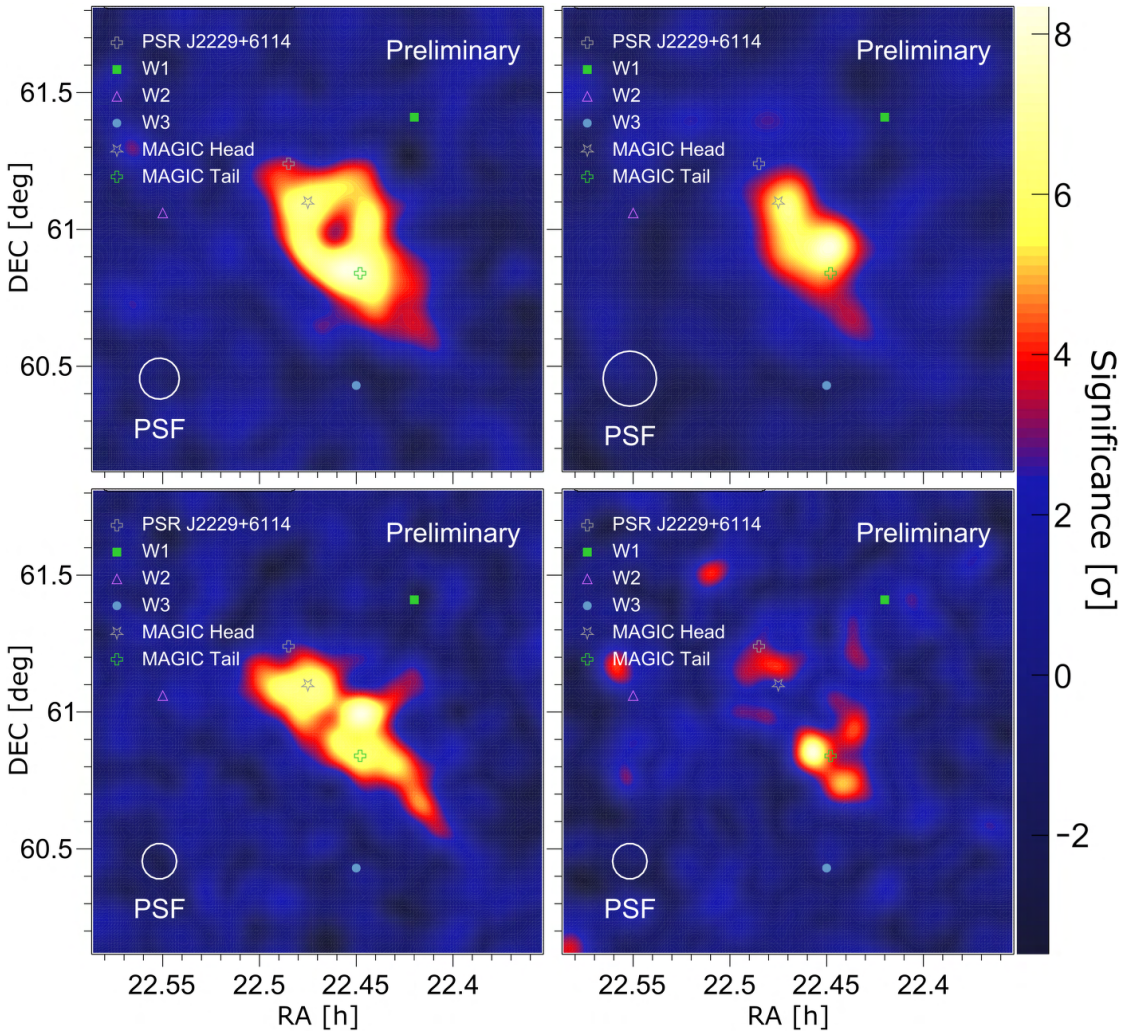

Figure 5.4: `Caspar` significance maps of the Boomerang SNR produced in this work. The four maps are for the energy ranges of 0.4 - 30 TeV (top left), 0.4 - 1.06 TeV (top right), 1.06 - 5.65 TeV (bottom left) and 5.65 - 30 TeV (bottom right). The PSF is indicated as a white circle at the bottom left of each panel. The three pointing positions of wobble configuration 2 are marked in each panel with a filled green square (W1), empty purple triangle (W2) and filled blue circle (W3). The position of the Boomerang pulsar PSR J2229+6114 is indicated with an empty gray cross while the reference Head and Tail positions are shown with a empty gray star and an empty green cross, respectively.

Fig. 5.3 are well compatible with the top panels in Fig. 5.2. Comparing the publication with the top panels in Fig. 5.4, there is only a minor change in the morphology of the Boomerang SNR, moving from a threshold of 0.2 TeV to 0.4 TeV. The single round hotspot in panel (b) of Fig. 5.2 and on the right panel of Fig. 5.3 becomes slightly more elongated and shifts its position from the reference Head towards the reference Tail region for a threshold of 0.4 TeV (top right panel of Fig. 5.4). Now viewing the top right and the bottom panels in Fig. 5.4, one can see that the source clearly exhibits an energy-dependent morphology. The emission region is visibly larger than the PSF, indicating that it is possible to resolve several structures of the source with the MAGIC telescopes. The signal of the γ-ray emission gradually shifts from the reference Head to the reference Tail, going from low to high energies. In the medium energy bin in the bottom left panel of Fig. 5.4 the emission spans the whole length of the SNR and it seems to be the dominating contribution to the overall emission. With the highest energies in the bottom right panel, the signal reaches a maximum of $6\,\sigma$ at the reference Tail region, whereas there is only a hint for emission in the reference Head region. In general, I find a good agreement between the results of my re-analysis (see Fig. 5.3 and 5.4) and the published maps (see Fig. 5.2), considering all the morphological elements that have been described. It seems there is a marginal difference in the overall significance of the signal, being $\sim 1 - 2\,\sigma$ higher for the maps of this work. A variation of that amplitude can be considered to arise from fluctuations and systematic uncertainties introduced by the limited suitability of the `caspar` program for analyses of extended sources and its approximative approach, and is therefore not significant. Concerning the modified treatment of the two wobble configurations in the `caspar` analysis, no significant change in the morphology could be distinguished. This was somewhat expected since the wobble pairs of the two configurations differ only by $2\,^\circ$ in wobble angle.

5.2 The 3D and 1D Analysis Pipelines

In this section, I will specify all the analysis settings and cuts that are part of the performed 3D and 1D analyses of the Crab Nebula and the Boomerang SNR. The pipeline takes MAGIC proprietary `melibea` files as input and produces all the high-level products considered in this study, e. g., significance maps, spectra from 3D and 1D analyses and optimized parameters of spectral and spatial models, fitted in the framework of 3D modeling and fitting procedures. The processing starts with the conversion of `ROOT` files to the standardized DL3 format.

Running the `DL3 Converter`, I specified a zenith range of $30\,^\circ$ to $50\,^\circ$ corresponding to the range in which the data lies and applied a hadronness cut of 0.325. This choice was made based on the following argument: For a 3D analysis the primary objective is to model and fit the remaining background, which becomes increasingly difficult for poor statistics. Therefore, a good hadronness parameter is not only constrained from below (a stricter hadronness cut leads to less hadronic events), but also from above (more hadronic events are better for a feasible and precise modeling of the background).

For a recommended hadronness efficiency of 0.85 in `SkyPrism`, the maximum returned hadronness cut was 0.325 and is the value I used. An optimization of the hadronness cut is in general important, but goes beyond the scope of this thesis, for which this approximation will be sufficient. I also applied a standard *size* cut of 50 photoelectrons, where the Hillas parameter *size* was introduced in section 2.2.3.4. The full-enclosure IRFs (the three main IRFs listed in section 4.3.2.4) were computed with a binning of 4 bins per decade on an estimated energy range of 50 GeV to 50 TeV, resulting in 12 bins in estimated energy and 15 bins in true energy with a ratio of estimated to true energy bins of 0.8. They were produced up to a maximum offset from the camera center of 1.5 °, considering that the MC simulations only provide reliable reconstruction up to that same maximum offset for two of the three periods.

At this point, the 3D and 1D analysis chains start to diverge. The main processing branch for this project was the 3D approach. However, I performed also a 1D spectral analysis with the given dataset in `gammapy`. While data from DL3 files can directly be reduced and fitted with spectral models in `gammapy` in the 1D geometry, the 3D analysis requires an intermediate step for the production of background models.

For the 3D case, I generated background maps for every period separately. `Pybkgmodel` was run with a stacked exclusion method. For the Crab Nebula, a circular exclusion region covering the whole emission region was set. For the Boomerang SNR, I chose an elliptical exclusion region covering the γ-ray emission as seen by MAGIC [76]. Specifications about the exclusion regions are given in Tab. 5.2, where the parameters in the last column are stated in ds9 format[1] as required in `pybkgmodel`. Furthermore, I chose the same energy binning as for the IRF production, a quadratic camera field of $6° \times 6°$ centered on the camera center and a spatial bin size of 0.3 ° in FoV longitude and latitude.

Having produced a template background model for each period, the background information was merged with the corresponding DL3 data run by run in `gammapy` to allow for subsequent data reduction and high-level analysis. In the following, I will shortly comment on the specifics of my 3D data reduction chain, making use of the `gammapy`

[1] https://ds9.si.edu/doc/ref/region.html

Source	Exclusion	Ra [°]	Dec [°]	Parameters
Crab Nebula	circular	83.63	22.01	radius [°]: 0.4
Boomerang SNR	elliptical	336.88	60.94	semi-major axis [°]: 0.59 semi-minor axis [°]: 0.38 position angle [°]: 130.0

Table 5.2: Exclusion regions applied in `pybkgmodel` and `gammapy` for the 3D analysis of the Crab Nebula and the Boomerang SNR. The region type is listed along with its center coordinates Ra/Dec and its parametrization in the ds9 format.

classes and spectral and spatial models defined in section 4.3.2.6. In the final parameter configuration of the analysis presented here, I set a spatial binsize of 0.02 ° and a lower energy threshold of 0.4 TeV (this choice will be explained and discussed in section 5.3.1). Each data run was reduced with the `MapDatasetMaker`, imposing a binned 3D geometry on the data. Additionally, I used the `SafeMaskMaker` to make a safe data range mask up to 1.5 ° maximum offset. I also set the safe mask for the effective area to be larger than 10 % of the maximum effective area, thereby introducing a lower energy threshold excluding energies at which the sensitivity is too low. The latter was done to assure the use of good quality data, but was found to not change the result, since the concerned data range was already excluded by the chosen lower energy threshold of 0.4 TeV. Furthermore, I required the `FoVBackgroundModel` to introduce a background spectral model, the `PowerLawNormSpectralModel`, using the default *tilt* value of 0. Running the `FoVBackgroundMaker` on each `Observation` with the *fit* method, the 3D background models from `pybkgmodel` were re-normalized to the given data. After running the three `Makers`, the resulting `MapDataset`s were stacked to produce a single `MapDataset`. During the stacking process IRFs are averaged. To avoid this, one would have to perform a joint instead of a stacked analysis in `gammapy`, fitting all datasets simultaneously without combining them. The main reason why this is not possible for faint sources like the Boomerang SNR is the lack of statistics. Accordingly, the stacked analysis was chosen, while keeping in mind the systematic effects that can be introduced by averaged IRFs. Starting from the stacked dataset, I ran the `ExcessMapEstimator` to produce sky maps for energy ranges listed along with their applied correlation radii in Tab. 5.1. The values of the correlation radii derive from the `caspar` PSF applied in the published analysis [76]. The objective was to match the amount of details in the `gammapy` and `caspar` sky maps. PSF values in `MARS` cannot be directly used as correlation radii in `gammapy`, since the two programs intrinsically adopt two different functions for correlating the signal. `Caspar` applies a 2D Gaussian whereas `gammapy` uses a `Tophat2DKernel` to calculate that significance. I maximized the common surface of these two normalized functions and got an adapted correlation radius for each value of the PSF used in `caspar`. In parallel to the sky maps, I also defined and fitted spectral and spatial models using the combined maximum likelihood technique. For all models, the *norm* parameter of the `PowerLawNormSpectralModel` for the background was fitted simultaneously. All fits were done in the energy range from 0.4 TeV to 30 TeV. Finally, I produced an SED running the `FluxPointsEstimator` on my `MapDataset`.

For the 1D case, I created and ran a `SpectrumDatasetMaker` on my `Observations`, reducing them to `SpectrumDataset`s and finally stacking them to get a single `SpectrumDataset`. Inside of the region chosen for spectrum fitting and flux points extraction the IRFs were averaged, instead of assuming IRF values from one single position. I set an energy threshold of 0.4 TeV and also applied the `SafeMaskMaker` with the same effective area cut as for the 3D data reduction. The `FoVBackgroundMaker` was replaced by the `ReflectedRegionsBackgroundMaker` and provided with the source exclusion region listed in Tab. 5.2. Finally, I performed a spectral fit in the energy

range from 0.4 TeV to 30 TeV on the stacked dataset and produced an SED running the `FluxPointsEstimator`.

5.3 Testing the Pipeline on Crab Nebula Data

To date, the Crab Nebula is one of the strongest and most stable sources detected in VHE γ-rays. It is also the most extensively studied and best-characterized source in this field, which is why it is suited for cross checks. Aiming at a validation of the 3D analysis pipeline, I started with Crab Nebula data at `superstar` level. For reasons of comparability the data was selected to match the specifications of the sample from the Boomerang SNR, such as the zenith range and MC periods. There was not enough Crab Nebula data available for period ST.03.08 (since it lasted only three months), so the period was excluded. While the Crab Nebula is a point source, the purpose of testing the 3D analysis pipeline required the use of diffuse MC simulations for its analysis. Therefore, I chose the same MC test productions as originally employed for the published analysis of the Boomerang SNR.

I applied the below listed cuts for data selection with `quate` (see section 4.3.3.1):

- A standard maximum DC cut of 3000 mA.
- A minimum duration cut of 10 min.
- A LIDAR transmission cut of 0.85 for the transmission at 9 km from the telescopes. I requested to keep only data that has simultaneous transmission measurements, to be conservative for the test data sample. All runs with missing LIDAR measurements were therefore excluded.

This selection results in a total of 29.5 h of good quality data from the Crab Nebula; 18.9 h for ST.03.07, 2.3 h for ST.03.10 and 8.3 h for ST.03.11.

Before moving to a standardized format, the selected sample was processed with `melibea` to reconstruct energy, direction and hadronness of each event. RFs, needed in the computation, were provided by the previous analyzers of the Boomerang SNR project. Note that special attention was paid to select the correct test MC samples for this step, the samples that were not used to train the RF.

5.3.1 Sky Maps

In Fig. 5.5, the Crab Nebula is seen as a bright spot approximately centered on the position of the Crab pulsar, indicated with the green star in each panel. The signal significance in the center of the top left panel (0.4 - 30 TeV) reaches values as high as 175 σ. Consecutively inspecting the top right, bottom left and bottom right panel of Fig. 5.5, it is visible that the flux falls quickly for increasing energy, due to less efficient

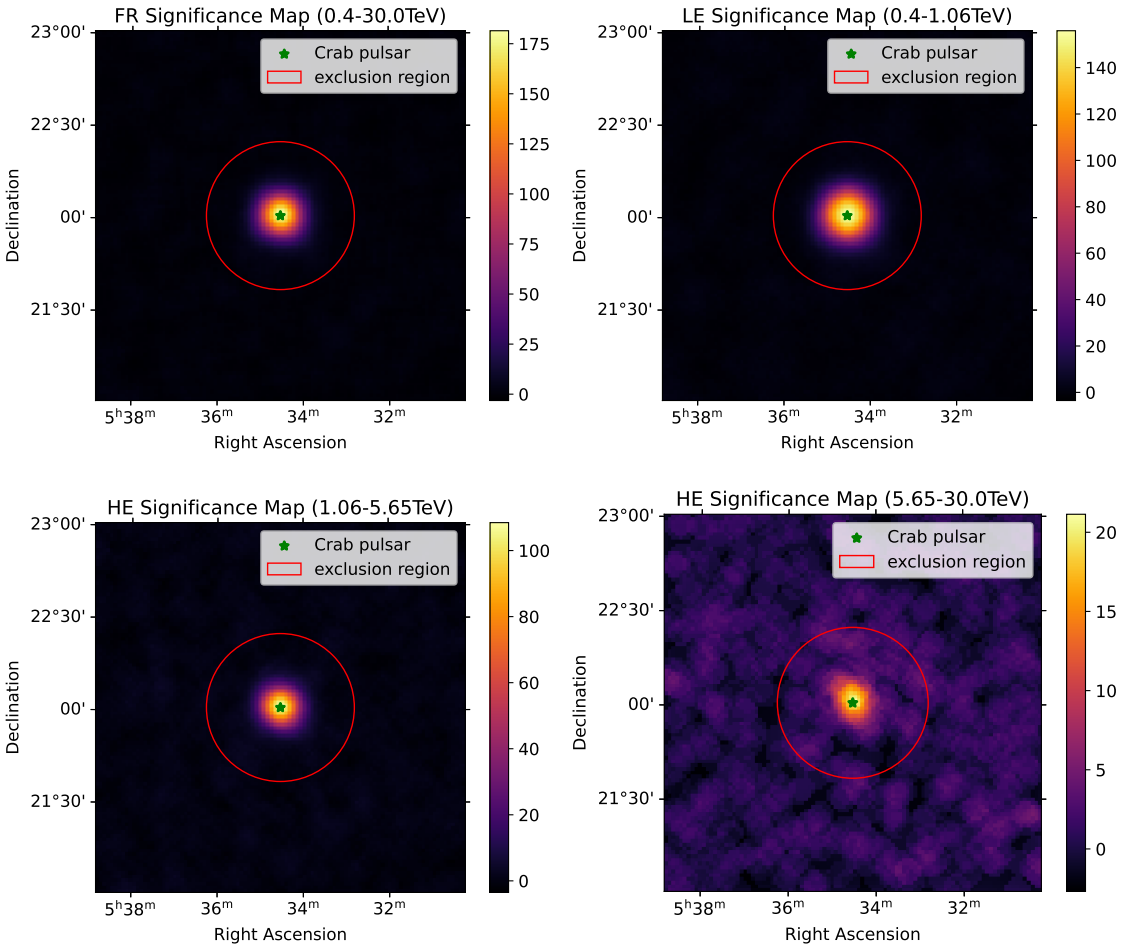

Figure 5.5: `Gammapy` significance maps of the Crab Nebula. The four maps are for the energy ranges of 0.4 - 30 TeV (top left), 0.4 - 1.06 TeV (top right), 1.06 - 5.65 TeV (bottom left) and 5.65 - 30 TeV (bottom right). In each panel, the position of the Crab pulsar is marked with a green star and the circular exclusion region used during the analysis is enclosed by a red line. The significance of the signal is indicated with a color bar to the right of each panel.

acceleration mechanisms of γ-ray-emitting particles and also decreasing sensitivity of the telescopes. The size of the central emission becomes smaller with increasing energy, because the angular resolution (the PSF of the system) improves at higher energies. One more element has to be noted in the bottom right panel of Fig. 5.5, which is an asymmetry of the central hotspot. As explained in section 4.3.4, `gammapy` does not take into account asymmetric IRFs, although in second approximation they are expected to have asymmetric behavior in general. The asymmetric shape is therefore expected to be due to a lack of precision in the IRF description. For the sake of this work the symmetric

approximation works fine enough.

Another way to assess a signal strength and detect potential systematic effects in an analysis is to look at the significance histograms of a significance map, as presented in Fig. 5.6. Analogous to Fig. 5.5, the four panels correspond to the four already specified energy ranges. In each panel, the background distribution of significance values is drawn in blue (labeled *off bins*) and the total distribution is drawn in salmon (labeled *all bins*). In all the histograms, one can see a clear signal that is incompatible with only

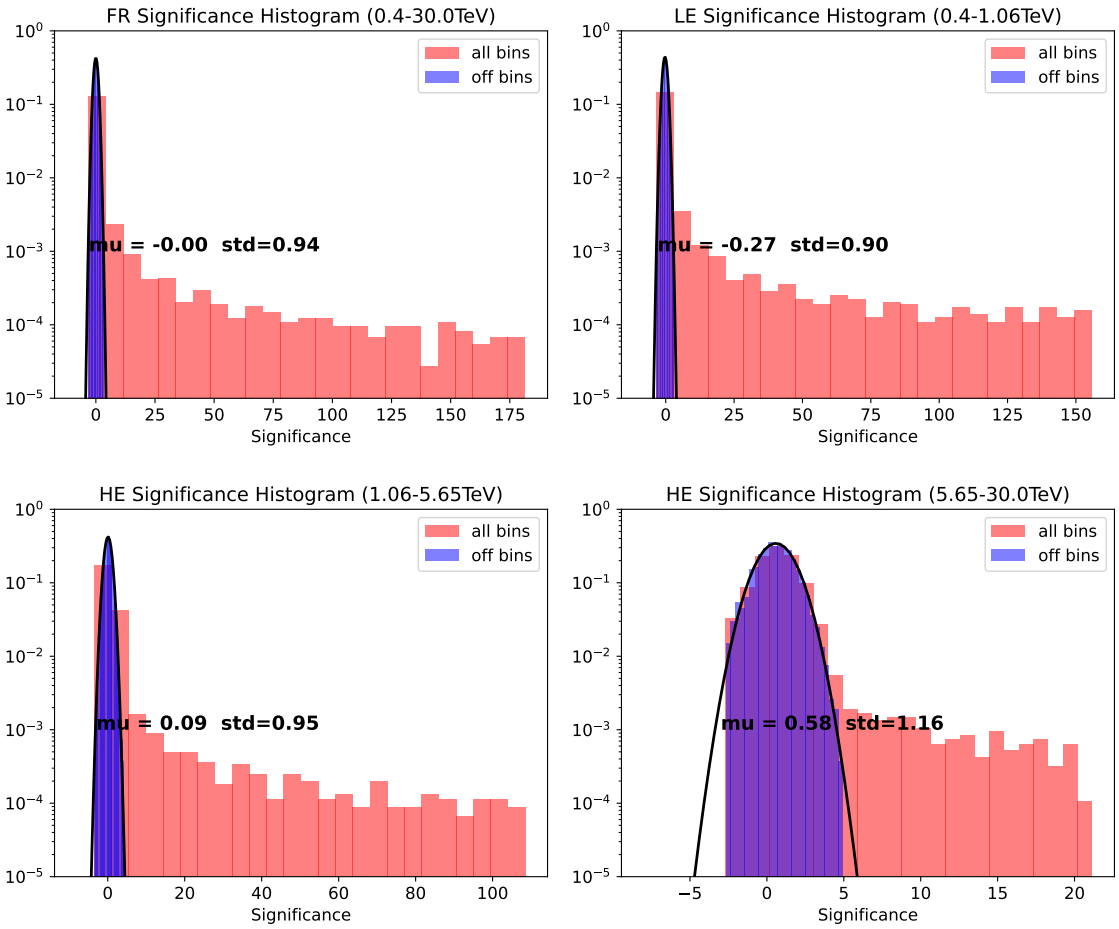

Figure 5.6: Normalized signal and background significance histograms of the Crab Nebula. The four maps are for the energy ranges of 0.4 - 30 TeV (top left), 0.4 - 1.06 TeV (top right), 1.06 - 5.65 TeV (bottom left) and 5.65 - 30 TeV (bottom right). In each panel, the background distribution of significance values is plotted in blue color (labeled *off bins*) and the total distribution in salmon color (labeled *all bins*). The background is fitted with a Gaussian function (fit indicated with a black line), yielding a mean value μ and a standard deviation σ (printed in black).

a background distribution. The choice of the energy threshold of 0.4 TeV, compared to the original threshold of 0.2 TeV, is based on an effect that was discovered in these histograms. With the original threshold, I found an asymmetric feature in the lowest energy range (0.2 TeV to 1.06 TeV) of the background significance distribution both for the Crab Nebula and the Boomerang SNR. The effect was much stronger for the SNR, due to the larger dataset of more than 100 h of observations, but also clearly visible for the Crab Nebula, as shown in the left panel of Fig. 5.7. Successively, the particularity in the shape of the distribution could be removed in both datasets by applying a higher energy threshold, see right panel of Fig. 5.7. The effect could be explained by the fact that the computation of the IRFs marginally differs between the `MARS` routines and the `DL3 converter`, possibly demanding for a more conservative threshold in `gammapy`.

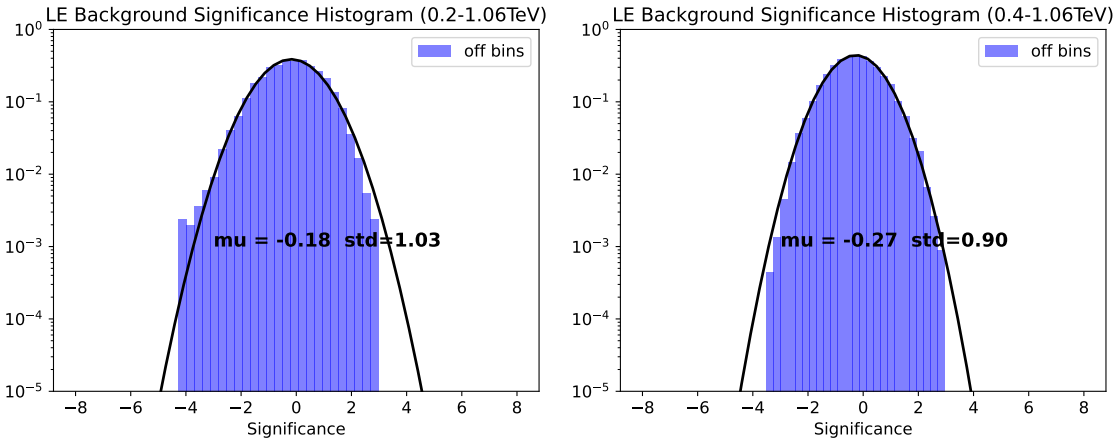

Figure 5.7: Background significance histograms of the Crab Nebula for 0.2 TeV (left) and 0.4 TeV (right) energy threshold. In each panel, the background distribution of significance values is plotted in blue color (labeled *off bins*). The background is fitted with a Gaussian function (fit indicated with a black line), yielding a mean value μ and a standard deviation σ (printed in black). The left panel shows an asymmetric feature at the left end of the background distribution.

The mean μ and standard deviation σ of a background signal distribution are expected to be $\mu = 0$ and $\sigma = 1.0$. While the standard deviation in the histograms in Fig. 5.6 fulfills this behavior (excluding fluctuations due to statistics) the mean μ seems to shift from negative to increasingly positive values for increasing energy. It goes from $\mu = -0.27$ in the top right panel to $\mu = 0.09$ in the bottom left panel to $\mu = 0.58$ in the bottom right panel. Uncertainty intervals of the order of ~ 0.01 on the mean were found to not solve this discrepancy. It will be further investigated and discussed in sections 5.3.3 and 5.5.

Before moving to the results obtained by modeling and fitting the data, I would like to stress that identifying effects such as the asymmetric feature at low energies and the systematic shift of the mean in the significance histogram of the background was the main motivating factor for a test of the 3D analysis pipeline on Crab Nebula data.

Thus, I was able to rule out, that these effects were specific to my source of interest, the Boomerang SNR, and to conclude that they are more likely linked to a systematic influence in the analysis.

5.3.2 Spectral and Spatial Analysis

In general, the Crab Nebula spectral model for all analyses was chosen to be a `LogParabolaSpectralModel` (`lp`) including an amplitude ϕ_0 and two spectral indices α and β as free parameters. Performing the 3D analysis, I fitted two different spatial models; a `PointSpatialModel` (`point`) entirely described by two spatial coordinates (Ra/Dec) and a symmetric `GaussianSpatialModel` (sym. `gauss`), involving a Gaussian width parameter σ in addition to the coordinates. The main spectral and spatial results of this work on the Crab Nebula are visualized in Fig. 5.8 (fitted spectra and flux points from 3D and 1D analyses) and Fig. 5.9 (Gaussian spatial model superposed on a full range significance map) and quantified in the form of spectral and spatial fit parameters in Tab. 5.3 and 5.4.

In Fig. 5.8, I plot the spectrum of the Crab Nebula, as obtained with different analysis methods. In the top panel, it contains the fitted spectrum in the range from 0.4 TeV to 30 TeV from a 3D point-like analysis (light blue), from a 3D Gaussian analysis (navy blue) and from a 1D spectral analysis (dark blue). Moreover, I show the Crab Nebula spectrum from the performance study of the MAGIC telescopes in red [15] and the 3D and 1D flux points/ULs in yellow and orange, respectively. The shaded gray band around each curve indicates the error region. The lower panel plots the residuals, computed as the difference between the obtained model and the reference model, divided by the obtained flux errors. While the agreement between all the curves and the flux points is very good at low energies, the 1D fit falls a bit more rapidly above several TeV. The error bands of the fitted models at these energies are almost touching but not overlapping. The SED points from 3D and 1D analysis above 10 TeV are slightly shifted to lower or higher flux values and might be due to systematic uncertainties not fully propagated through the analysis. In general, these SED points have to be considered with much care, due to the very approximative method with which they were estimated. Instead, the butterfly areas around a fit are more suitable to evaluate a spectrum. Particularly the 3D Gaussian analysis performs very well under that aspect, reproducing almost exactly the MAGIC reference spectrum from Aleksić et al. [15], judging from its spectrum and residuals. Also the 3D point-like analysis is compatible inside the error bands. To compare the models, we can also look at the spectral results in numbers stated in Tab. 5.3. The reference spectral parameters from [15] are listed in the last row of the table. Fitted values of the amplitude ϕ_0 and the two spectral indices α and β_{10} of the `LogParabolaSpectralModel` are stated along with statistical error confidence intervals. β_{10} refers to the spectral index in the $\log_{10}$ notation, to distinguish between the two common parametrizations of the `LogParabolaSpectralModel`; one based on the natural logarithm and one based on the $\log_{10}$. Considering only the statistical uncertainties, the uncertainty intervals of the measured amplitudes do not always strictly overlap,

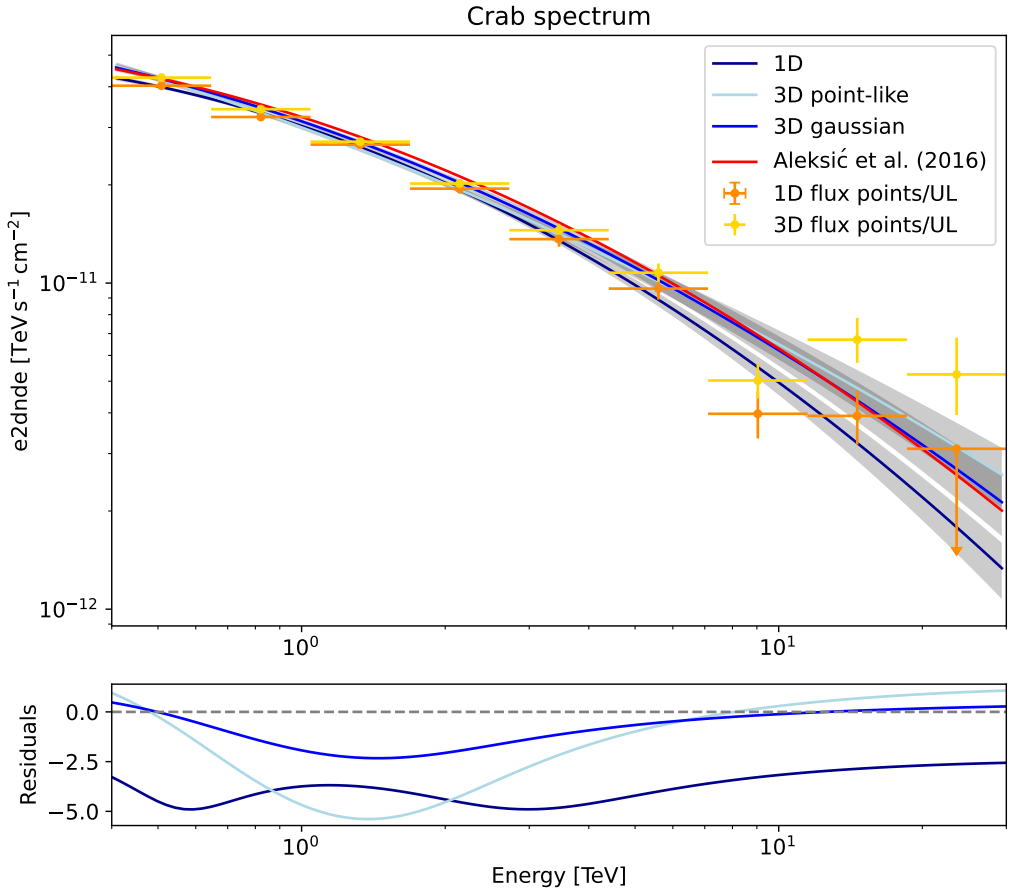

Figure 5.8: `LogParabola` spectrum of the Crab Nebula from 3D and 1D analyses (in shades of blue), together with 3D and 1D flux points/Upper Limits (ULs) (yellow and orange) and a reference spectrum [15] (red). The bottom panel displays the residuals of the fits, calculated as the difference between the obtained model and the reference model, divided by the obtained flux errors. The plot contains the 3D point-like fit in light blue, the 3D Gaussian fit in navy blue and the 1D purely spectral fit in dark blue. Data has been considered in the energy range 0.4 - 30 TeV for each fit and error bands are drawn in gray around the optimized model curve. The 3D Gaussian fit comes with the smallest residuals.

though they do in most cases. The spectral indices are not directly comparable, since a change in α can compensate for a change in β if both are left free. However, they are in general consistent, being of the same order of magnitude. Again, the 3D Gaussian parameters show the best performance compared to the reference spectral parameters. Taking into account systematic uncertainties stated in section 4.3.4, which amount to around $\sim 0.50 \times 10^{-11}\,\mathrm{cm}^{-2}\,\mathrm{s}^{-1}\,\mathrm{TeV}^{-1}$ for the amplitude (from the 11 - 18 % systematic uncertainty on the flux normalization) and to 0.15 for the spectral indices, all results from the 3D analyses and the 1D analysis are consistent among themselves and also with

the reference values. In the next paragraph, I will discuss how the Gaussian and the point-like 3D model can be further confronted not only in terms of the spectral part.

	Φ_{spat}	Φ_{spec}	ϕ_0 [$\text{cm}^{-2}\,\text{s}^{-1}\,\text{TeV}^{-1}$]	α	β_{10}
3D	`point`	`lp`	$(3.00 \pm 0.05) \times 10^{-11}$	2.53 ± 0.02	0.13 ± 0.04
3D	`gauss`	`lp`	$(3.13 \pm 0.05) \times 10^{-11}$	2.50 ± 0.02	0.20 ± 0.04
1D	-	`lp`	$(3.03 \pm 0.05) \times 10^{-11}$	2.49 ± 0.02	0.29 ± 0.05
1D [15]	-	`lp`	$(3.39 \pm 0.09_{\text{stat}} \times 10^{-11})$	$2.51 \pm 0.02_{\text{stat}}$	$0.21 \pm 0.03_{\text{stat}}$

Table 5.3: Spectral fit results for the Crab Nebula, obtained with a 3D point-like, a 3D Gaussian and a 1D spectral modeling. In the last row, reference values of the Crab Nebula spectrum from [15] are given. The table states the type of spatial model Φ_{spat}, the type of spectral model Φ_{spec} and the three describing parameters: the amplitude ϕ_0 and the spectral indices α and β_{10}. β_{10} denotes the spectral index in the $\log_{10}$ notation. All spectral models are given at a reference energy of $E_0 = 1.0\,\text{TeV}$.

	Φ_{spat}	Ra [°]	Dec [°]	σ [°]
3D	`point`	83.6312 ± 0.0006	22.0189 ± 0.0005	-
3D	`gauss`	83.6306 ± 0.0007	22.0194 ± 0.0006	0.0239 ± 0.0008

Table 5.4: Spatial fit results for the Crab Nebula, obtained with a 3D point-like and a 3D Gaussian modeling. The table states the type of spatial model Φ_{spat}, the fitted coordinates Ra/Dec and the width of the Gaussian fit σ, if applicable.

The results of a model quality assessment with the AIC (defined in section 4.3.2.6) for the Crab Nebula are shown in Tab. 5.5, confronting a point-like and a Gaussian spatial model. Compared to the classical likelihood ratio test using Wilk's theorem, the AIC is applicable for model comparisons of two models that are not necessarily nested. Since not all spatial models tried on the Boomerang SNR were nested, I had to use the AIC for the performed model quality tests to be consistent. For each statistical model Tab. 5.5 states the value of $-2 \times \log(\mathcal{L}_{\text{max}})$ as returned by the fitting procedure, the number of *dof* and the calculated AIC. With an AIC of 33261.98 compared to 33486.97, the Gaussian model is preferred. This supports the qualitative results from the spatial fit residuals of both models, as shown in Fig. A.17 and Fig. A.15 of appendix A. Using Eq. 4.12, I estimated that the point-like model is 10^{-49} times as probable as the Gaussian model, meaning that the probability is compatible with $p_{21} = 0$. Then, applying Eq. 4.13, I found the significance of that probability to be as high as $15.0\,\sigma$.

Considering only the spectrum the 3D point-like fit seems to be reasonably compatible with the reference Crab Nebula spectrum and the 3D Gaussian fit. However, taking into account the non-homogeneous spatial residuals of the point-like fit in Fig. A.17 and a model quality comparison of the Gaussian and point-like model with the AIC, the Gaussian description of the data eventually was found to be much more probable and preferred over the point-like description.

Φ_{spat}	Φ_{spec}	$-2 \times \log(\mathcal{L}_{\text{max}})$	*dof*	AIC
`gauss`	`lp`	33249.98	6	33261.98
`point`	`lp`	33476.97	5	33486.97

Table 5.5: AIC for two spatial models of the Crab Nebula: the point-like model (`point`) and the Gaussian model (`gauss`). AIC values are computed from the maximized log-likelihood values $\log(\mathcal{L}_{\text{max}})$ and the number of *dof* of the total fitted model, including spatial and spectral components. For the spectral component of both models a `LogParabola` (`lp`) was used.

The spatial results of the preferred 3D Gaussian analysis are plotted in Fig. 5.9 and given in numbers in Tab. 5.4. Also the coordinate fit of the point-like case is listed in the table. The fitted positions of the Crab Nebula are in very good agreement with each other, as well as with the values from the SIMBAD Astronomical database[2]: Ra

[2] http://simbad.cds.unistra.fr/simbad/

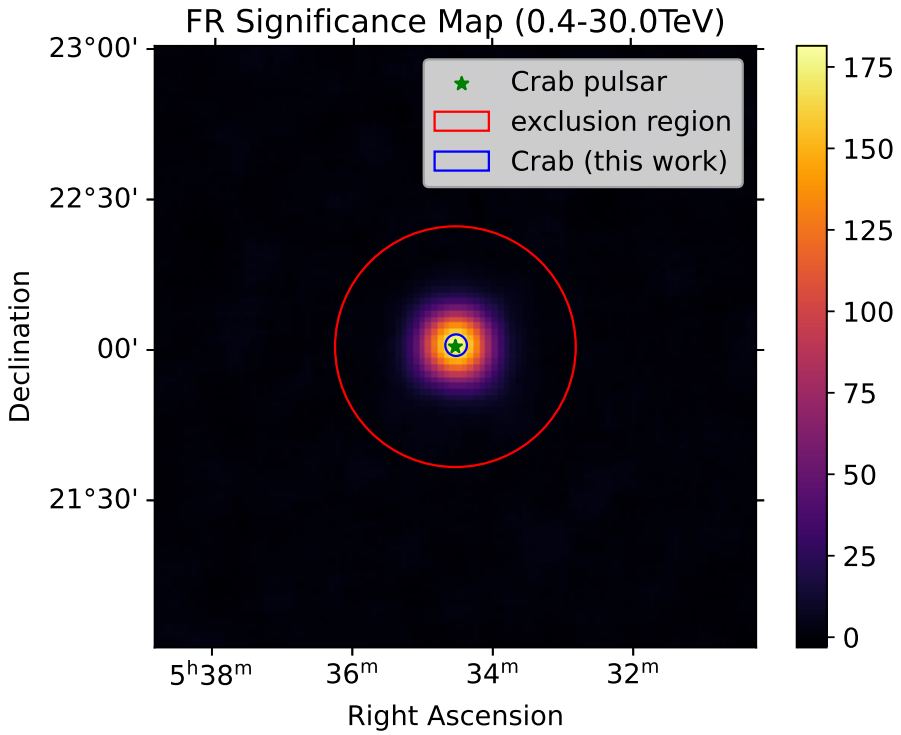

Figure 5.9: Superposition of the Gaussian spatial fit result on a `gammapy` significance map of the Crab Nebula for the full range between 0.4 TeV to 30 TeV. The exclusion region used for the analysis is drawn in red, the Crab pulsar is marked with a green star and the $1\,\sigma$ contour of a 3D Gaussian fit to the data is plotted in blue, being $\sigma = (0.0239 \pm 0.0008)\,^{\circ}$.

= 83.63 °, Dec = 22.01 °. The 3D Gaussian approach also yielded a Gaussian extension parameter of $\sigma = (0.0239 \pm 0.0008)^\circ$ corresponding to a 68 % containment radius of $r_{68} = (0.036 \pm 0.001_{\text{stat}})^\circ$ for the Crab Nebula (see Tab. 5.6). The systematic uncertainty on the pointing accuracy of the MAGIC telescopes is $\lesssim 0.02^\circ$ [15]. The Gaussian σ of the measured extension slightly exceeds this pointing accuracy, hinting at the measured extension being an actual physical extension and not only resulting from inaccuracies in the pointing. While this may not suffice to unambiguously claim the detection of extended emission from the Crab Nebula, it sets the most stringent UL for the Crab Nebula extension ever measured by the MAGIC telescopes. The last such measurement by MAGIC was reported in 2008, with an upper limit for the Gaussian extension σ of $2.2' \sim 0.037^\circ$ [11]. To date, only a few measurements of the extension of this source in the HE and VHE regime have been done, which are listed in Tab. 5.6 for comparison. The *Fermi*-LAT collaboration in 2018 reported the first positive measurement of the Crab extension [6]. For the Crab Nebula they state a 68 % containment radius of the best-fit Gaussian model of $r_{68} = 0.030^\circ$, where data has been considered in the range from 1 GeV to 1 TeV. They were followed in 2020 by a publication from H.E.S.S. [56], stating a Gaussian width of $\sigma = 52.2''$, which corresponds to a 68 % containment radius in degrees of $r_{68} = 0.022^\circ$ between 0.7 TeV and 30 TeV. The most recent investigation, however, came out in 2024 as a combined study of the energy-dependent extension of the Crab Nebula by *Fermi*-LAT and H.E.S.S. [7]. In this article, the Crab Nebula extension was re-measured independently by both experiments, using the `gammapy` package instead of the respective proprietary software. The publication quotes an extension of around $r_{68} = 0.014^\circ$ with H.E.S.S. above 10 TeV and an extension of $r_{68} = 0.035^\circ$ with *Fermi*-LAT above 1 GeV. Additionally, they combined the two datasets and performed an energy-dependent study of the Crab Nebula extension. Looking at the reported values in Tab. 5.6, it is evident that the UL I provided should be on the verge of a detection, if previous measurements of *Fermi*-LAT and H.E.S.S. are to be trusted.

	Energy range	r_{68} [°]	Δr_{68} [°]	
Fermi-LAT (2018)	1 GeV - 1 TeV	0.030	$\pm 0.003_{\text{stat}}$	$\pm 0.007_{\text{sys}}$
Fermi-LAT (2024)	> 1 GeV	0.035	$\pm 0.003_{\text{stat}}$	
MAGIC UL (2008)	> 500 GeV	0.055	-	
MAGIC UL (this work)	0.4 TeV - 30 TeV	0.036	$\pm 0.001_{\text{stat}}$	
H.E.S.S. (2020)	0.7 TeV - 30 TeV	0.022	$\pm 0.001_{\text{stat}}$	$\pm 0.003_{\text{sys}}$
H.E.S.S. (2024)	> 10 TeV	0.014	$\pm 0.005_{\text{stat}}$	

Table 5.6: Extension measurements and ULs of the Crab Nebula in HE and VHE γ-rays, reported by *Fermi*-LAT, H.E.S.S. and in this work. The table lists the energy range of the measurement, the 68 % containment radius of the fitted 2D Gaussian and the uncertainty interval. ULs are labeled as such.

Concluding, the test of the 3D analysis pipeline with Crab Nebula data has been successful. The reasonable results for the spectra and sky maps of the Crab Nebula validated the 3D analysis pipeline for usage on other sources. Furthermore, two systematic effects

could be identified, being the asymmetric feature in the background histograms at low energy and the systematic shift of the mean in the background significance histograms. Both are related to the background and the former could also be reduced as a consequence. For the description of the emission, a Gaussian spatial model is clearly preferred over a point source model. Using the 3D analysis, I was able to set the most stringent UL for the extension of the Crab Nebula with MAGIC data so far. The UL is compatible with actual measurements by H.E.S.S. and *Fermi*-LAT and seems to be on the verge of a detection. With a typical resolution of around 0.07 °, IACTs are not able to directly measure the extension of sources below that limit, but my result demonstrates that it may be possible to reveal the extension of marginally extended sources with novel analysis techniques, such as the 3D analysis.

5.3.3 Study of the Spectral *Tilt* Parameter of the Background

As mentioned in section 5.3.1, I found that the mean of the background significance histograms was systematically shifted to higher values with increasing energy. It is most probable that the effect is related to the background estimation or treatment in the 3D analysis chain. Given the novel analysis technique, the background is at the moment a major unknown influence on the systematic uncertainties and will require detailed studies, which go beyond the scope of this work. Here, I will give a glimpse at a brief supplementary check done in this work to identify if the background spectral model parameters could be at the origin of the systematic shift of the mean in the background significance histograms.

For this purpose, I repeatedly ran the 3D analysis pipeline described in section 5.2 on the Crab Nebula, keeping all the specified settings, but varying the *tilt* parameter of the background's `PowerLawNormSpectralModel`. The values I tried are the following: 0, -0.025, -0.05, -0.075 and -0.1. For each energy range, I then plotted the mean of the background significance histogram against the *tilt* parameter and obtained the graph in Fig. 5.10. It displays data points in light blue for the low energies (0.4 - 1.06 TeV), in navy blue for the medium energies (1.06 - 5.65 TeV) and in dark blue for the highest energies (5.65 - 30 TeV). The statistical uncertainty on the mean was found to be of the order of ~ 0.01 for all data points. In each energy range the mean seems to follow a linear relation. Indeed, the combination at a *tilt* value of 0 does not seem to be the optimal one, since the spread of the mean values of different energy bins is quite large. The behavior seems to be less dispersed and more random rather than systematic around a *tilt* of -0.05. Concluding, this brief investigation seems to hint at two different things: Firstly, the background spectral model could need some adjustments for a better description of the background. This could be either a change in the corresponding parameters (e. g., the *tilt* of the spectrum) or an altogether change in the model type, which has not been tried in this work, but may be considered in future works. And secondly, having a look at Fig. 5.10 again, it can be noted that there is a degeneracy in the optimization of the *tilt* for different energy ranges. This probably traces back to the computation of the template background models, indicating that our methods or the used data for the

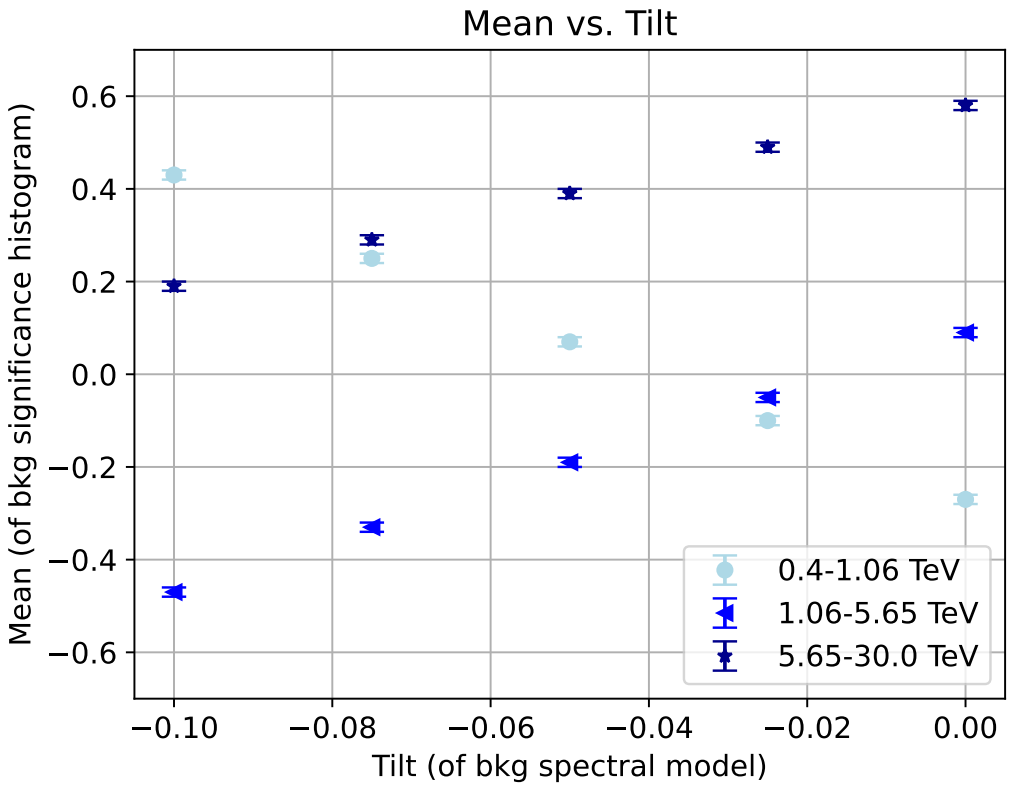

Figure 5.10: Plot of the mean value of background significance histograms of the Crab Nebula against the *tilt* parameter of the background spectral model. Varying the *tilt* parameter in steps of 0.025 between 0 and −0.1, the mean shows a linear behavior for all three considered energy ranges: 0.4 - 1.06 TeV (light blue), 1.06 - 5.65 TeV (navy blue) and 5.65 - 30 TeV (dark blue).

construction of 3D background cubes could be improved to reduce this degeneracy.

5.4 Applying the Pipeline to Boomerang SNR Data

Following the validation on Crab Nebula data, I applied the 3D analysis pipeline to my dataset of Boomerang SNR observations, of which the results will be presented in this section.

5.4.1 Skymaps

In Fig. 5.11, the significance maps of the Boomerang SNR for the four usual energy ranges are displayed. It is important to recall the aforementioned difference in the color scale of the `caspar` and `gammapy` maps, to correctly interpret these results. One particular aspect of this difference is important to remind here: The tuned color scale of `caspar` makes it much easier to distinguish a signal from the background, because all

points that have a significance below $3\,\sigma$ are colored in blue. Furthermore, it has to be noted that due to a different way of correlating the signal the maps of `gammapy` appear more pixelised. Comparing the `caspar` significance maps in Fig. 5.4 with Fig. 5.11, I find a good agreement not only of the rough energy-dependent morphology related to the signal inside the reference Head and Tail regions, but also of several smaller structures, e. g., the double emission peak inside the reference Tail region at energies from 5.65 TeV to 30 TeV (bottom right panel in Fig. 5.4 and Fig. 5.11). Also the complex shape of the emission region between 1.06 TeV and 5.65 TeV in the bottom left panel of Fig. 5.4 is well reproduced in the same panel of Fig. 5.11. The difference of around $\sim 2\,\sigma$ in the maximum significance of the signal between Fig. 5.4 and 5.11 is on the verge of the expected amplitude of fluctuations. It is on the order of the mentioned difference between the sky maps in Fig. 5.2 and 5.4. Part of the effect be due to non-optimal correlation radii, used in the computation of the significance maps. The difference in estimated significance could indicate that the two distinct correlating functions of `gammapy` (`TopHat2DKernel`) and `caspar` (Gaussian kernel) were not sufficiently approximated via a maximization of the common surface. Looking at the bottom right panel of Fig. 5.11 the Tail region stands out at a level of about $4-5\,\sigma$, which represents at least a strong hint for emission. Meanwhile, part of the Head region close to the pulsar position also exhibits a slight increase of signal with respect to the background. This slight hint of γ-ray signal is also seen as a feature in the bottom right panel of Fig. 5.4, but not in the corresponding energy bin of [76] (see Fig. 5.2). For the Head region, a signal above several TeV has not been detected so far, but it is one of the most controversial of the facets of the Boomerang SNR that are under investigation by the community. Not only MAGIC, but also LST-1, LHAASO, VERITAS and future γ-ray observatories are interested to clarify this aspect, substantiated by the recent publications about the source [76, 30, 89].

The significance histograms of the signal and the background in Fig. 5.12 can also be used to evaluate results. Again, the background bins are fitted with a Gaussian and the mean μ and standard deviation σ are printed on the corresponding panel. The four histograms indicate that in each energy bin the distribution of significance values from all spatial bins is not compatible with the distribution from off bins only, meaning that there is a γ-ray signal in the map. While this excess is most notable between 0.4 TeV and 30 TeV (top left panel in Fig. 5.12) and clearly present in the first two energy ranges (top right and bottom left panels in Fig. 5.12), it is less obvious but visible in the highest energy bin between 5.65 TeV and 30 TeV (bottom right panel in Fig. 5.12). Note that a systematically deviating mean of the background distributions, which should be $\mu = 0$ in theory, is evidenced in these histograms. The same effect was identified in the results from the Crab Nebula and it goes also in the same direction as for the Crab Nebula in all energy bins (see section 5.3.1). This indicates that it is a source-independent effect, related to a systematic influence in the analysis. It was investigated in section 5.3.3.

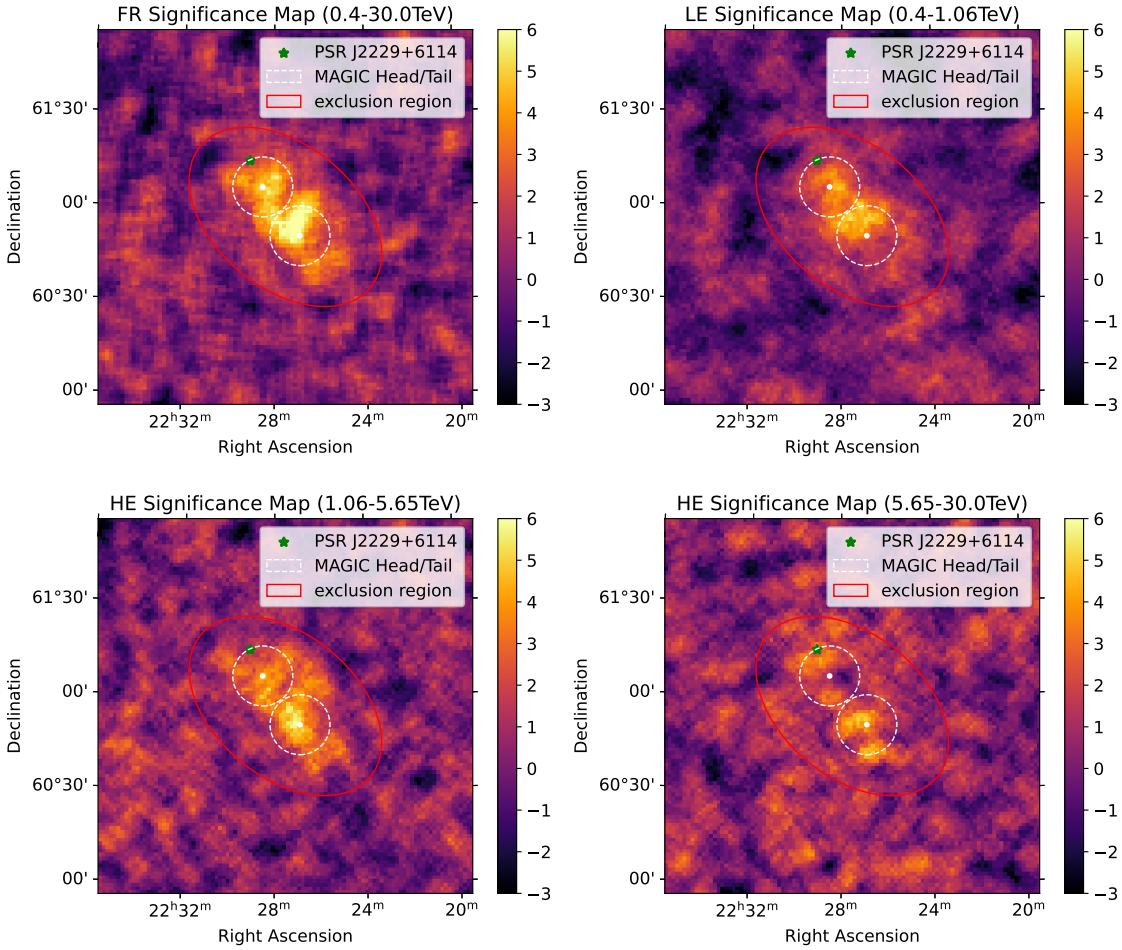

Figure 5.11: `Gammapy` significance maps of the Boomerang SNR. The four maps are for the energy ranges of 0.4 - 30 TeV (top left), 0.4 - 1.06 TeV (top right), 1.06 - 5.65 TeV (bottom left) and 5.65 - 30 TeV (bottom right). In each panel, the position of the pulsar PSR J2229+6114 is marked with a green star and the elliptical exclusion region used during the analysis is enclosed by a red line covering the extended emission of the remnant. The reference Head and Tail positions and extensions are indicated with a white dot and white dashed line, respectively. The significance of the signal is indicated with a color bar to the right of each panel, ranging from $-3\,\sigma$ to $6\,\sigma$.

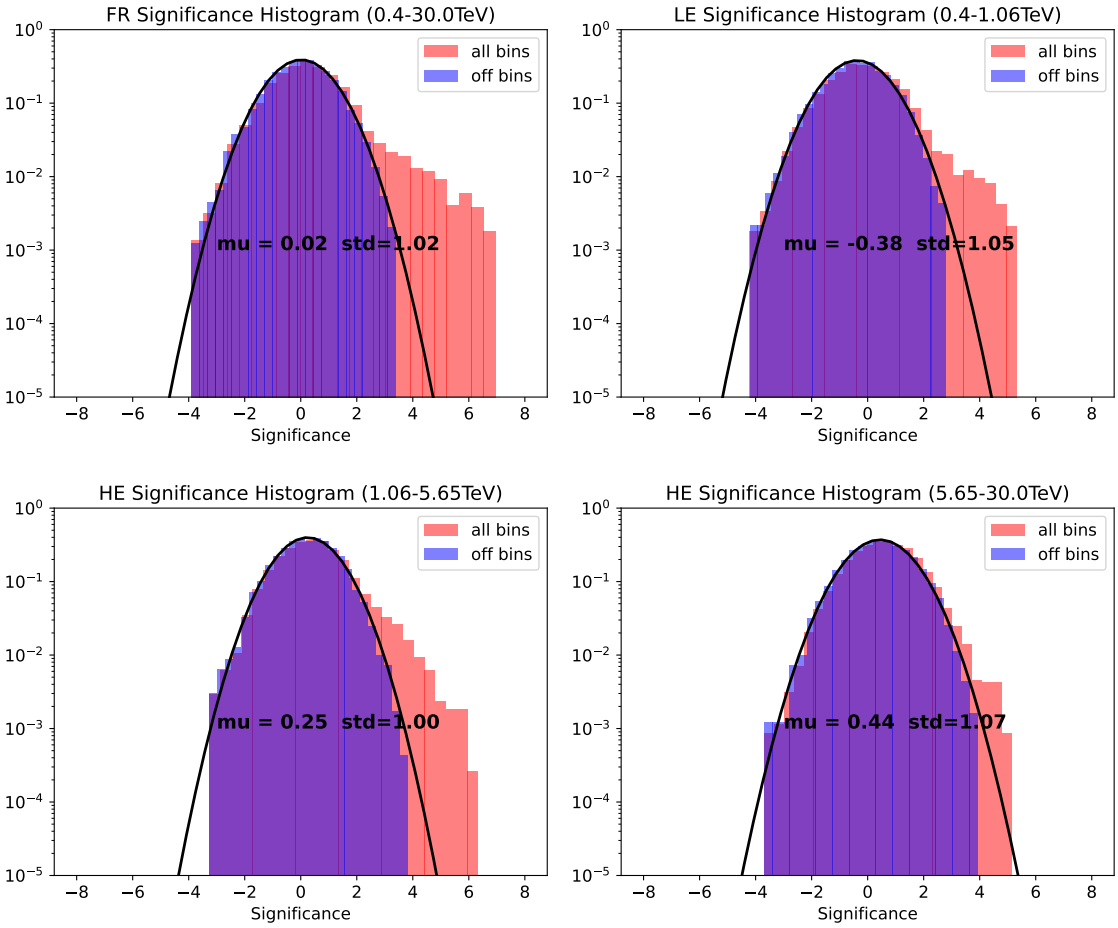

Figure 5.12: Normalized signal and background significance histograms of the Boomerang SNR. The four maps are for the energy ranges of 0.4 - 30 TeV (top left), 0.4 - 1.06 TeV (top right), 1.06 - 5.65 TeV (bottom left) and 5.65 - 30 TeV (bottom right). In each panel, the background distribution of significance values is plotted in blue color (labeled *off bins*) and the total distribution in salmon color (labeled *all bins*). The background is fitted with a Gaussian function (fit indicated with a black line), yielding a mean value μ and a standard deviation σ (printed in black).

5.4.2 Spectral and Spatial Analysis

A simple `PowerLawSpectralModel` (`pl`) with a free amplitude ϕ_0 and a free index Γ was used to spectrally describe each morphological element of the Boomerang SNR. Depending on the number of spatial components of the chosen model, I required one or two spectral models. The spatial component was modeled and fitted in three different ways: Firstly, I tried a single asymmetric `GaussianSpatialModel` (asym. `gauss`). Apart from the coordinates (Ra/Dec) and an extension parameter σ, this model is characterized by an eccentricity e and an orientation angle ϕ. The idea behind this model was to describe the elongated emission of the SNR with a single elliptical shape. Secondly, I applied two symmetric `GaussianSpatialModel`s (and two `PowerLawSpectralModel`s), setting the reference Head and Tail parameters as start values for the simultaneous fit. In the following this approach will be called the *1step* approach. For the last fitting procedure, I performed a fit in two steps, keeping the two spatial and spectral models as well as the start parameter values. Freezing the spectral indices from [76], the spatial models and spectral amplitude were fitted. Then, reversing the situation, the full spectral models were fitted with fixed spatial parameters. I will call this the *2step* approach. The main spectral and spatial results of this work on the Boomerang SNR for the Head and Tail region are presented in a quantitative way in Tab. 5.7 and 5.8 (spectral fit results of the Head and Tail), Tab. 5.10 and 5.11 (spatial fit results of the Head and Tail). Additionally, Tab. 5.9 lists the fitted spectral and spatial parameters for the asymmetric Gaussian model. Results are also visualized in Fig. 5.13 (spectrum of the Head region), 5.14 (spectrum of the Tail region), and 5.15 (fits of various spatial models superposed on a full range significance map).

First, I will concentrate on spectral results obtained when assuming two distinct sources for the spatial description, the Head and the Tail region. In Fig. 5.13 and 5.14, I present the obtained spectral flux of the Head and Tail regions fitted in this work, respectively. The spectral flux is given in units of $\mathrm{cm}^{-2}\,\mathrm{s}^{-1}\,\mathrm{TeV}^{-1}$. Each of the graphs in the top panel shows fitted spectra produced with three different approaches: a 1D spectral fit, a 3D *1step* fit and a 3D *2step* fit. In the Head (Tail) spectrum in Fig. 5.13 (Fig. 5.14) the 1D fit is shown in dark blue (dark red), the 3D *1step* fit is shown in navy blue (red) and the 3D *2step* fit is shown in light blue (salmon). Moreover, the plots contain 3D and 1D flux points/ULs in yellow and orange and a reference spectrum of the reference Head and Tail regions in black, as measured in [76]. The lower panel of Fig. 5.13 and 5.14 plots the residuals of the 3D *1step* approach and the 1D spectrum, computed as the difference between the obtained model and the reference model from [76], divided by the obtained flux errors.

For the Head spectrum, it makes almost no difference whether a 3D model is fitted in *1step* or *2step*s. The resulting amplitudes ϕ_0 and spectral indices Γ in Tab. 5.7 are consistent with each other inside uncertainties and error bands in Fig. 5.13 largely overlap. The 1D spectral fit performed with `gammapy` is in agreement with the 1D analysis of MAGIC, whose spectral parameters are reprinted from [76] in the last row of Tab. 5.7

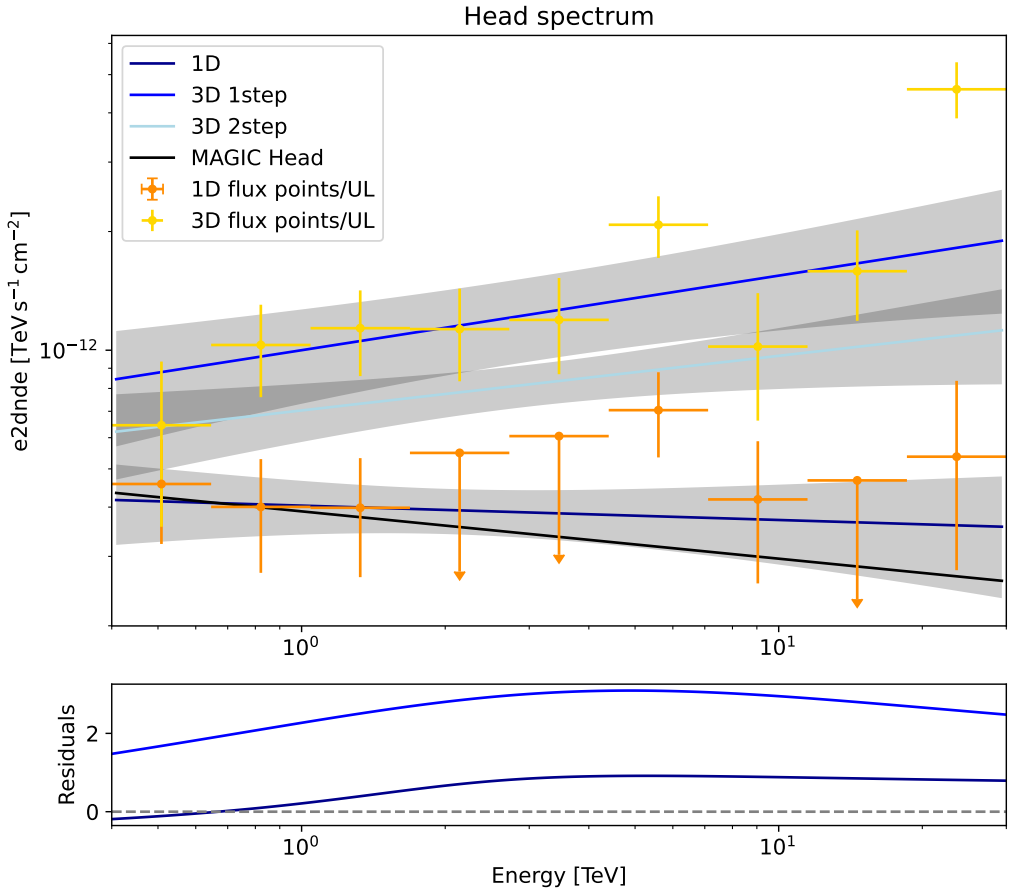

Figure 5.13: `PowerLawSpectrum` of the Boomerang Head region from 3D and 1D analyses (in shades of blue), together with 3D and 1D flux points/ULs (yellow and orange) and the reference spectrum from the MAGIC publication [76] (black). The spectral flux on the y-axis is given in units of $\mathrm{cm}^{-2}\,\mathrm{s}^{-1}\,\mathrm{TeV}^{-1}$. Shown are the fitted spectra of the 1D method in dark blue, the 3D *1step* fit in navy blue and the 3D *2step* fit in light blue. Data has been considered in the energy range 0.4 - 30 TeV for each fit and error bands are drawn in gray around the optimized model curve. The bottom panel displays the residuals of the 3D *1step* and 1D fits, calculated as the difference between the obtained model and the reference model, divided by the obtained flux errors.

for convenience. The 3D and 1D flux points/ULs in Fig. 5.13 are roughly consistent with the power laws from the respective 3D and 1D analyses, which is sufficiently accurate recalling the fact that they are produced with a very approximative approach. There is a slight difference between the Head spectral index Γ of the 1D and 3D approaches, judging from the plot and the spectral values. The Head's spectrum results to be slightly harder with the 3D analysis. This seems to hint at stronger TeV emission from the Head than was found in [76]. It is in this sense consistent with the small hint of emission between 5.65 TeV and 30 TeV found in the sky maps of this work (see bottom right

panel of Fig. 5.4 and 5.11). The previous MAGIC result has a softer spectral index for the Head region, see last row of Tab. 5.7 [76]. However, acknowledging the statistical uncertainties in Tab. 5.7 and the systematic uncertainties stated in section 4.3.4, it is not enough to claim any significant discrepancy, but all spectral indices of this work are found to be consistent with the previous study of MAGIC.

	Φ_{spec}	ϕ_0 [$\text{cm}^{-2}\,\text{s}^{-1}\,\text{TeV}^{-1}$]	Γ
3D (*1step*)	`pl`	$(1.4 \pm 0.3) \times 10^{-13}$	1.81 ± 0.11
3D (*2step*)	`pl`	$(0.9 \pm 0.1) \times 10^{-13}$	1.86 ± 0.11
1D	`pl`	$(4.3 \pm 0.6) \times 10^{-14}$	2.04 ± 0.12
1D [76]	`pl`	$(3.8 \pm 0.14) \times 10^{-14}$	2.12 ± 0.27

Table 5.7: Spectral fit results for the Boomerang SNR Head region, obtained with a 3D double symmetric Gaussian (2 sym. `gauss`) with *1step* and *2step* fitting and a 1D spectral modeling. The table states the type of spectral model Φ_{spec}, the amplitude ϕ_0 and the spectral index Γ of a `PowerLawSpectralModel` (`pl`). In the last row, published values of the Boomerang SNR power law spectrum from [76] are cited. All spectral models are given at a reference energy of $E_0 = 3.0\,\text{TeV}$.

Similar conclusions as for the Head spectrum can be drawn for the Tail spectrum. The two fitted 3D models (*1step* and *2step*) are in very good agreement with each other. Fig. 5.14 shows that their error bands are overlapping and the spectral parameters in Tab. 5.8 are consistent among themselves. The same goes for the 1D spectrum of this work and the 1D spectrum of the MAGIC publication [76]. 3D and 1D flux points/ULs are consistent with the respective model from which they were extracted. The residuals in the bottom panel of Fig. 5.14 show that the 3D *1step* and 1D analysis of this work are both compatible with the reference model from [76]. The spectra and the fitted values are indicating a good agreement between the purely spectral analyses with `MARS` and `gammapy`. Note that in comparison to the Head region, the indices of the Tail region do not have any difference for 3D and 1D analyses but are fully compatible with each other in Tab. 5.8.

Spectral results of both the Head and Tail (this work) exhibit a difference in amplitude related to whether the analysis was based on a 1D or 3D approach. This can be noted both visually in Fig. 5.13 and 5.14 and in numbers in Tab. 5.7 and 5.8. Amplitudes are different by a factor of ~ 3 and ~ 2 for the case of the Head and Tail, respectively. This difference cannot be considered a significant inconsistency, because the ways in which spectra are extracted in a 1D and 3D analysis are intrinsically distinct. In the 1D spectrum, the extraction region is chosen selecting certain events based on a θ^2-cut, while in the 3D fit all events inside the FoV contribute more or less to the spectrum, but their impact is determined by weighting the events with the considered spatial model. It means that we do not expect the spectrum from the 3D analysis to have exactly the same parameters as from the 1D analysis, because we are extracting another spectrum.

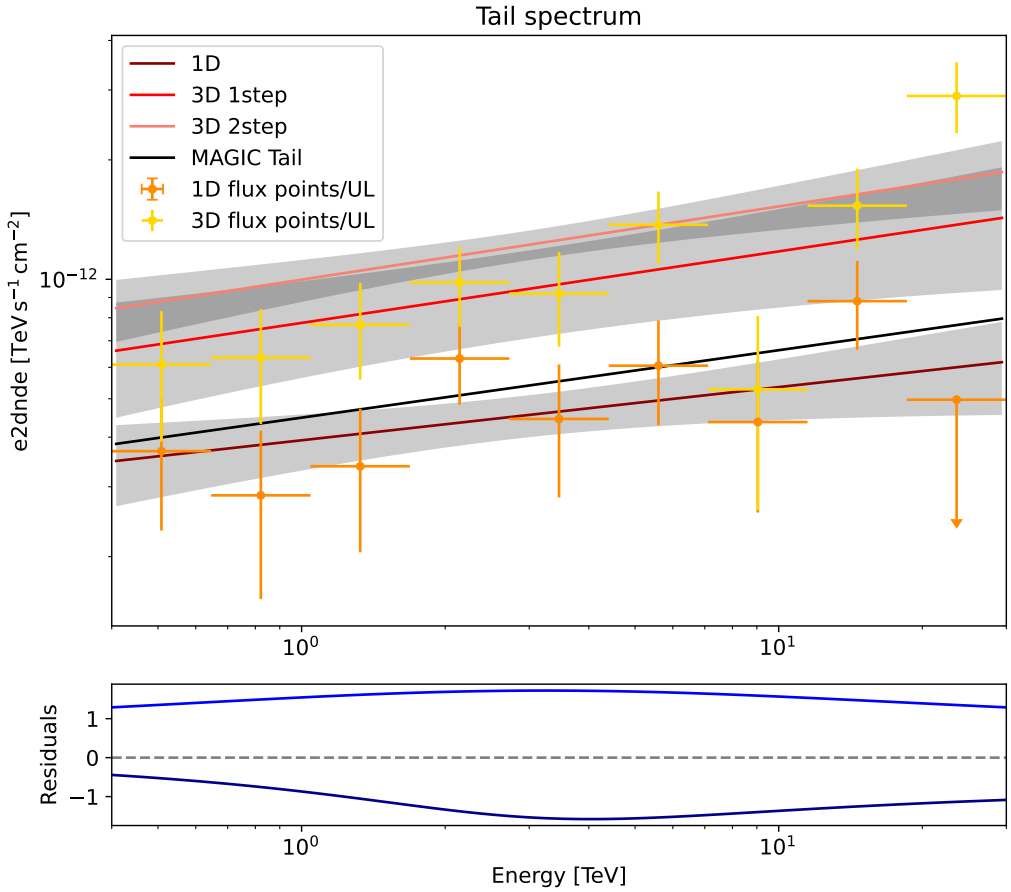

Figure 5.14: `PowerLawSpectrum` of the Boomerang Tail region from 3D and 1D analyses (in shades of red), together with 3D and 1D flux points/ULs (yellow and orange) and the reference spectrum from the MAGIC publication [76] (black). The spectral flux on the y-axis is given in units of $\mathrm{cm}^{-2}\,\mathrm{s}^{-1}\,\mathrm{TeV}^{-1}$. Shown are the fitted spectra of the 1D method in dark red, the 3D *1step* fit in red and the 3D *2step* fit in salmon. Data has been considered in the energy range 0.4 - 30 TeV for each fit and error bands are drawn in gray around the optimized model curve. The bottom panel displays the residuals of the 3D *1step* and 1D fits, calculated as the difference between the obtained model and the reference model, divided by the obtained flux errors.

One more model was tried for the Boomerang SNR, which has a single asymmetric Gaussian spatial component and a power law spectral component. The spectral fit values of the `PowerLaw` are reported in the top row of Tab. 5.9. They should not be directly compared to the values of the double symmetric Gaussian models. However, they seem to be consistent in the sense that the amplitude ϕ_0 is about twice the amplitude of either the Head or Tail region from the other fits. Since the elliptical region of the asymmetric Gaussian model approximately covers the two circular regions of the double symmetric Gaussian model (see Fig. 5.15), this is expected. A similar explanation holds for the

	Φ_{spec}	ϕ_0 [$\text{cm}^{-2}\,\text{s}^{-1}\,\text{TeV}^{-1}$]	Γ
3D (*1step*)	`pl`	$(1.1 \pm 0.3) \times 10^{-13}$	1.82 ± 0.10
3D (*2step*)	`pl`	$(1.4 \pm 0.1) \times 10^{-13}$	1.82 ± 0.08
1D	`pl`	$(5.1 \pm 0.6) \times 10^{-14}$	1.87 ± 0.10
1D [76]	`pl`	$(6.0 \pm 1.7) \times 10^{-14}$	1.83 ± 0.25

Table 5.8: Spectral fit results for the Boomerang SNR Tail region, obtained with a 3D double symmetric Gaussian (2 sym. `gauss`) with *1step* and *2step* fitting and a 1D spectral modeling. The table states the type of spectral model Φ_{spec}, the amplitude ϕ_0 and the spectral index Γ of a `PowerLawSpectralModel` (`pl`). In the last row, published values of the Boomerang SNR power law spectrum from [76] are cited. All spectral models are given at a reference energy of $E_0 = 3.0\,\text{TeV}$.

	Φ_{spec}	ϕ_0 [$\text{cm}^{-2}\,\text{s}^{-1}\,\text{TeV}^{-1}$]	Γ
3D	`pl`	$(2.5 \pm 0.2) \times 10^{-13}$	1.84 ± 0.05

	Φ_{spat}	Ra [°]	Dec [°]	σ [°]	e	ϕ [°]
3D	asym. `gauss`	336.89 ± 0.04	60.95 ± 0.02	0.29 ± 0.03	0.84 ± 0.04	35 ± 6

Table 5.9: Spectral and spatial fit results for the Boomerang SNR, obtained with a 3D asymmetric Gaussian (asym. `gauss`) modeling and a power law spectrum (`pl`). Top: The table states the type of spectral model Φ_{spec}, the amplitude ϕ_0 and the spectral index Γ. The spectral model is given at a reference energy of $E_0 = 3.0\,\text{TeV}$. Bottom: The type of spatial model Φ_{spat}, the fitted coordinate positions Ra/Dec, the width of the major axis σ, the eccentricity e and the orientation angle ϕ are listed.

expectation of the spectral index Γ. It is comparable to the indices from the Head and Tail model (this work), as it roughly combines the two extraction regions.

Next, I present and discuss the spatial results of the 3D analysis carried out on the Boomerang SNR. The best-fit parameters can be found in Tab. 5.10 and 5.11. Additionally, the $1\,\sigma$ contours of the corresponding fitted models are superposed on sky maps in Fig. 5.15 for the asymmetric Gaussian and the two double symmetric Gaussian models. The significance map is the same in all three cases and spans the fitted energy range of the spectral models: 0.4 TeV to 30 TeV. The last row in Tab. 5.10 and 5.11 states the values of the reference Head and Tail positions and extensions from [76]. Note, that these values are listed in the same tables for the purpose of convenient comparison, but are not resulting from a simultaneous fit as the remaining entries. The two coordinate positions of [76] are the results of two separate 2D Gaussian fits, each fit not accounting for the overlapping contribution of the respective other source. In addition, the stated extensions are not the result of a fit but were chosen to have the same fixed radius of $0.16\,^\circ$ to avoid overlap between the reference Head and Tail regions. Though, they are similar to the extensions fitted by the previous analyzers.

	Φ_{spat}	Ra [°]	Dec [°]	σ [°]
3D (*1step*)	sym. `gauss`	337.15 ± 0.08	61.12 ± 0.05	0.19 ± 0.03
3D (*2step*)	sym. `gauss`	337.15 ± 0.07	61.15 ± 0.05	0.15 ± 0.02
`Caspar` [76]	-	337.13	61.10	0.16

Table 5.10: Spatial fit results for the Boomerang SNR Head region. Listed are the results for a 3D double symmetric Gaussian (2 sym. `gauss`) with *1step* and *2step* fitting. The table states the type of spatial model Φ_{spat} with corresponding parameters: the coordinates Ra/Dec and the Gaussian width σ. In the last row, reference values of the Boomerang SNR spatial study from [76] are given. They do not have the same meaning as the fitted parameters of this work, since they were obtained in a different way, as explained in the text.

	Φ_{spat}	Ra [°]	Dec [°]	σ [°]
3D (*1step*)	sym. `gauss`	336.71 ± 0.05	60.83 ± 0.03	0.14 ± 0.02
3D (*2step*)	sym. `gauss`	336.75 ± 0.05	60.84 ± 0.03	0.15 ± 0.03
`Caspar` [76]	-	336.72	60.84	0.16

Table 5.11: Spatial fit results for the Boomerang SNR Tail region. Listed are the results for a 3D double symmetric Gaussian (2 sym. `gauss`) with *1step* and *2step* fitting. The table states the type of spatial model Φ_{spat} with corresponding parameters: the coordinates Ra/Dec and the Gaussian width σ. In the last row, reference values of the Boomerang SNR spatial study from [76] are given. They do not have the same meaning as the fitted parameters of this work, since they were obtained in a different way, as explained in the text.

Best-fit parameters of the asymmetric Gaussian model in the lower panel of Tab. 5.9 and their visualization in the top panel of Fig. 5.15 are consistent with the sky maps of the source based on a visual approach. In 2009, VERITAS first reported about the detection of the Boomerang SNR and the morphology they found, an asymmetric Gaussian [5], whose $1\,\sigma$ contour is also superposed in the top panel of Fig. 5.15. The asymmetric Gaussians are somewhat different in size and orientation. Considering that the structure of the observed emission seen by MAGIC and VERITAS is after all quite different (compare sky maps in Fig. 5.11 with [5]) and much more complex than a simple asymmetric Gaussian, these fits cannot be considered contradictory. It is rather the observed emission region that will need to be clarified in the future. The results from the two double symmetric Gaussian fits (*1step* and *2step*) are fully compatible with each other in terms of position and extension σ in Fig. 5.15. Fitted coordinate positions of the Head and Tail agree between themselves inside the uncertainties and furthermore agree with the fitted positions of [76] in the last row of the Tab. 5.10 and 5.11 and in the bottom panels of Fig. 5.15. As can be seen in the same plot, the $1\,\sigma$ contours coincide with the $0.16\,^\circ$ reference Head and Tail extensions, drawn in white dashed circles. It should be kept in mind that the extensions of [76] have a different

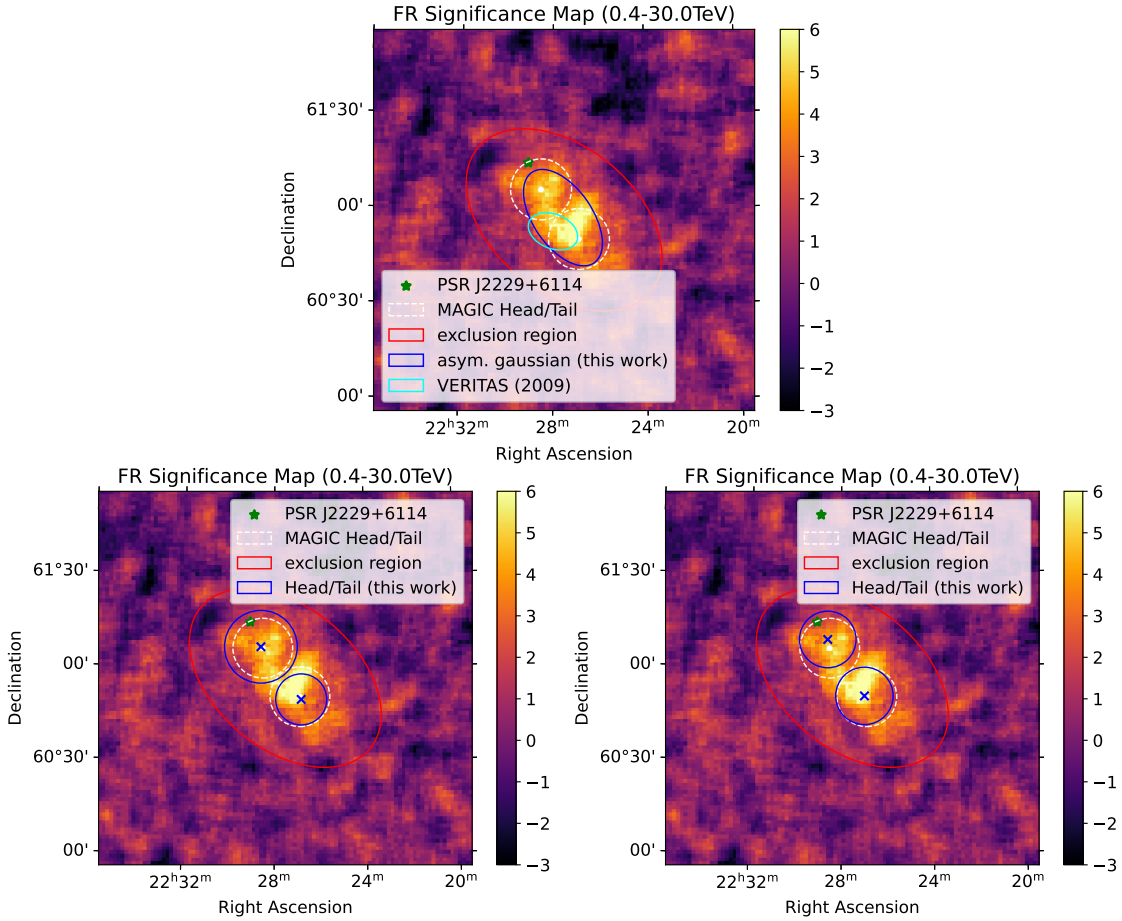

Figure 5.15: Superposition of spatial component fits on significance map of the Boomerang SNR for energies between 0.4 TeV and 30 TeV. The top panel is for the asymmetric Gaussian fit; the bottom panels for the double symmetric Gaussian fits. In the bottom, the left panel is for the 3D *1step* approach, while the right panel is for the 3D *2step* approach. In each panel, the exclusion region used in the analysis is drawn in red, the Boomerang pulsar PSR J2229+6114 is marked with a green star and the reference Head and Tail regions as defined in [76] are enclosed in white dashed circles. The $1\,\sigma$ contours of the fitted regions are superposed in blue while their centroids are marked with blue crosses in each panel. The top panel also contains the $1\,\sigma$ contour of the emission region reported by the VERITAS collaboration [5].

meaning than a Gaussian width parameter, which limits comparability.

A model quality assessment was performed, equivalent to the one presented for the Crab Nebula. Here, I only confront two distinct models: the asymmetric Gaussian model (asym. `gauss`) and the double symmetric Gaussian model (2 sym. `gauss`) fitted in

1step. The maximized likelihood values, as returned by the fit, the number of *dof* and the AICs computed with Eq. 4.11 are listed in Tab. 5.12. According to these values, the asymmetric Gaussian model is preferred over the double symmetric Gaussian model, although this preference is only slight. With Eq. 4.12, it was found that the double symmetric Gaussian model is around 0.12 times as probable as the asymmetric Gaussian model. Statistically speaking, the significance of that probability is only around $2\,\sigma$ (from Eq. 4.13). It follows that the two tested models perform equally well on the given data.

Φ_{spat}	Φ_{spec}	$-2 \times \log(\hat{L})$	*dof*	*AIC*
asym. `gauss`	`pl`	-255373.65	7	-255359.65
2 sym. `gauss`	2 `pl`	-255375.50	10	-255355.50

Table 5.12: AIC for two spatial models of the Boomerang SNR: the asymmetric Gaussian model (asym. `gauss`) and the double symmetric Gaussian model (2 sym. `gauss`) from *1step* fitting. AIC values are computed from the maximized log-likelihood values $\log(\hat{L})$ and the number of *dof* of the total fitted model, including spatial and spectral components. For the spectral components of both models a `PowerLawSpectrum` (`pl`) was used.

Summing up, the morphological results obtained for the Boomerang SNR in this thesis with a 3D analysis are largely confirming results of a previous 1D analysis with the same dataset from the MAGIC telescopes [76]. The spectral and spatial models tested for the Boomerang SNR agree very well with themselves and previous measurements. The spatial distribution of the emission can be described with an asymmetric Gaussian model or with a double symmetric Gaussian model. The Tail region exhibits a γ-ray signal above 6 TeV, which is in agreement with MAGIC results and many other articles. The question whether this emission is related to hadronic particles colliding with a molecular cloud or some other scenario cannot be answered by the kind of study performed in this work, but may be clarified in future works profiting from works like this. It remains to be determined if the Head region features some significant γ-ray emission or not, which will mostly depend on ongoing and upcoming efforts in characterizing the background properties and finding ways to understand and reduce systematic influences. This leads me to the last section of this chapter, which will discuss the background estimation of the presented analysis.

5.5 Discussion of the Background Estimation

Without doubt, the background is the most dominant source of uncertainty in this work. Above, I have presented that my 3D analysis pipeline is subject to several systematic effects, which we do not yet understand and which require dedicated studies in the next years. In section 4.2, I introduced the types and dependencies of the background and I will discuss its actual influence on the presented analysis here. The statements will be valid both for the Crab Nebula and the Boomerang SNR sample, if not stated otherwise, using the dataset specifications from section 5.1.

To respond to the influence of changing performance of the telescope hardware, MC periods defining distinct intervals of constant telescope performance were introduced. Since the background is expected to change with the period in general, a background model for each period was derived separately in this work (see section 5.2). The MAGIC telescope system is another influential factor for the background, explained through its geometry. Judging from Fig. 4.4, the projected inter-telescope distance $d_{\text{projected}}$ (defined in Eq. 4.1) for the Boomerang SNR data sample lies between 60 m and 83 m and the rotation angle γ between $-70\,^\circ$ and $20\,^\circ$. From the first, it follows that the azimuth angle dependency of the shape of the background is relatively limited in my dataset; from the second, I expect a dipole-shaped background, confirmed by the background maps produced for the Boomerang SNR (see appendix A). For the Crab Nebula data sample, the observations match in terms of zenith but contain a wider range of azimuth angles. From there come the rather circular-shaped backgrounds in the background maps (see appendix A). As mentioned before (see section 5.1), the data sample for this work's analysis has been taken at zenith distances where the shape of the background is not yet disturbed by a strong gradient. Hence, the direct zenith-dependent influence on the background estimation is minimized. Moreover, the data selection for the published analysis that was carried out by the previous analyzer was done with a quality cut of 0.85 for the cumulative transmission at 9 km from the telescopes (measured with the LIDAR, see section 2.3.1). I applied the same transmission cut for the Crab Nebula. Therefore the influence of the atmosphere on the background can be considered as minimal as possible. Since this study is about a Galactic source, located close to the Galactic plane, a small contribution to the background originating from diffuse γ-ray emission in the FoV is present but taken into account when modeling the background. The data used for this study was taken exclusively under dark time conditions.

Apart from these effects to which it was possible to respond appropriately, there are others that could not be reduced in impact. Repeating this kind of study, one might want to try different background estimation techniques and compare their performance to reduce fluctuations in the shape of the background and find the method introducing the least systematic uncertainties. Using the whole dataset between $30\,^\circ$ and $50\,^\circ$ zenith angle and azimuth angles of $0\,^\circ$ to $50\,^\circ$ and $320\,^\circ$ to $360\,^\circ$, I found that some of the MC periods provide limited statistics for a solid background estimation. In Fig. A.5 in appendix A for example, it can be noticed that the available statistics decreases strongly above tens of TeV. The range of energy considered in this work goes from 0.4 TeV to 30 TeV, meaning that the analysis was not too badly affected by missing statistics except for the period ST.03.08 of the Boomerang SNR and ST.03.10 for the Crab Nebula (see background models in appendix A). At high energies, the background rate could have been misreconstructed for the affected periods. Statistics is without doubt a crucial factor to be improved, considering that specifically at multi-TeV energies, my results are still ambiguous about the presence or absence of strong emission. Without more populated background models, this ambiguity between a γ-ray signal and a misreconstructed background will not be resolved. While for the named coordinate ranges and the scope of

this thesis, the approximation of a uniform background is expected to be viable, a more precise approach would include binning in zenith and azimuth angle. Thus, it would further reduce the available statistics in each bin. The choice of binning is a trade-off between the accuracy of the background models applied to the data and the statistics one has to deal with.

Summarizing, the influences on the background estimation of this analysis were reduced where possible, but several remaining effects might cause systematic uncertainties, whose magnitude is at the moment not well known. However, they have been discussed wherever relevant when results were presented.

Chapter 6

Conclusion

This master's thesis is focused on the data analysis of a potential Galactic PeVatron emitter and CR accelerator with archival observations from the MAGIC telescopes, the Boomerang SNR G106.3+2.7.

When analyzing extended sources, the main difficulty to handle is the influence of the background, which is in general non-uniform over the FoV and requires dedicated treatment. With the advent of novel and more appropriate analysis techniques for extended-source analyses in γ-ray astronomy, we can tackle the challenge of background estimation more efficiently. My contribution to this field of science is composed of two parts: the exploration and validation of new methods for the analysis of extended sources, supported by the current movement promoting the adoption of a standardized and open framework, and the advancement of our understanding of a particular PeVatron candidate, the Boomerang SNR. I re-analyzed archival MAGIC data from this source at high-level, starting with the already low-level processed dataset from a previous publication [76]. As a starting point, I re-performed the high-level analysis with `MARS`, introducing a small improvement in the wobble treatment with `caspar`. The resulting signal significances and sky maps are in good agreement with the previous MAGIC results, and display the same energy-dependent morphology. Moving to more appropriate tools for the complex analysis of extended sources, the main part of the project was carried out along three lines of work: the preparation of a 3D and 1D analysis pipeline, its validation on Crab Nebula data and its execution on Boomerang SNR data. I converted the proprietary MAGIC data, at an equivalent level of DL2, to DL3 format and computed full-enclosure IRFs with the `DL3 Converter`. Subsequently, I produced 3D background template models with the software `pybkgmodel`, binned in energy. Finally, I reduced the data and applied 3D and 1D fitting and modeling routines in the framework of `gammapy` to my datasets, trying various spatial models to describe the morphology of the Crab Nebula and the Boomerang SNR.

Testing the 3D analysis pipeline with Crab Nebula data, I could validate the pipeline for usage on other sources. The results for the spectra and sky maps of the Crab Nebula from 3D and 1D analyses were in very good agreement with previous results from the MAGIC collaboration. The test enabled the identification of two systematic effects on the analysis. As a consequence, the asymmetric feature in the background histograms at low energies could be reduced introducing an elevated energy threshold. In addition, I proposed a possible approach to investigate the systematic shift of the mean in the background significance histograms in future studies and found indications that the effect is related to the spectral modeling of the background. Fitted spectra and fit residuals of the 3D models and a model quality test with the AIC all point to the Gaussian spatial model as the more accurate description of the Crab Nebula's emission, compared to a point spatial model. In this way, I was able to provide the most stringent UL on the extension of the Crab Nebula ever measured by the MAGIC telescopes: $\sigma = (0.0239 \pm 0.0008)^\circ$. The measurement is subject to a systematic uncertainty of the pointing of $\lesssim 0.02^\circ$, which justifies, that no unanimous statement about a detection can be made for the moment. The measured extension UL is larger but comparable in magnitude with previous H.E.S.S. and *Fermi*-LAT extension measurements, suggesting that it is on the verge of a detection. Even though the evidence does not suffice to claim extended emission from the Crab Nebula, my result demonstrates the capability of the 3D analysis to extract more precise spatial information from IACT measurements than the typical resolution of around 0.07° would allow.

Applying the 3D analysis pipeline to G106.3+2.7 data, I performed one of the first full spectro-morphological analyses of MAGIC data of an extended source, using standardized data formats and open-source analysis tools. The morphological results obtained for G106.3+2.7 in this thesis are predominantly confirming the findings of the previous publication, except for a new hint of emission from the Head region above 6 TeV. I tested an asymmetric Gaussian model and a double symmetric Gaussian model with a Head and Tail region for the description of the emission in the whole energy range and found both of them to be viable. The spectral results of the 3D double symmetric Gaussian fit indicate a slightly harder index for the Head region than the 1D analysis of this work and the published work, while the indices for the Tail region are all very consistent. Whether the Head region displays significant γ-ray emission above several TeV is left open for the moment.

More constraining evidence might be detectable once ongoing and upcoming efforts in characterizing the background properties are fruitful. On that note, it will be crucial to find ways to understand and reduce systematic influences to better distinguish between a source and a background signal. In the future, other and more complex spatial models might be worth to try describing the emission of the remnant. One of the most important imprecisions of the applied models is the uniformity in energy. Since the Boomerang SNR displays an energy-dependent morphology, energy-dependent spatial models would be more suitable. A tool that offers possibilities for these kind of studies and whose use would be an interesting test to conduct is the recently implemented

`EnergyDependentMorphologyEstimator` of `gammapy`.

Recalling that the 3D analysis technique is a novel approach and comes with unknown systematic uncertainties, it becomes clear that one main effort of the community will concentrate on understanding these effects and developing tools to reduce the influence of the background. In this thesis, I named numerous starting points for further research in that direction. The 3D pipeline I developed could be refined for a more in depth and more precise study of the performance of background models on an extended-source analysis, by binning the data in azimuth and zenith to take into account the related dependence. The results from different background estimation techniques could be confronted in the future. For instance computing background models from OFF data might be beneficial to increase the available statistics for robustness, as well as trying the so-called ring background method, implemented in `gammapy`. As indicated by the results of this thesis, different spectral models for the background might be worth to try, and the definition of new standards including the implementation of asymmetric IRFs will be of advantage. Moreover, an optimization of the hadronness cut can help to solidify results, removing one source of uncertainty. Ultimately, the study could be done using other extended sources to probe its performance with different morphologies and enlarge our understanding of the Galactic source population. Another line of work to be followed is a deeper study of the extension of seemingly point-like sources that could reveal a minor extension below the typical angular resolution limit of IACTs. Although this has not been achieved for the Crab Nebula in this work, the measurement of an UL below the angular resolution limit of the MAGIC telescopes demonstrated the strength of the 3D analysis method.

Concluding, I have demonstrated that the novel 3D analysis technique is developing into a powerful tool for the analysis of γ-ray data in several ways. Using dedicated 3D background models, it enables the analyzer to perform the analysis of complex emission regions with simultaneous spatial and spectral fitting and possibly to detect the extension of nearly point-like sources below the angular resolution limit of an instrument. The next few years may show which other strengths the method can offer and future work along these lines will concentrate on improving these techniques. The ultimate goal is to validate the novel 3D analysis and find out how it can help to solve the question about the origin of CRs. Only then will the γ-ray community be able to clarify, whether G106.3+2.7 is an efficient CR accelerator and which part of its spatial appearance is produced by leptonic or hadronic emission mechanisms.

Appendix A

Additional Graphs

The appendix contains the complete set of background models produced during this analysis, and further graphs from the high-level spectral and spatial analyses (1D and 3D), that do not belong to the main results but should be present for completeness and to underline statements, made in this thesis. Some of them will be referred to in the main text.

Background Models - Crab Nebula

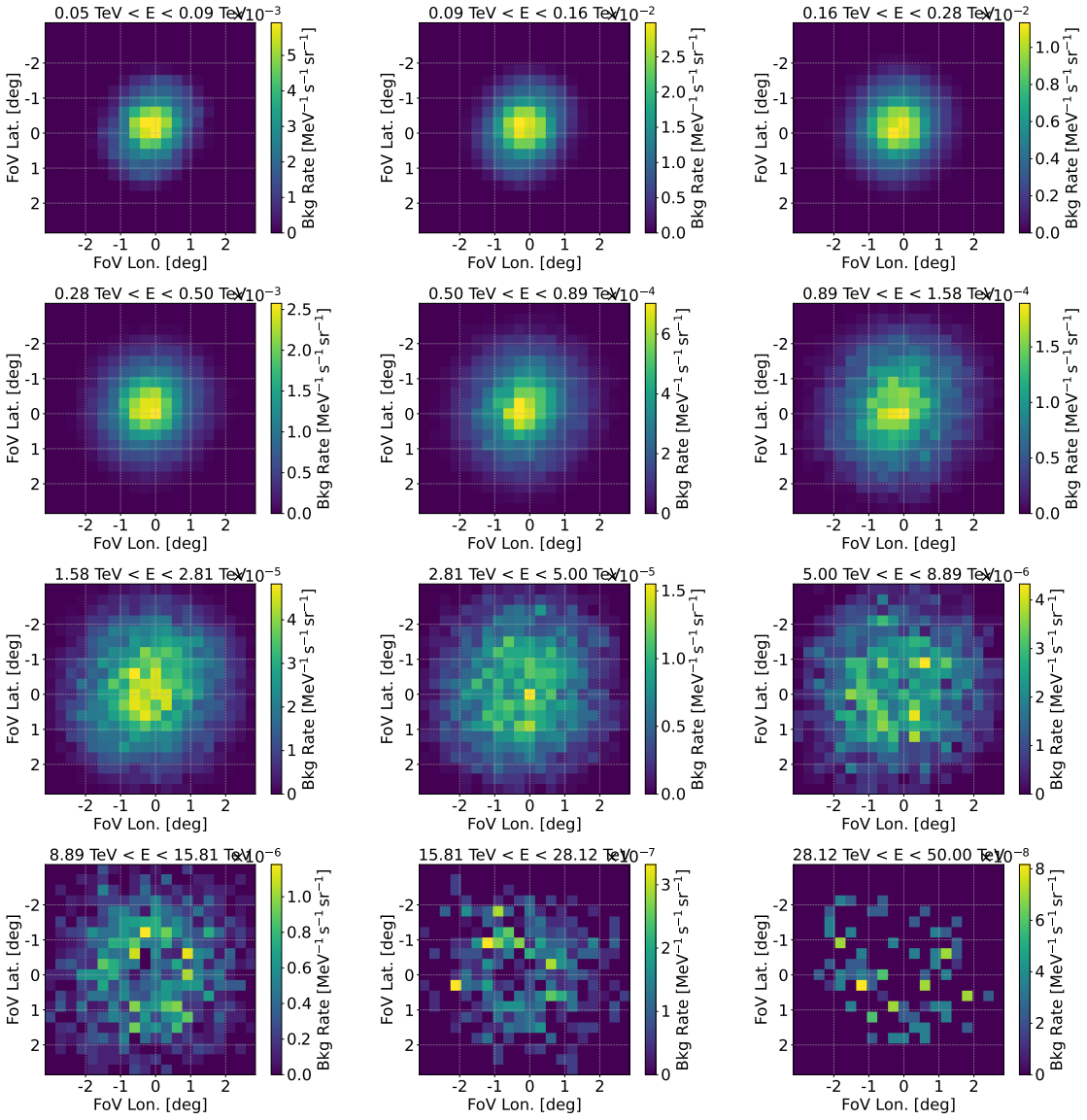

Figure A.1: Background models for period ST0307 of Crab Nebula observations, consisting of 2D histograms of the background rate inside the camera FoV in 12 logarithmic energy bins between 50 GeV and 50 TeV. The background rate is given in units of $\mathrm{MeV}^{-1}\,\mathrm{s}^{-1}\,\mathrm{sr}^{-1}$ and the camera plane in degrees of FoV longitude and latitude.

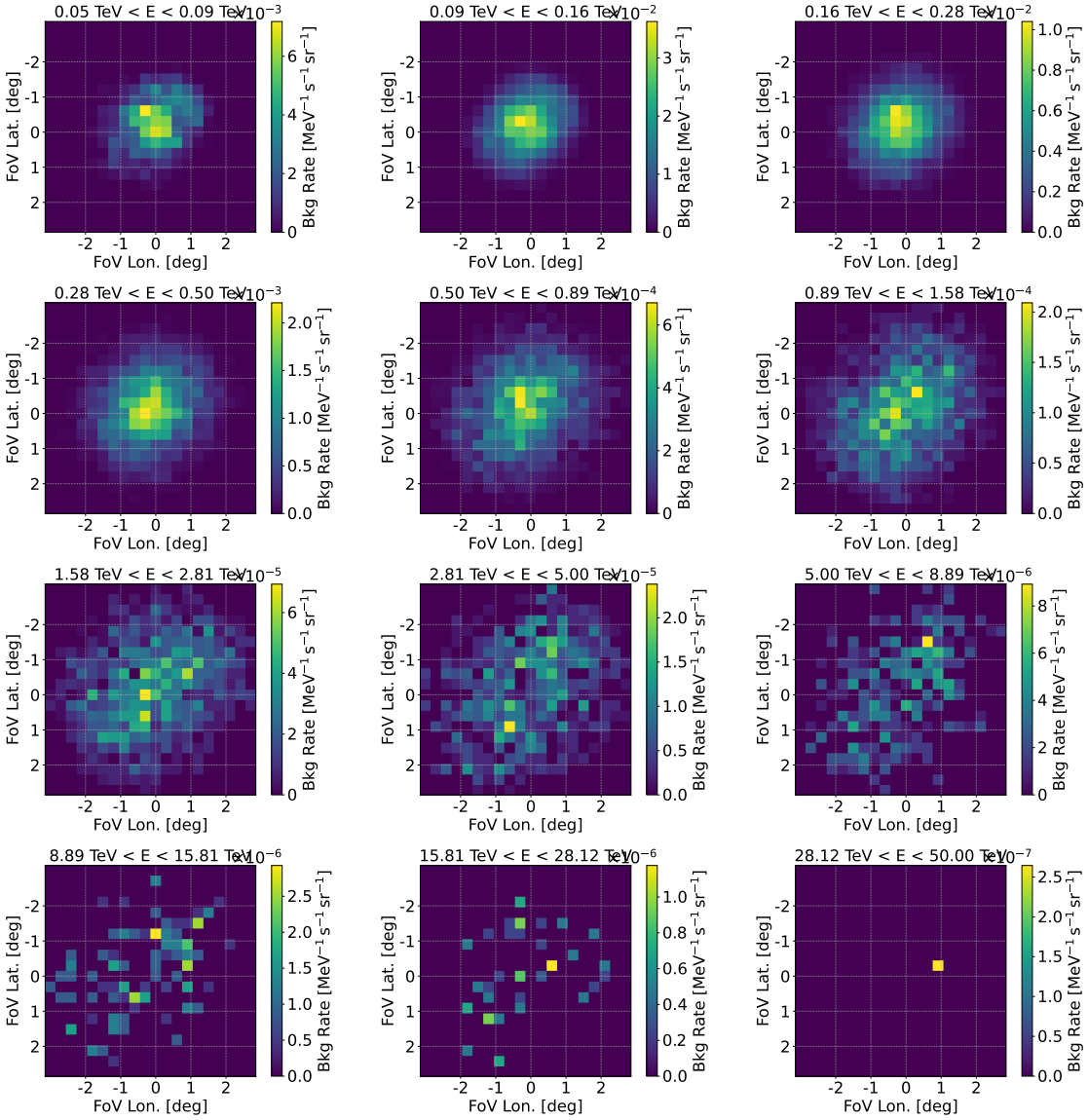

Figure A.2: Background models for period ST0310 of Crab Nebula observations, consisting of 2D histograms of the background rate inside the camera FoV in 12 logarithmic energy bins between 50 GeV and 50 TeV. The background rate is given in units of $\mathrm{MeV}^{-1}\,\mathrm{s}^{-1}\,\mathrm{sr}^{-1}$ and the camera plane in degrees of FoV longitude and latitude. The statistics is low for this period.

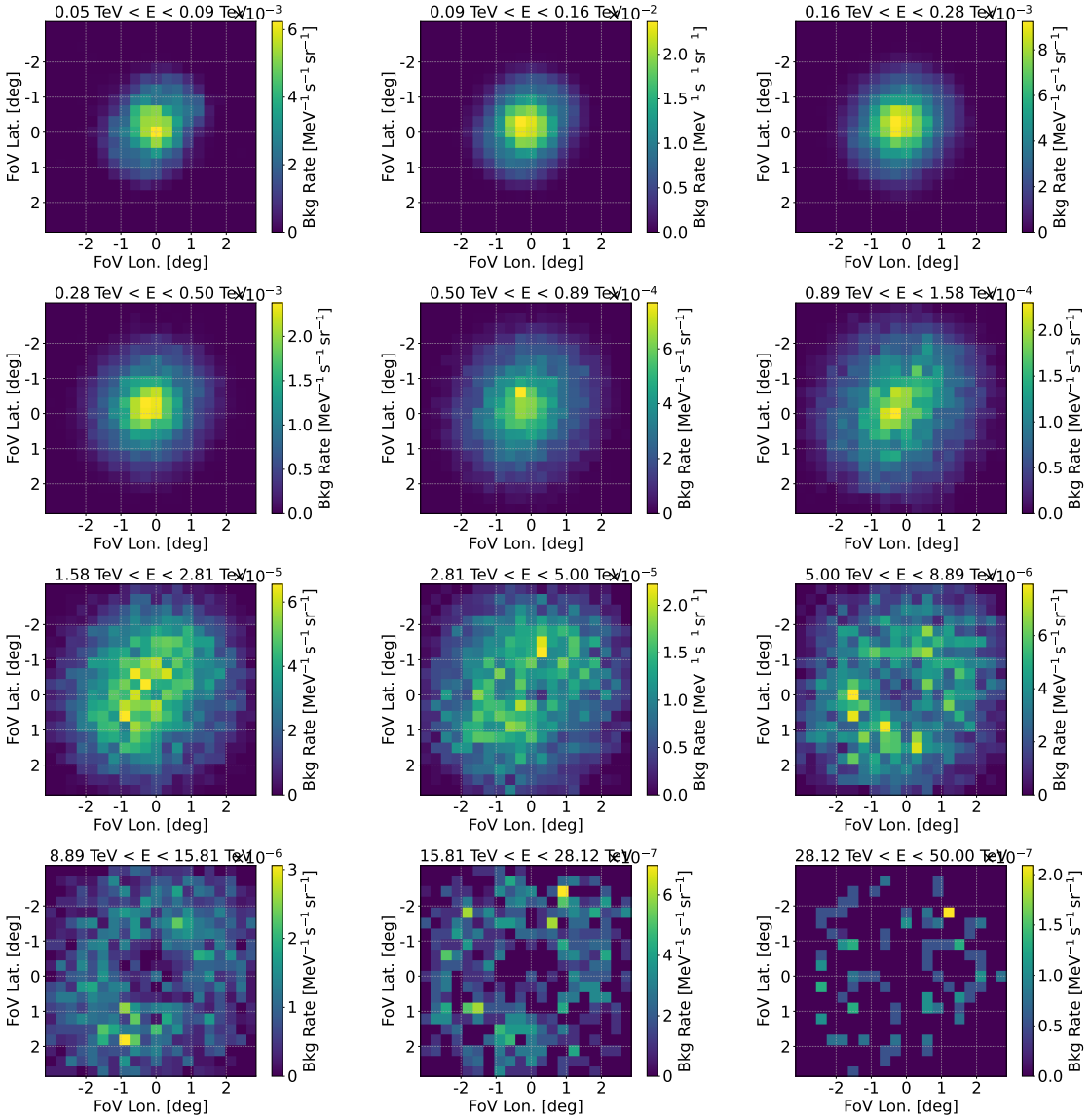

Figure A.3: Background models for period ST0311 of Crab Nebula observations, consisting of 2D histograms of the background rate inside the camera FoV in 12 logarithmic energy bins between 50 GeV and 50 TeV. The background rate is given in units of $\mathrm{MeV}^{-1}\,\mathrm{s}^{-1}\,\mathrm{sr}^{-1}$ and the camera plane in degrees of FoV longitude and latitude.

Background Models - Boomerang SNR

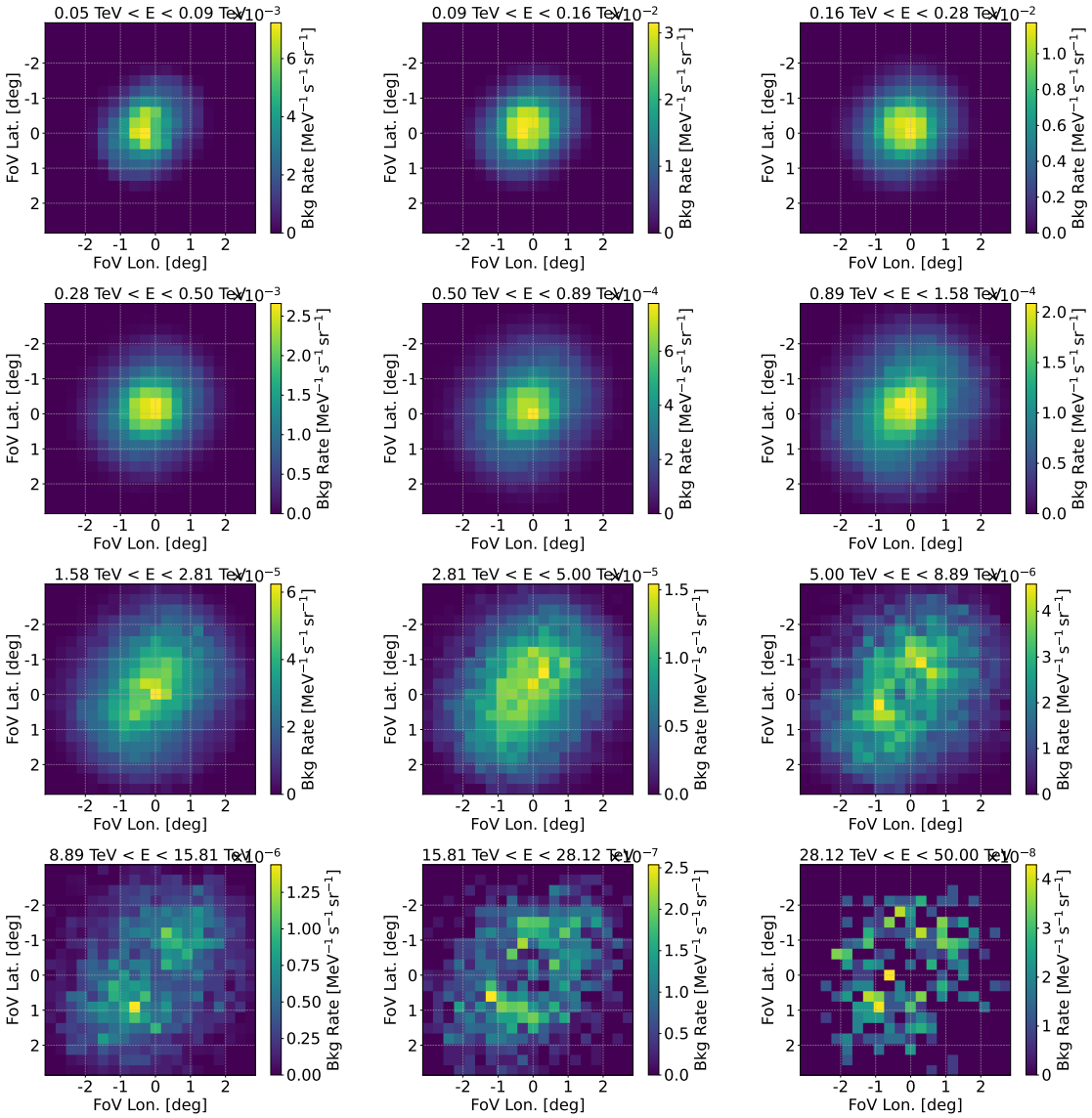

Figure A.4: Background models for period ST0307 of Boomerang SNR observations, consisting of 2D histograms of the background rate inside the camera FoV in 12 logarithmic energy bins between 50 GeV and 50 TeV. The background rate is given in units of $\mathrm{MeV}^{-1}\,\mathrm{s}^{-1}\,\mathrm{sr}^{-1}$ and the camera plane in degrees of FoV longitude and latitude.

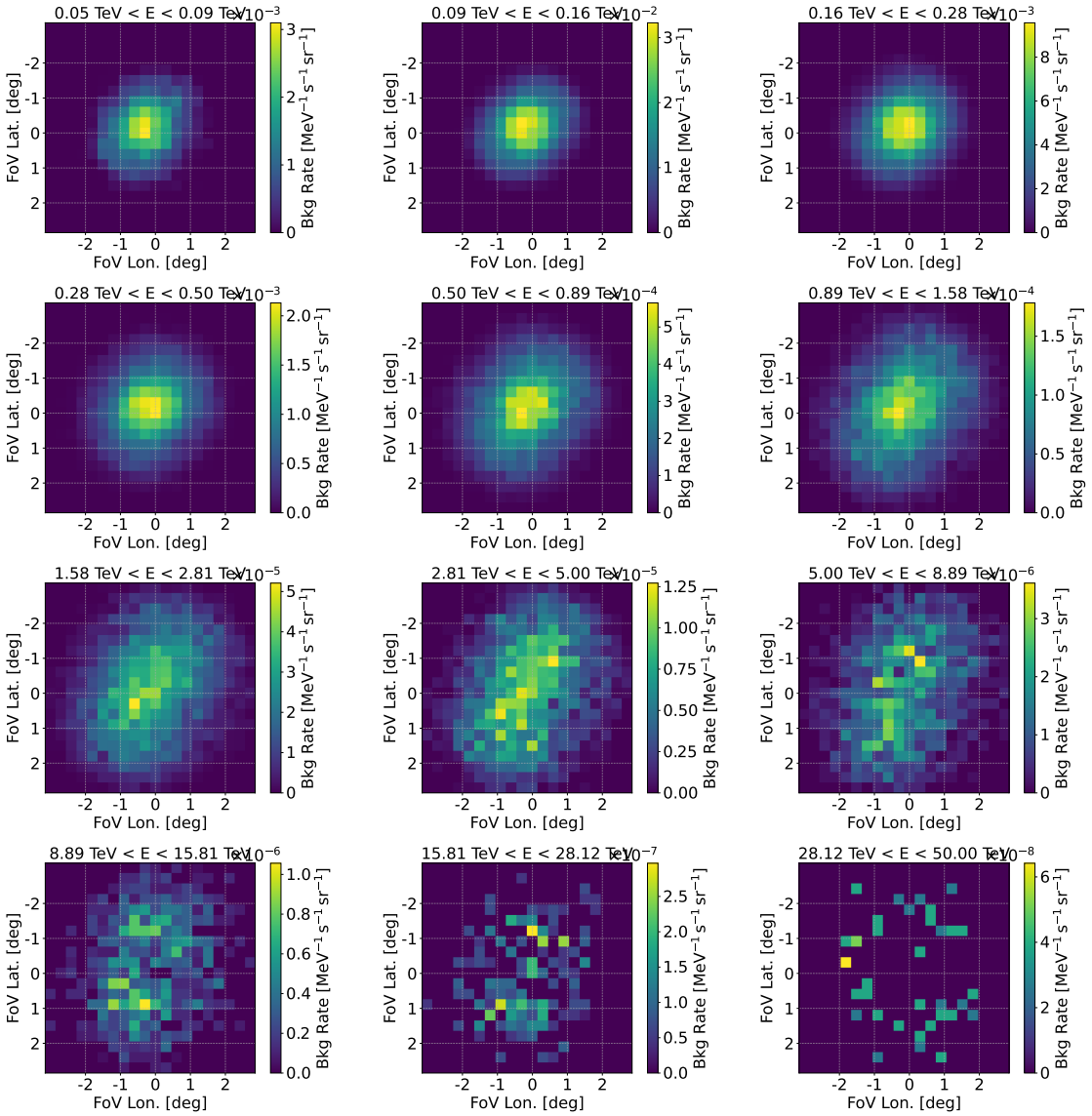

Figure A.5: Background models for period ST0308 of Boomerang SNR observations, consisting of 2D histograms of the background rate inside the camera FoV in 12 logarithmic energy bins between 50 GeV and 50 TeV. The background rate is given in units of $\mathrm{MeV}^{-1}\,\mathrm{s}^{-1}\,\mathrm{sr}^{-1}$ and the camera plane in degrees of FoV longitude and latitude.

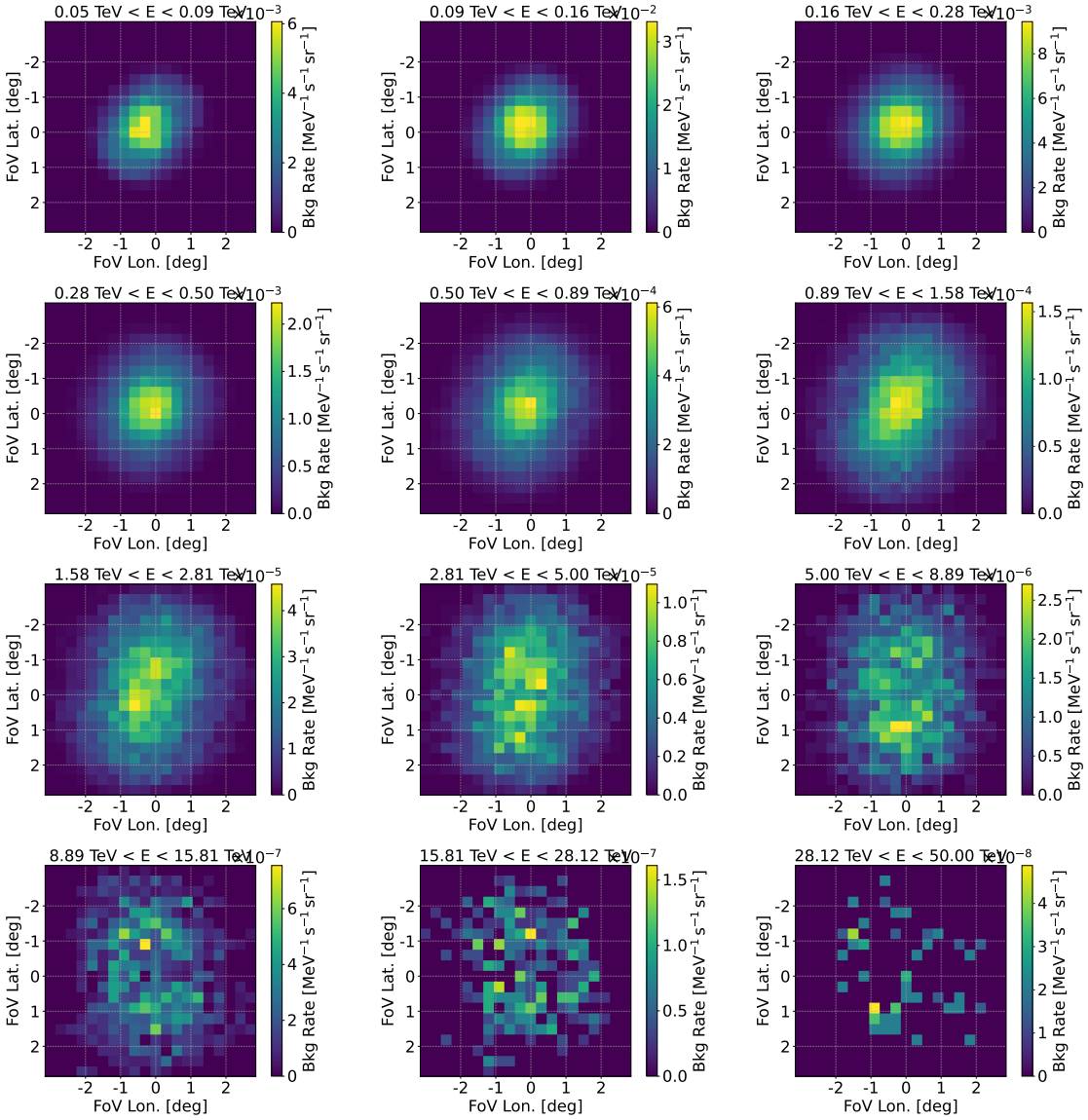

Figure A.6: Background models for period ST0310 of Boomerang SNR observations, consisting of 2D histograms of the background rate inside the camera FoV in 12 logarithmic energy bins between 50 GeV and 50 TeV. The background rate is given in units of MeV^{-1} s^{-1} sr^{-1} and the camera plane in degrees of FoV longitude and latitude.

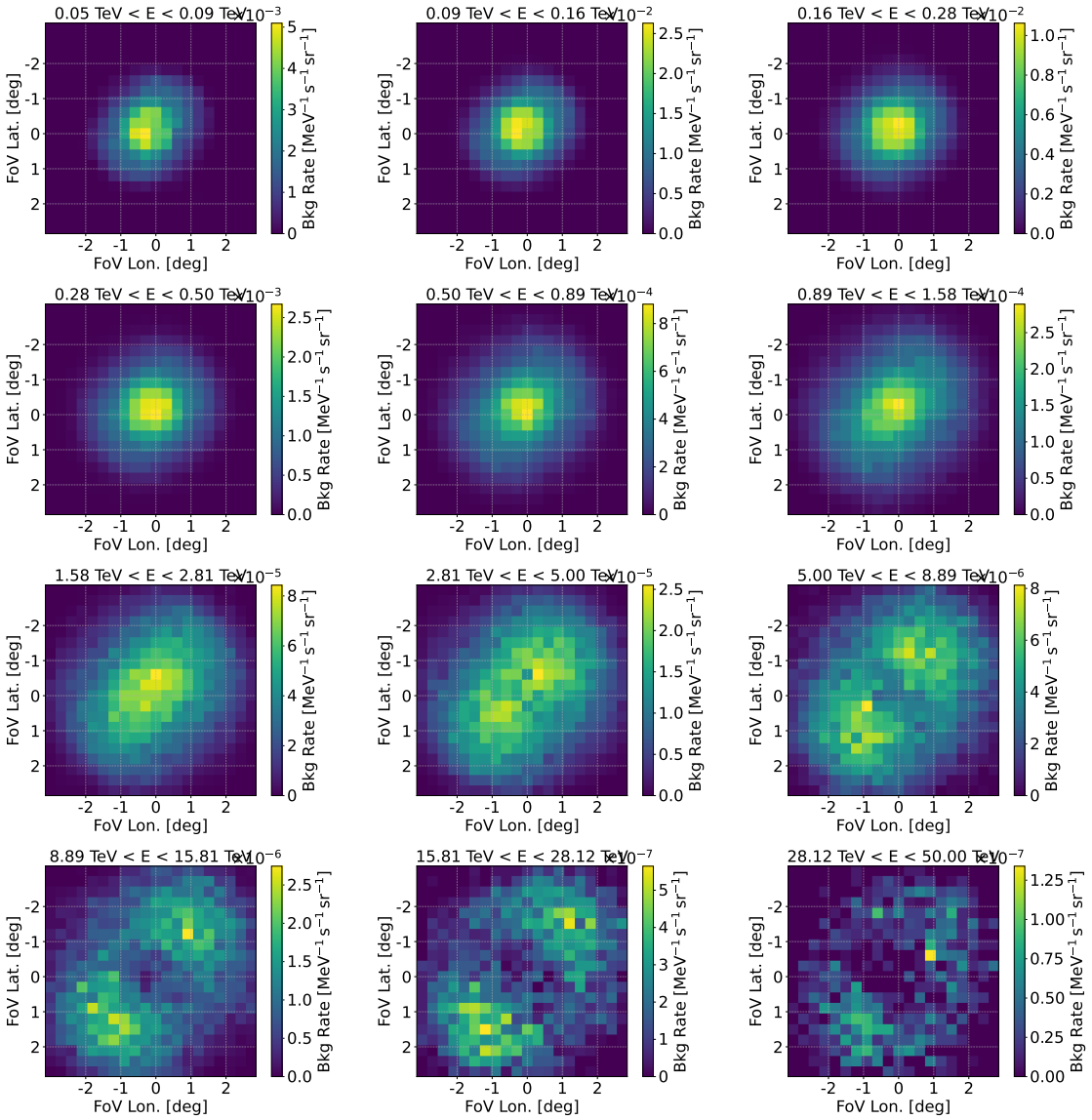

Figure A.7: Background models for period ST0311 of Boomerang SNR observations, consisting of 2D histograms of the background rate inside the camera FoV in 12 logarithmic energy bins between 50 GeV and 50 TeV. The background rate is given in units of $\mathrm{MeV}^{-1}\,\mathrm{s}^{-1}\,\mathrm{sr}^{-1}$ and the camera plane in degrees of FoV longitude and latitude.

1D Spectral Analysis - Crab Nebula

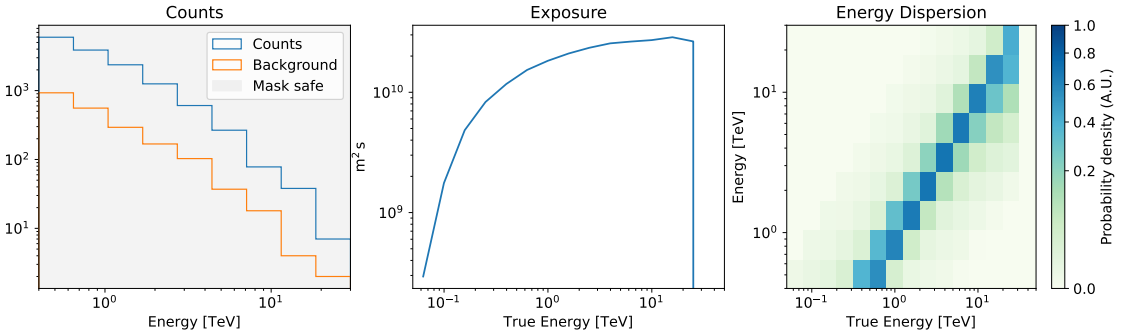

Figure A.8: Counts of the signal and background, exposure and energy dispersion of the stacked 1D Crab Nebula dataset. Counts are plotted against the reconstructed energy, the exposure in terms of the true energy and the energy dispersion is given as a matrix relating true and reconstructed energy.

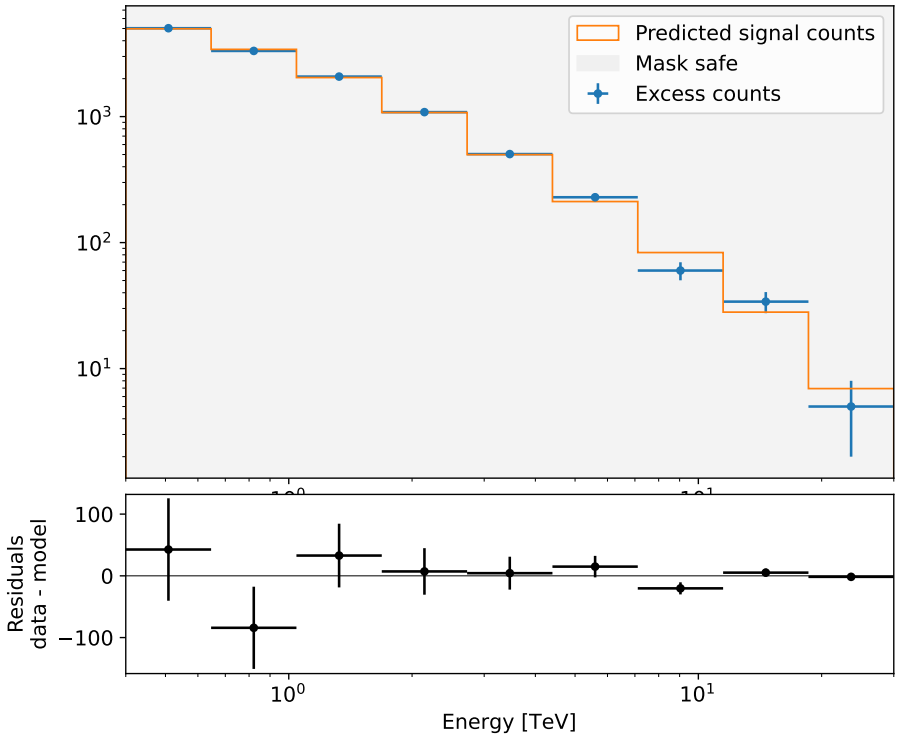

Figure A.9: Measured and predicted signal counts from the 1D analysis of the Crab Nebula against reconstructed energy. Predicted signal counts from the fitted spectral model are rendered in orange, measured counts in blue. The gray region indicates a safe range of the data as defined by the safe mask. The bottom panel displays the difference between the data and the applied model.

1D Spectral Analysis - Boomerang SNR

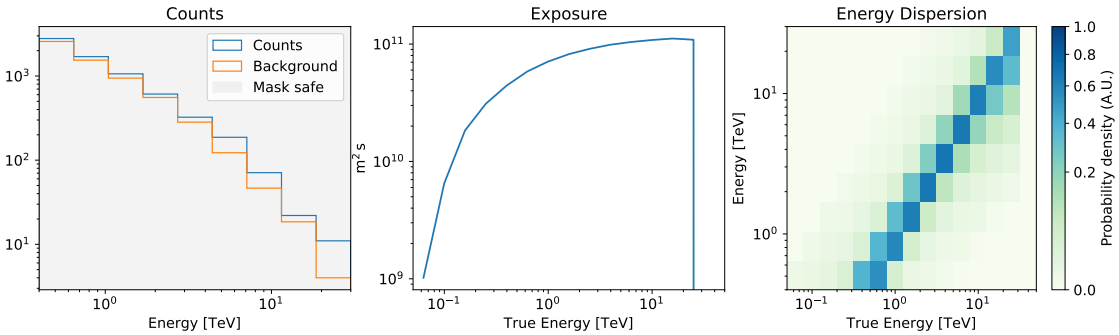

Figure A.10: Counts of the signal and background, exposure and energy dispersion of the stacked 1D Boomerang SNR dataset for the Head region. Counts are plotted against the reconstructed energy, the exposure in terms of the true energy and the energy dispersion is given as a matrix relating true and reconstructed energy.

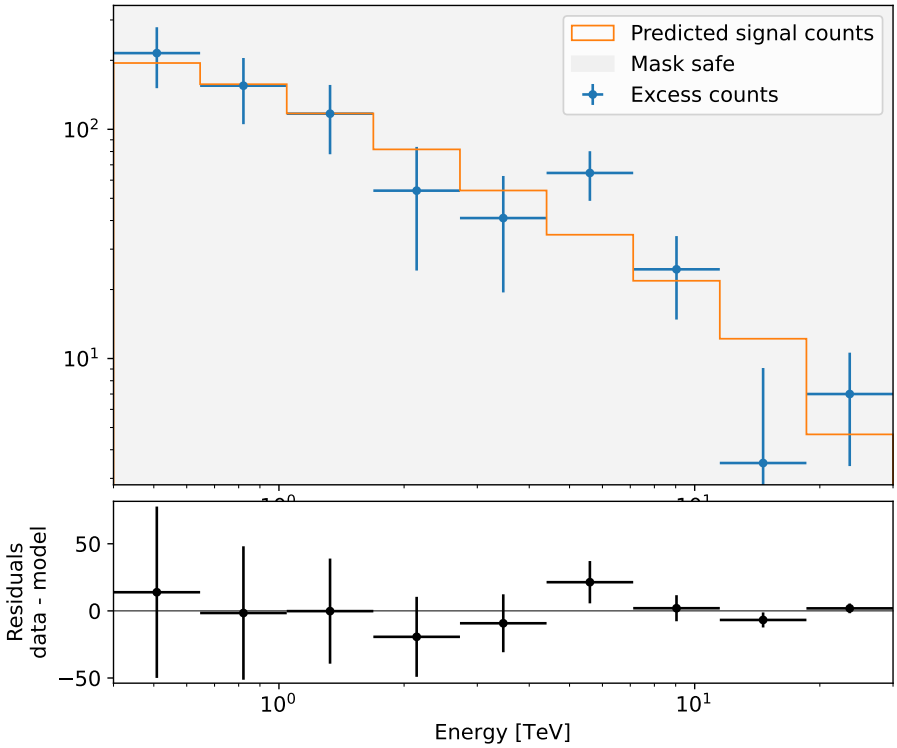

Figure A.11: Measured and predicted signal counts from the 1D analysis of the Boomerang SNR Head against reconstructed energy. Predicted signal counts from the fitted spectral model are rendered in orange, measured counts in blue. The gray region indicates a safe range of the data as defined by the safe mask. The bottom panel displays the difference between the data and the applied model.

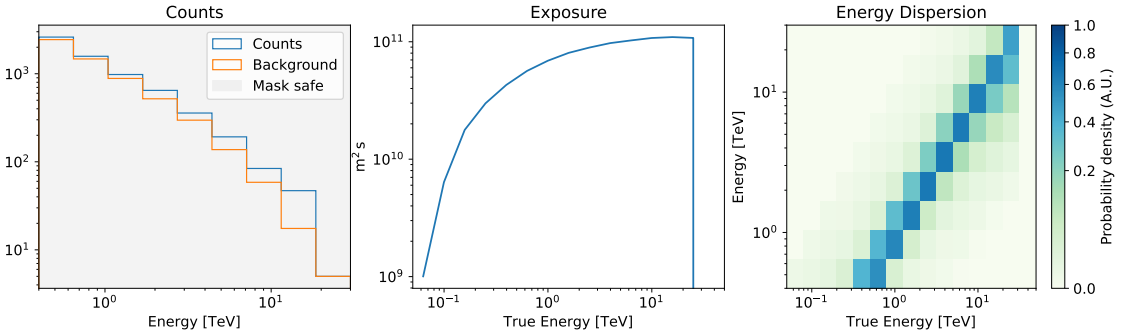

Figure A.12: Counts of the signal and background, exposure and energy dispersion of the stacked 1D Boomerang SNR dataset for the Tail region. Counts are plotted against the reconstructed energy, the exposure in terms of the true energy and the energy dispersion is given as a matrix relating true and reconstructed energy.

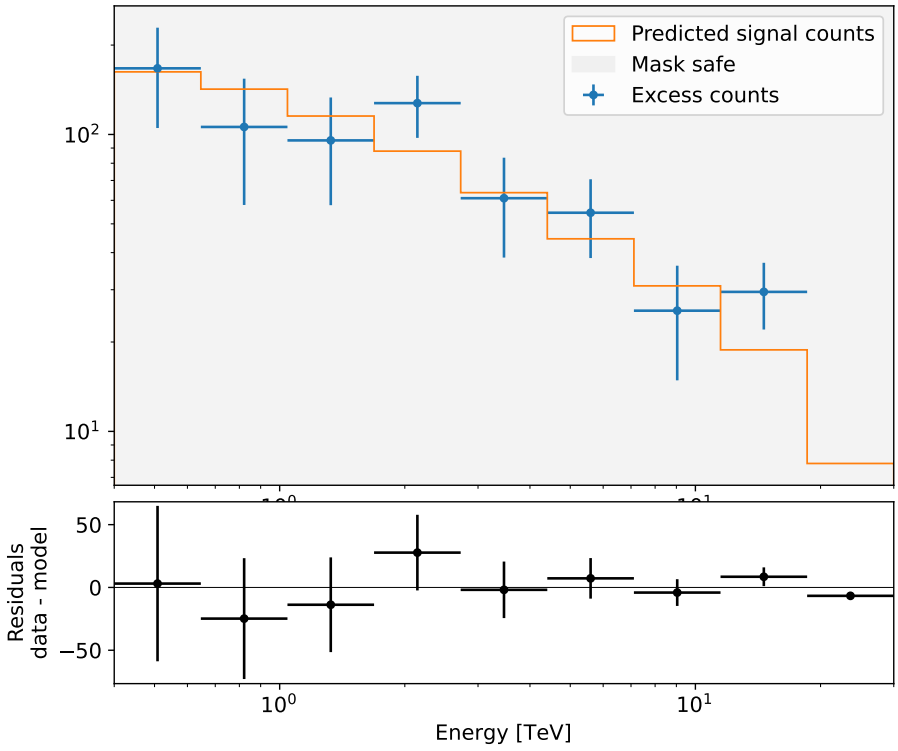

Figure A.13: Measured and predicted signal counts from the 1D analysis of the Boomerang SNR Tail against reconstructed energy. Predicted signal counts from the fitted spectral model are rendered in orange, measured counts in blue. The gray region indicates a safe range of the data as defined by the safe mask. The bottom panel displays the difference between the data and the applied model. The last data point is missing here due to too low statistics.

Spectral and Spatial Fitting - Crab Nebula

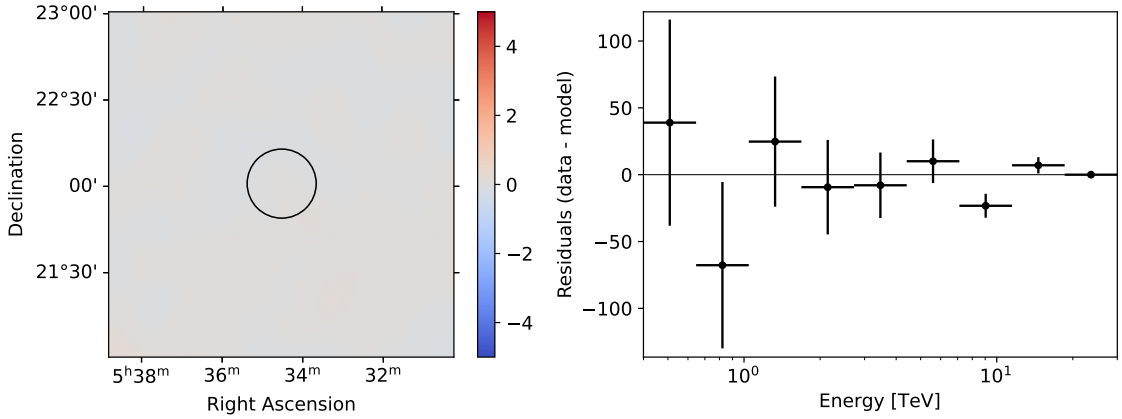

Figure A.14: Spectral residuals of a 3D Gaussian fit of Crab Nebula data. The left panel shows spatial residuals, superposed with a circular region of 0.2 ° size, from which the spectral information is extracted and plotted on the right panel.

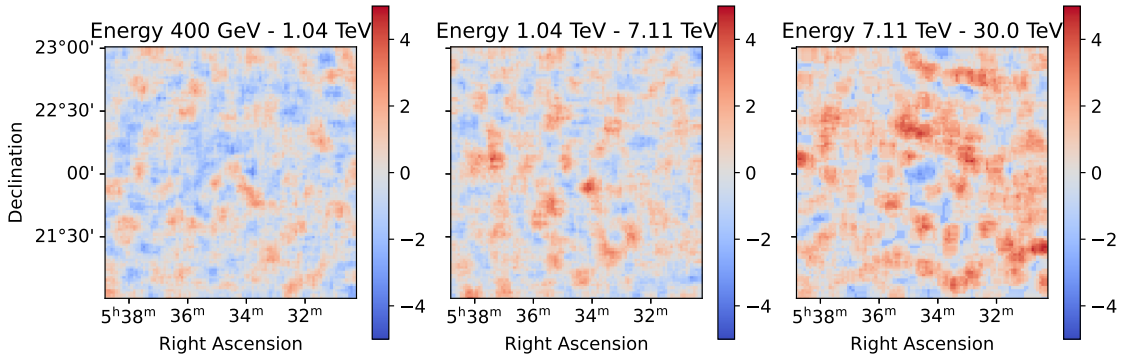

Figure A.15: Spatial residuals in the form of significance maps for a 3D Gaussian fit of Crab Nebula data, produced with the `ExcessMapEstimator` in three energy bins between 0.4 TeV and 30 TeV. There is no evident residual at the center of the fields.

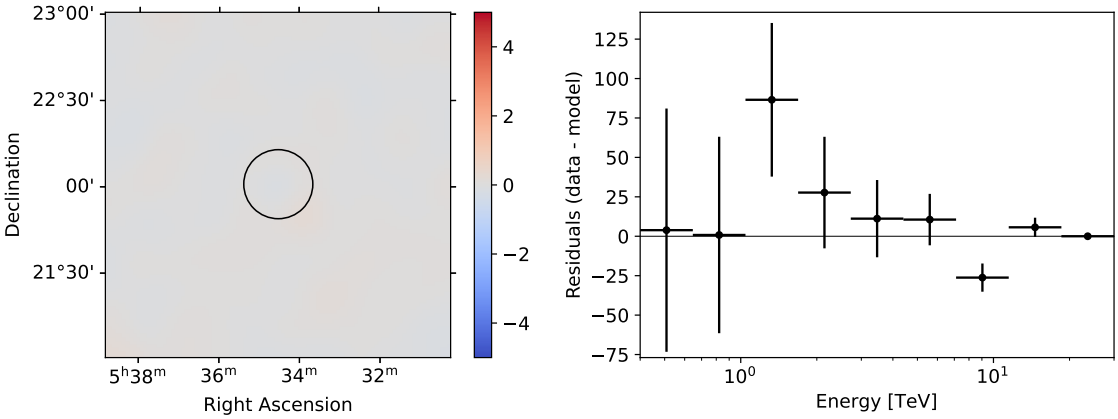

Figure A.16: Spectral residuals of a 3D point-like fit of Crab Nebula data. The left panel shows spatial residuals, superposed with a circular region of 0.2 ° size, from which the spectral information is extracted and plotted on the right panel.

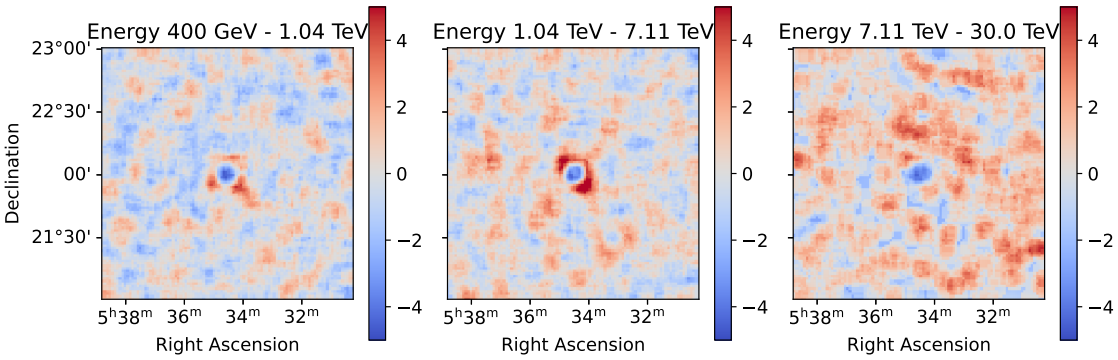

Figure A.17: Spatial residuals in the form of significance maps for a 3D point-like fit of Crab Nebula data, produced with the `ExcessMapEstimator` in three energy bins between 0.4 TeV and 30 TeV. All energy bins remain with an artifact at the position of the Crab Nebula, with the signal from a central spot being underestimated and the signal from its close surroundings being overestimated.

Spectral and Spatial Fitting - Boomerang SNR

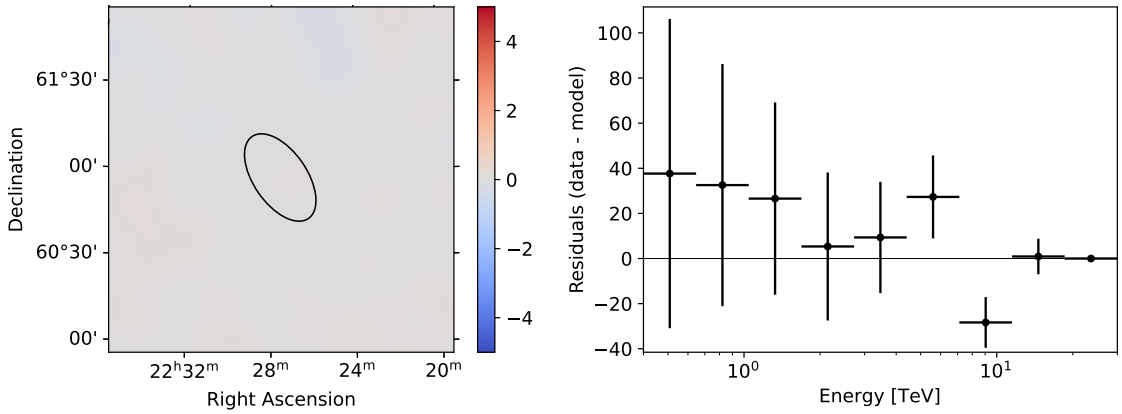

Figure A.18: Spectral residuals of a 3D asymmetric Gaussian fit of Boomerang SNR data. The left panel shows spatial residuals, superposed with the elliptical region delineating the $1\,\sigma$ contour of the fitted spatial model, from which the spectral information is extracted and plotted on the right panel.

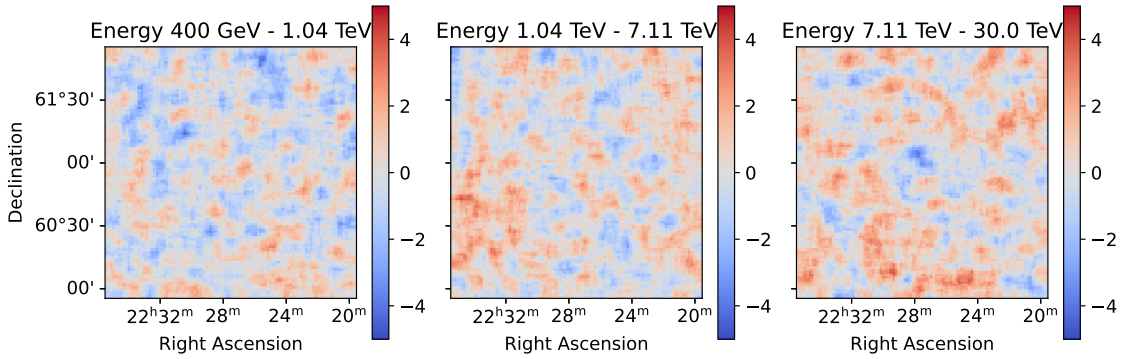

Figure A.19: Spatial residuals in the form of significance maps for a 3D asymmetric Gaussian fit of Boomerang SNR data, produced with the `ExcessMapEstimator` in three energy bins between 0.4 TeV and 30 TeV. No evident artifacts can be distinguished.

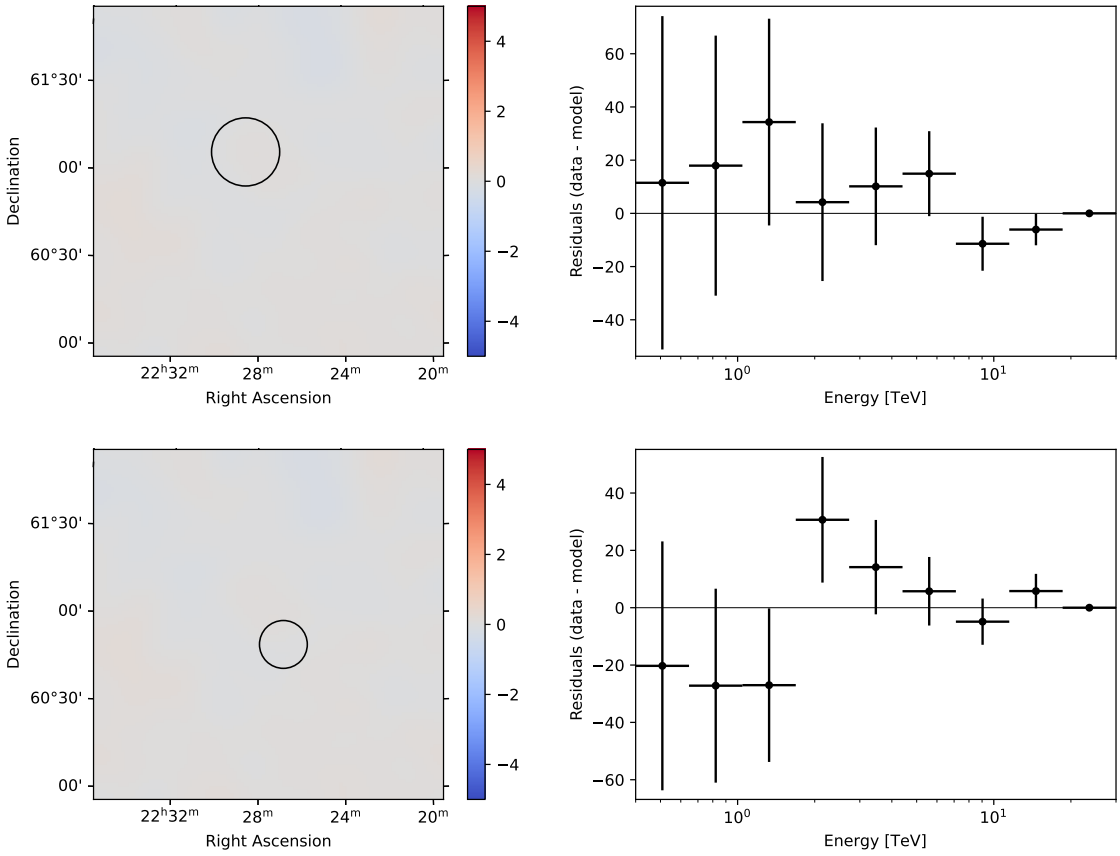

Figure A.20: Spectral residuals of a 3D double symmetric Gaussian fit (*1step*) of Boomerang SNR data. The top and bottom left panel show spatial residuals of the Head and the Tail region, respectively, superposed with the circular regions delineating the $1\,\sigma$ contour of the fitted spatial model, from which the spectral information is extracted and plotted on the top and bottom right panel.

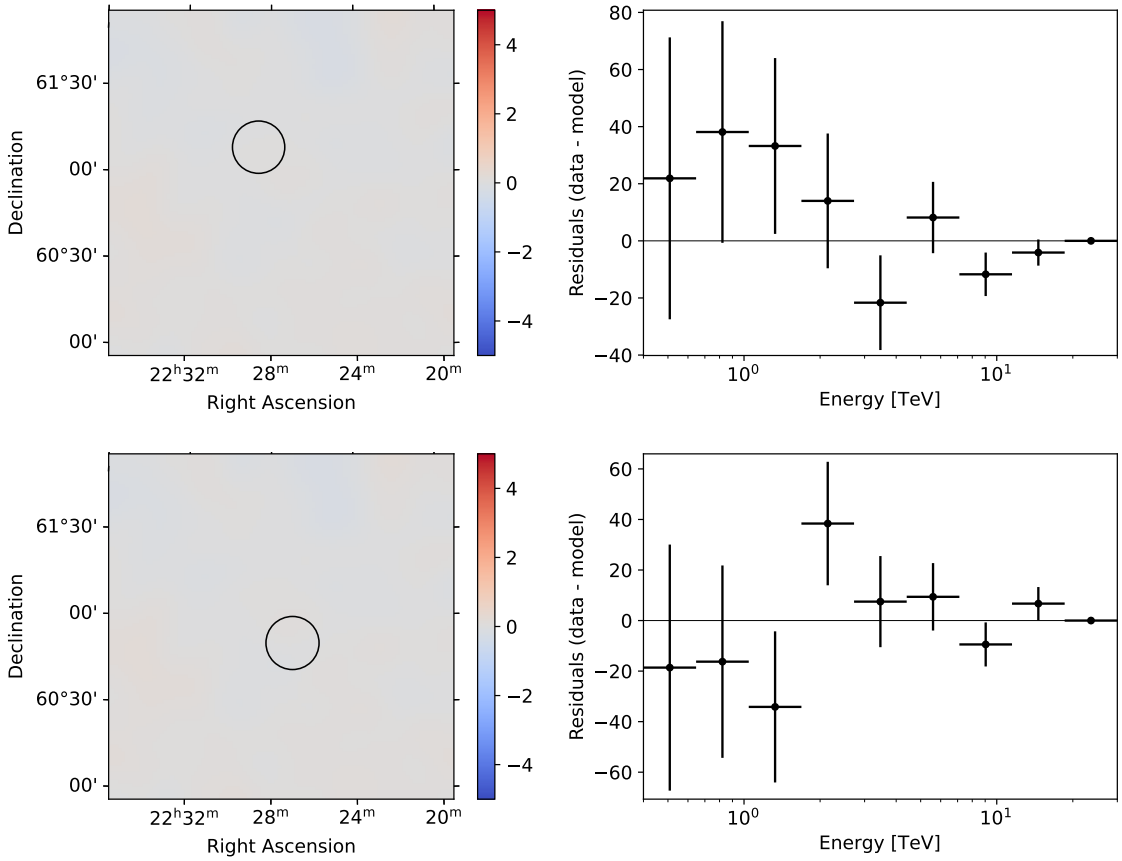

Figure A.21: Spectral residuals of a 3D double symmetric Gaussian fit (*2step*) of Boomerang SNR data. The top and bottom left panel show spatial residuals of the Head and the Tail region, respectively, superposed with the circular regions delineating the $1\,\sigma$ contour of the fitted spatial model, from which the spectral information is extracted and plotted on the top and bottom right panel.

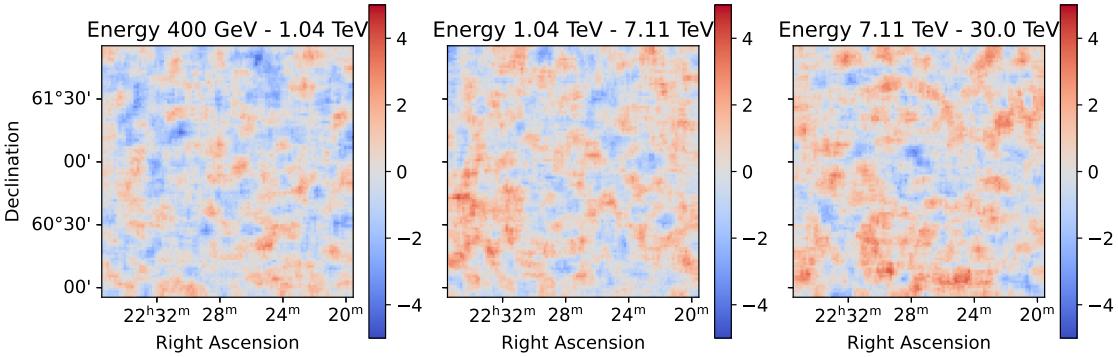

Figure A.22: Spatial residuals in the form of significance maps for a 3D double symmetric Gaussian fit (*1step*) of Boomerang SNR data, produced with the `ExcessMapEstimator` in three energy bins between 0.4 TeV and 30 TeV. No evident artifacts can be distinguished.

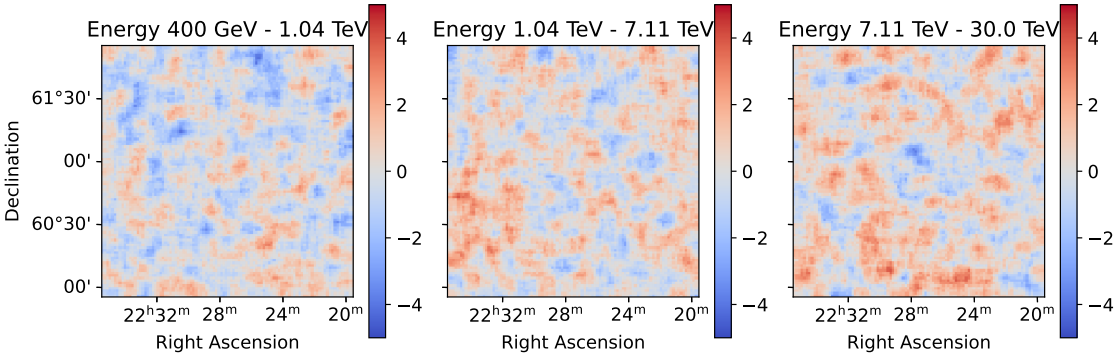

Figure A.23: Spatial residuals in the form of significance maps for a 3D double symmetric Gaussian fit (*2step*) of Boomerang SNR data, produced with the `ExcessMapEstimator` in three energy bins between 0.4 TeV and 30 TeV. No evident artifacts can be distinguished.

Bibliography

[1] G. Aad et al. "Observation of a new particle in the search for the Standard Model Higgs boson with the ATLAS detector at the LHC". In: *Physics Letters B* 716.1 (2012), pp. 1–29. DOI: 10.1016/j.physletb.2012.08.020. arXiv: 1207.7214.

[2] A. A. Abdo et al. "TeV Gamma-Ray Sources from a Survey of the Galactic Plane with Milagro". In: ApJ 664.2 (2007), pp. L91–L94. DOI: 10.1086/520717. arXiv: 0705.0707 [astro-ph].

[3] A. A. Abdo et al. "Fermi Large Area Telescope Detection of Pulsed γ-rays from the Vela-like Pulsars PSR J1048-5832 and PSR J2229+6114". In: ApJ 706.2 (2009), pp. 1331–1340. DOI: 10.1088/0004-637X/706/2/1331. arXiv: 0910.2249 [astro-ph.HE].

[4] A. A. Abdo et al. "Milagro Observations of Multi-TeV Emission from Galactic Sources in the Fermi Bright Source List". In: ApJ 700.2 (2009), pp. L127–L131. DOI: 10.1088/0004-637X/700/2/L127. arXiv: 0904.1018 [astro-ph.HE].

[5] V. A. Acciari et al. "Detection of Extended VHE Gamma Ray Emission from G106.3+2.7 with Veritas". In: ApJ 703.1 (2009), pp. L6–L9. DOI: 10.1088/0004-637X/703/1/L6. arXiv: 0911.4695 [astro-ph.HE].

[6] M. Ackermann et al. "The Search for Spatial Extension in High-latitude Sources Detected by the Fermi Large Area Telescope". In: ApJS 237.2 (2018), p. 32. DOI: 10.3847/1538-4365/aacdf7. arXiv: 1804.08035 [astro-ph.HE].

[7] F. Aharonian et al. "Spectrum and extension of the inverse-Compton emission of the Crab Nebula from a combined Fermi-LAT and H.E.S.S. analysis". In: *arXiv e-prints* (2024). DOI: 10.48550/arXiv.2403.12608. arXiv: 2403.12608 [astro-ph.HE].

[8] H. Akaike. "Information Theory and an Extension of the Maximum Likelihood Principle". In: *Selected Papers of Hirotugu Akaike*. Springer New York, 1998, pp. 199–213. ISBN: 978-1-4612-1694-0. DOI: 10.1007/978-1-4612-1694-0_15. URL: https://doi.org/10.1007/978-1-4612-1694-0_15.

[9] A. Albert et al. "Science Case for a Wide Field-of-View Very-High-Energy Gamma-Ray Observatory in the Southern Hemisphere". In: *arXiv e-prints* (2019). DOI: 10.48550/arXiv.1902.08429. arXiv: 1902.08429 [astro-ph.HE].

[10] A. Albert et al. "HAWC J2227+610 and Its Association with G106.3+2.7, a New Potential Galactic PeVatron". In: ApJ 896.2 (2020), p. L29. DOI: 10.3847/2041-8213/ab96cc. arXiv: 2005.13699 [astro-ph.HE].

[11] J. Albert et al. "VHE γ-Ray Observation of the Crab Nebula and its Pulsar with the MAGIC Telescope". In: ApJ 674.2 (2008), pp. 1037–1055. DOI: 10.1086/525270. arXiv: 0705.3244 [astro-ph].

[12] J. Aleksić et al. "Observations of the Crab Pulsar between 25 and 100 GeV with the MAGIC I Telescope". In: ApJ 742.1 (2011), p. 43. DOI: 10.1088/0004-637X/742/1/43. arXiv: 1108.5391 [astro-ph.HE].

[13] J. Aleksić et al. "Performance of the MAGIC stereo system obtained with Crab Nebula data". In: *Astroparticle Physics* 35.7 (2012), pp. 435–448. DOI: 10.1016/j.astropartphys.2011.11.007. arXiv: 1108.1477 [astro-ph.IM].

[14] J. Aleksić et al. "The major upgrade of the MAGIC telescopes, Part I: The hardware improvements and the commissioning of the system". In: *Astroparticle Physics* 72 (2016), pp. 61–75. DOI: 10.1016/j.astropartphys.2015.04.004. arXiv: 1409.6073 [astro-ph.IM].

[15] J. Aleksić et al. "The major upgrade of the MAGIC telescopes, Part II: A performance study using observations of the Crab Nebula". In: *Astroparticle Physics* 72 (2016), pp. 76–94. DOI: 10.1016/j.astropartphys.2015.02.005. arXiv: 1409.5594 [astro-ph.IM].

[16] M. Amenomori et al. "First Detection of sub-PeV Diffuse Gamma Rays from the Galactic Disk: Evidence for Ubiquitous Galactic Cosmic Rays beyond PeV Energies". In: Phys. Rev. Lett. 126.14 (2021), p. 141101. DOI: 10.1103/PhysRevLett.126.141101. arXiv: 2104.05181 [astro-ph.HE].

[17] W. B. Atwood et al. "The Large Area Telescope on the Fermi Gamma-Ray Space Telescope Mission". In: ApJ 697.2 (2009), pp. 1071–1102. DOI: 10.1088/0004-637X/697/2/1071. arXiv: 0902.1089 [astro-ph.IM].

[18] A. Bamba and B. J. Williams. "Supernova Remnants: Types and Evolution". In: *Handbook of X-ray and Gamma-ray Astrophysics*. 2022, p. 77. DOI: 10.1007/978-981-16-4544-0_88-1.

[19] Y. Bao et al. "PeVatron candidate SNR G106.3+2.7 in a low-density cavity: a multiwavelength test". In: MNRAS 528.4 (2024), pp. 5487–5494. DOI: 10.1093/mnras/stae058. arXiv: 2401.02654 [astro-ph.HE].

[20] J. A. Barrio. *The MAGIC telescope design report*. Tech. rep. MPI Institute Report MPI-PhE/98-5. Max Planck Institute for Physics (MPI), Munich, 1998.

[21] D. Berge, S. Funk, and J. Hinton. "Background modelling in very-high-energy γ-ray astronomy". In: A&A 466.3 (2007), pp. 1219–1229. DOI: 10.1051/0004-6361:20066674. arXiv: astro-ph/0610959 [astro-ph].

[22] A. Biland et al. "The Active Mirror Control of the MAGIC Telescopes". In: *International Cosmic Ray Conference*. Vol. 3. International Cosmic Ray Conference. 2008, pp. 1353–1356. DOI: 10.48550/arXiv.0709.1574. arXiv: 0709.1574 [astro-ph].

[23] M. Bitossi, R. Paoletti, and D. Tescaro. "Ultra-Fast Sampling and Data Acquisition Using the DRS4 Waveform Digitizer". In: *IEEE Transactions on Nuclear Science* 63.4 (2016), pp. 2309–2316. DOI: 10.1109/TNS.2016.2578963.

[24] T. Bretz et al. "The drive system of the major atmospheric gamma-ray imaging Cherenkov telescope". In: *Astroparticle Physics* 31.2 (2009), pp. 92–101. DOI: 10.1016/j.astropartphys.2008.12.001. arXiv: 0810.4593 [astro-ph].

[25] R. Brun and F. Rademakers. "ROOT: An object oriented data analysis framework". In: *Nucl. Instrum. Meth. A* 389 (1997), pp. 81–86. DOI: 10.1016/S0168-9002(97)00048-X. URL: https://root.cern/.

[26] N. Bucciantini and R. Bandiera. "Pulsar bow-shock nebulae. I. Physical regimes and detectability conditions". In: A&A 375 (2001), pp. 1032–1039. DOI: 10.1051/0004-6361:20010900.

[27] E. M. Cackett, M. C. Bentz, and E. Kara. "Reverberation mapping of active galactic nuclei: from X-ray corona to dusty torus". In: *iScience* 24.6 (2021), p. 102557. DOI: 10.1016/j.isci.2021.102557. arXiv: 2105.06926 [astro-ph.GA].

[28] Z. Cao, D. della Volpe, and S. Liu. "The Large High Altitude Air Shower Observatory (LHAASO) Science Book (2021 Edition)". In: *arXiv e-prints* (2019). DOI: 10.48550/arXiv.1905.02773. arXiv: 1905.02773 [astro-ph.HE].

[29] Z. Cao et al. "Ultrahigh-energy photons up to 1.4 petaelectronvolts from 12 γ-ray Galactic sources". In: Nature 594.7861 (2021), pp. 33–36. DOI: 10.1038/s41586-021-03498-z.

[30] Z. Cao et al. "The First LHAASO Catalog of Gamma-Ray Sources". In: ApJS 271.1 (2024), p. 25. DOI: 10.3847/1538-4365/acfd29. arXiv: 2305.17030 [astro-ph.HE].

[31] Zhen Cao et al. "Measurement of Ultra-High-Energy Diffuse Gamma-Ray Emission of the Galactic Plane from 10 TeV to 1 PeV with LHAASO-KM2A". In: Phys. Rev. Lett. 131.15 (2023), p. 151001. DOI: 10.1103/PhysRevLett.131.151001. arXiv: 2305.05372 [astro-ph.HE].

[32] P. A. Čerenkov. "Visible Radiation Produced by Electrons Moving in a Medium with Velocities Exceeding that of Light". In: *Physical Review* 52.4 (1937), pp. 378–379. DOI: 10.1103/PhysRev.52.378.

[33] G. Ceribella. "Insights into the 10-100 GeV gamma-ray emission of pulsars from extensive observations of MAGIC". PhD thesis. Technical University Munich, 2021. URL: https://mediatum.ub.tum.de/?id=1617483.

[34] Cherenkov Telescope Array Consortium et al. *Science with the Cherenkov Telescope Array*. 2019. DOI: 10.1142/10986. arXiv: 1709.07997 [astro-ph.HE].

[35] G. Cocconi. "Influence of the Earth's Magnetic Field on the Extensive Air Showers". In: *Phys. Rev.* 93 (3 1954), pp. 646–647. DOI: 10.1103/PhysRev.93.646.2.

[36] J. L. Contreras et al. "Data model issues in the Cherenkov Telescope Array project". In: *34th International Cosmic Ray Conference (ICRC2015)*. Vol. 34. International Cosmic Ray Conference. 2015, p. 960. DOI: 10.22323/1.236.0960. arXiv: 1508.07584 [astro-ph.IM].

[37] *Data Formats for Gamma-ray Astronomy. GitHub Repository.* (accessed on 9 April 2024). URL: https://github.com/open-gamma-ray-astro/gamma-astro-data-formats.

[38] *Data Formats for Gamma-ray Astronomy. Online Documentation.* (accessed on 9 April 2024). URL: https://gamma-astro-data-formats.readthedocs.io/.

[39] A. De Sarkar et al. "LHAASO J2226+6057 as a pulsar wind nebula". In: A&A 668 (2022), A23. DOI: 10.1051/0004-6361/202244841. arXiv: 2209.13285 [astro-ph.HE].

[40] C. Deil et al. "Open high-level data formats and software for gamma-ray astronomy". In: *6th International Symposium on High Energy Gamma-Ray Astronomy*. Vol. 1792. American Institute of Physics Conference Series 070006. AIP, 2017. DOI: 10.1063/1.4969003. arXiv: 1610.01884 [astro-ph.IM].

[41] A. Donath et al. "Gammapy: A Python package for gamma-ray astronomy". In: A&A 678.A157 (2023). DOI: 10.1051/0004-6361/202346488. arXiv: 2308.13584.

[42] C. Evoli. *The Cosmic-Ray Energy Spectrum*. 2023. DOI: 10.5281/zenodo.7948212. URL: https://zenodo.org/records/7948212.

[43] K. Fang et al. "Evidence for PeV Proton Acceleration from Fermi-LAT Observations of SNR G 106.3 +2.7". In: Phys. Rev. Lett. 129.7 (2022), p. 071101. DOI: 10.1103/PhysRevLett.129.071101. arXiv: 2208.05457 [astro-ph.HE].

[44] E. Fermi. "Galactic Magnetic Fields and the Origin of Cosmic Radiation." In: ApJ 119 (1954), p. 1. DOI: 10.1086/145789.

[45] Enrico Fermi. "On the Origin of the Cosmic Radiation". In: *Physical Review* 75.8 (1949), pp. 1169–1174. DOI: 10.1103/PhysRev.75.1169.

[46] M. V. Fernandes et al. "A new method of reconstructing VHE γ-ray spectra: the Template Background Spectrum". In: A&A 568 (2014), A117. DOI: 10.1051/0004-6361/201323156. arXiv: 1407.0925 [astro-ph.IM].

[47] C. Fruck et al. "A novel LIDAR-based Atmospheric Calibration Method for Improving the Data Analysis of MAGIC". In: *arXiv e-prints* (2014). DOI: 10.48550/arXiv.1403.3591. arXiv: 1403.3591 [astro-ph.IM].

[48] Y. Fujita et al. "X-Ray Emission from the PeVatron-candidate Supernova Remnant G106.3+2.7". In: ApJ 912.2, 133 (2021), p. 133. DOI: 10.3847/1538-4357/abf14a. arXiv: 2101.10329 [astro-ph.HE].

[49] E. Furst et al. "A radio continuum survey of the Galactic Plane at 11 cmwavelength. III. The area 76deg <= L <= 240deg, -5deg <= B <= 5deg". In: A&AS 85 (Oct. 1990), pp. 691–803.

[50] T. K. Gaisser, R. Engel, and E. Resconi. *Cosmic Rays and Particle Physics*. 2nd ed. Cambridge University Press, 2016.

[51] T. K. Gaisser and A. M. Hillas. "Reliability of the Method of Constant Intensity Cuts for Reconstructing the Average Development of Vertical Showers". In: *International Cosmic Ray Conference*. Vol. 8. International Cosmic Ray Conference. 1977, p. 353.

[52] W. Galbraith and J. V. Jelley. "Light Pulses from the Night Sky associated with Cosmic Rays". In: Nature 171.4347 (1953), pp. 349–350. DOI: 10.1038/171349a0.

[53] *Gammapy. GitHub Repository.* (accessed on 24 April 2024). URL: https://github.com/gammapy/.

[54] *Gammapy. Online Documentation.* (accessed on 8 May 2024). URL: https://docs.gammapy.org/.

[55] C. Ge et al. "Revealing a peculiar supernova remnant G106.3+2.7 as a peta-electronvolt proton accelerator with X-ray observations". In: *The Innovation* 2 (2021), p. 100118. DOI: 10.1016/j.xinn.2021.100118. arXiv: 2012.11531 [astro-ph.HE].

[56] H. E. S. S. Collaboration. "Resolving the Crab pulsar wind nebula at teraelectronvolt energies". In: *Nature Astronomy* 4 (2020), pp. 167–173. DOI: 10.1038/s41550-019-0910-0. arXiv: 1909.09494 [astro-ph.HE].

[57] J. P. Halpern et al. "A Possible X-Ray and Radio Counterpart of the High-Energy Gamma-Ray Source 3EG J2227+6122". In: ApJ 547.1 (2001), pp. 323–333. DOI: 10.1086/318361. arXiv: astro-ph/0007076 [astro-ph].

[58] J. P. Halpern et al. "PSR J2229+6114: Discovery of an Energetic Young Pulsar in the Error Box of the EGRET Source 3EG J2227+6122". In: ApJ 552.2 (2001), pp. L125–L128. DOI: 10.1086/320347. arXiv: astro-ph/0104109 [astro-ph].

[59] R. C. Hartman et al. "The Third EGRET Catalog of High-Energy Gamma-Ray Sources". In: ApJS 123.1 (1999), pp. 79–202. DOI: 10.1086/313231.

[60] D. Heck et al. *CORSIKA: a Monte Carlo code to simulate extensive air showers.* 1998.

[61] V. F. Hess. "Über Beobachtungen der durchdringenden Strahlung bei sieben Freiballonfahrten". In: *Phys. Z.* 13 (1912), pp. 1084–1091.

[62] P. W. Higgs. "Broken Symmetries and the Masses of Gauge Bosons". In: Phys. Rev. Lett. 13.16 (1964), pp. 508–509. DOI: 10.1103/PhysRevLett.13.508.

[63] A. M. Hillas. "Cerenkov Light Images of EAS Produced by Primary Gamma Rays and by Nuclei". In: *19th International Cosmic Ray Conference (ICRC19).* Vol. 3. International Cosmic Ray Conference. 1985, p. 445. URL: https://ui.adsabs.harvard.edu/abs/1985ICRC....3..445H.

[64] J. A. Hinton and HESS Collaboration. "The status of the HESS project". In: New A Rev. 48.5-6 (2004), pp. 331–337. DOI: 10.1016/j.newar.2003.12.004. arXiv: astro-ph/0403052 [astro-ph].

[65] P. Huentemeyer et al. "The Southern Wide-Field Gamma-Ray Observatory (SWGO): A Next-Generation Ground-Based Survey Instrument". In: *Bulletin of the American Astronomical Society.* Vol. 51. 2019, p. 109. DOI: 10.48550/arXiv.1907.07737. arXiv: 1907.07737 [astro-ph.IM].

[66] G. Joncas and L. A. Higgs. "The DRAO galactic-plane survey. II. Field at l= 105." In: A&AS 82 (1990), pp. 113–144. URL: https://ui.adsabs.harvard.edu/abs/1990A&AS...82..113J.

[67] E. Kallas and W. Reich. "A 21 cm radio continuum survey of the galactic plane between l = 93 and l = 162." In: A&AS 42 (1980), pp. 227–243. URL: https://ui.adsabs.harvard.edu/abs/1980A&AS...42..227K.

[68] R. Kothes, W. Reich, and B. Uyanıker. "The Boomerang PWN G106.6+2.9 and the Magnetic Field Structure in Pulsar Wind Nebulae". In: ApJ 638.1 (2006), pp. 225–233. DOI: 10.1086/498666.

[69] R. Kothes, B. Uyaniker, and S. Pineault. "The Supernova Remnant G106.3+2.7 and Its Pulsar-Wind Nebula: Relics of Triggered Star Formation in a Complex Environment". In: ApJ 560.1 (2001), pp. 236–243. DOI: 10.1086/322511. arXiv: astro-ph/0106270 [astro-ph].

[70] T. -P. Li and Y. -Q. Ma. "Analysis methods for results in gamma-ray astronomy." In: ApJ 272 (1983), pp. 317–324. DOI: 10.1086/161295.

[71] X. Liang et al. "A PeVatron Candidate: Modeling the Boomerang Nebula in X-ray Band". In: *Universe* 8.10 (2022), p. 547. DOI: 10.3390/universe8100547. arXiv: 2209.03809 [astro-ph.HE].

[72] Q. Liu, P. Zhou, and Y. Chen. "IRAM 30 m CO-line Observation toward the PeVatron Candidate G106.3+2.7: Direct Interaction between the Shock and the Molecular Cloud Remains Uncertain". In: ApJ 926.2 (2022), p. 124. DOI: 10.3847/1538-4357/ac3fb3. arXiv: 2112.01101 [astro-ph.GA].

[73] S. Liu et al. "Hadronic versus Leptonic Models for γ-Ray Emission from VER J2227+608". In: ApJ 897.2 (2020), p. L34. DOI: 10.3847/2041-8213/ab9ff2. arXiv: 2006.14946 [astro-ph.HE].

[74] M. S. Longair. *High Energy Astrophysics*. 3rd edn. Cambridge University Press, 2011. ISBN: 978-0521756181.

[75] MAGIC Collaboration et al. "Teraelectronvolt emission from the γ-ray burst GRB 190114C". In: Nature 575.7783 (2019), pp. 455–458. DOI: 10.1038/s41586-019-1750-x. arXiv: 2006.07249 [astro-ph.HE].

[76] MAGIC Collaboration et al. "MAGIC observations provide compelling evidence of hadronic multi-TeV emission from the putative PeVatron SNR G106.3+2.7". In: A&A 671 (2023), A12. DOI: 10.1051/0004-6361/202244931. arXiv: 2211.15321 [astro-ph.HE].

[77] J. R. Mattox et al. "The Likelihood Analysis of EGRET Data". In: ApJ 461 (1996), p. 396. DOI: 10.1086/177068.

[78] S. Mender. "Spectral and Spatial Analysis of MAGIC Telescope Data in a Standardized Format". PhD thesis. Technical University Dortmund, 2023. URL: https://tu-dortmund.sciebo.de/s/ouiPepfhSA9AgR3.

[79] S. Mender et al. "Computing sky maps using the open-source package Gammapy and MAGIC data in a standardized format". In: *arXiv e-prints* (2023). arXiv: 2302.11285 [astro-ph.IM].

[80] R. Mirzoyan. "First time detection of a GRB at sub-TeV energies; MAGIC detects the GRB 190114C". In: *The Astronomer's Telegram* 12390 (2019), p. 1.

[81] L. Mohrmann et al. "Validation of open-source science tools and background model construction in γ-ray astronomy". In: A&A 632, A72 (2019), A72. DOI: 10.1051/0004-6361/201936452. arXiv: 1910.08088 [astro-ph.IM].

[82] A. Moralejo et al. "MARS, the MAGIC Analysis and Reconstruction Software". In: *arXiv e-prints* (2009). DOI: 10.48550/arXiv.0907.0943. arXiv: 0907.0943 [astro-ph.IM].

[83] A. Neronov and D. Semikoz. "Galactic diffuse gamma-ray emission at TeV energy". In: A&A 633 (2020), A94. DOI: 10.1051/0004-6361/201936368. arXiv: 1907.06061 [astro-ph.HE].

[84] C. Nigro. "Study of Persistent and Flaring Gamma-Ray Emission from Active Galactic Nuclei with the MAGIC Telescopes and Prospects for Future Open Data Formats in Gamma-Ray Astronomy". PhD thesis. Humboldt-Universität zu Berlin, 2019. URL: https://edoc.hu-berlin.de/bitstream/handle/18452/21335/dissertation_nigro_cosimo.pdf.

[85] C. Nigro. "Establishing the MAGIC data legacy: adopting standardised data formats and open-source analysis tools". In: *Proceedings of 7th Heidelberg International Symposium on High-Energy Gamma-Ray Astronomy — PoS(Gamma2022)*. Vol. 417. 2023, p. 122. arXiv: 2302.13615 [astro-ph.IM].

[86] C. Nigro, T. Hassan, and L. Olivera-Nieto. "Evolution of Data Formats in Very-High-Energy Gamma-Ray Astronomy". In: *Universe* 7.10 (2021), p. 374. DOI: 10.3390/universe7100374. arXiv: 2109.14661 [astro-ph.IM].

[87] B. Olmi and N. Bucciantini. "The Dawes Review 11: From young to old: The evolutionary path of Pulsar Wind Nebulae". In: PASA 40 (2023), e007. DOI: 10.1017/pasa.2023.5. arXiv: 2301.12903 [astro-ph.HE].

[88] S. Pineault and G. Joncas. "G106.3+2.7: A Supernova Remnant in a Late Stage of Evolution". In: AJ 120.6 (2000), pp. 3218–3225. DOI: 10.1086/316863.

[89] I. Pope et al. "A Multiwavelength Investigation of PSR J2229+6114 and its Pulsar Wind Nebula in the Radio, X-Ray, and Gamma-Ray Bands". In: ApJ 960.1 (2024), p. 75. DOI: 10.3847/1538-4357/ad0120. arXiv: 2310.04512 [astro-ph.HE].

[90] E. Prandini et al. "Study of hadron and gamma-ray acceptance of the MAGIC telescopes: towards an improved background estimation ". In: *Proceedings of The 34th International Cosmic Ray Conference — PoS(ICRC2015)*. Vol. 236. 2016, p. 721. DOI: 10.22323/1.236.0721.

[91] S. P. Reynolds and R. A. Chevalier. "Evolution of pulsar-driven supernova remnants." In: ApJ 278 (1984), pp. 630–648. DOI: 10.1086/161831.

[92] T. M. Shaffer, E. C. Pratt, and J. Grimm. "Utilizing the power of Cerenkov light with nanotechnology". In: *Nature Nanotechnology* 12.2 (2017), pp. 106–117. DOI: 10.1038/nnano.2016.301.

[93] G. Sinnis, A. Smith, and J. E. McEnery. "Hawc:. a Next Generation All-Sky VHE Gamma-Ray Telescope". In: *The Tenth Marcel Grossmann Meeting. On recent developments in theoretical and experimental general relativity, gravitation*

and relativistic field theories. 2006, p. 1068. DOI: 10.1142/9789812704030_0066. arXiv: astro-ph/0403096 [astro-ph].

[94] J. Sitarek et al. "Analysis techniques and performance of the Domino Ring Sampler version 4 based readout for the MAGIC telescopes". In: *Nuclear Instruments and Methods in Physics Research A* 723 (2013), pp. 109–120. DOI: 10.1016/j.nima.2013.05.014. arXiv: 1305.1007 [astro-ph.IM].

[95] M. Spurio. *Probes of Multimessenger Astrophysics. Charged cosmic rays, neutrinos, γ-rays and gravitational waves*. Astronomy and Astrophysics Library. Springer Cham, 2018. ISBN: 978-3-319-96853-7. DOI: 10.1007/978-3-319-96854-4.

[96] M. C. Strzys. "Deciphering the γ-Ray Sky Study of the γ-Cygni SNR using a novel Likelihood Analysis Technique for the MAGIC Telescopes". PhD thesis. Ludwig-Maximilians-University Munich, 2019. URL: https://edoc.ub.uni-muenchen.de/26997/7/Strzys_Marcel_Constantin.pdf.

[97] M. C. Strzys. "Skymaps". Presentation at the 9th MAGIC Software School, MAGIC Collaboration. 2023.

[98] M. C. Strzys et al. "Pybkgmodel - a background modelling toolbox for the CTA". In: *Proceedings of 38th International Cosmic Ray Conference — PoS(ICRC2023)*. Vol. 444. 2023, p. 894. DOI: 10.22323/1.444.0894.

[99] A. R. Taylor et al. "The Canadian Galactic Plane Survey". In: AJ 125.6 (2003), pp. 3145–3164. DOI: 10.1086/375301.

[100] Tibet ASγ Collaboration et al. "Potential PeVatron supernova remnant G106.3+2.7 seen in the highest-energy gamma rays". In: *Nature Astronomy* 5 (2021), pp. 460–464. DOI: 10.1038/s41550-020-01294-9. arXiv: 2109.02898 [astro-ph.HE].

[101] C. M. Urry and P. Padovani. "Unified Schemes for Radio-Loud Active Galactic Nuclei". In: PASP 107 (1995), p. 803. DOI: 10.1086/133630. arXiv: astro-ph/9506063 [astro-ph].

[102] I. Vovk, M. Strzys, and C. Fruck. "A spatial likelihood analysis for MAGIC telescope data: From instrument response modelling to spectral extraction". In: A&A 619 (2018), A7. DOI: 10.1051/0004-6361/201833139. arXiv: 1806.03167 [astro-ph.IM].

[103] R. M. Wagner. "Measurement of very high energy gamma-ray emission from four blazars using the MAGIC telescope and a comparative blazar study". PhD thesis. Max-Planck-Institute for Physics, Munich, 2006. URL: http://mediatum.ub.tum.de/doc/604099/document.pdf.

[104] W. Wagner. PhD thesis. University of Dortmund (now Technical University), Dortmund, 2004.

[105] T. C. Weekes et al. "Observation of TeV Gamma Rays from the Crab Nebula Using the Atmospheric Cerenkov Imaging Technique". In: ApJ 342 (1989), p. 379. DOI: 10.1086/167599.

[106] T. C. Weekes et al. "VERITAS: the Very Energetic Radiation Imaging Telescope Array System". In: *Astroparticle Physics* 17.2 (2002), pp. 221–243. DOI: 10.1016/S0927-6505(01)00152-9. arXiv: astro-ph/0108478 [astro-ph].

[107] Y. Xin et al. "VER J2227+608: A Hadronic PeVatron Pulsar Wind Nebula?" In: ApJ 885.2 (2019), p. 162. DOI: 10.3847/1538-4357/ab48ee. arXiv: 1907.04972 [astro-ph.HE].

[108] R. Zanin. "MARS, the MAGIC analysis and reconstruction software". In: *Proceedings of The 34th International Cosmic Ray Conference — PoS(ICRC2013)*. 2013, p. 0773. URL: https://inspirehep.net/literature/1412925.

List of Figures

List of Tables

Acknowledgements

To begin with, I want to thank my family for everything they gave and are giving me.

Secondly, I would like to thank my internal supervisor Prof. Dr. Thomas Kuhr from the Ludwig-Maximilians-University (LMU) in Munich, who accepted to supervise a thesis from a different field in physics once more and nevertheless dedicated time to understand my work and provide feedback, and my external supervisor Dr. Franca Cassol from the Centre de Physique des Particules de Marseille (CPPM) in France, who is leading and coordinating the Boomerang project in MAGIC/LST and supervised this thesis. I acknowledge the time they dedicated to me and to the reading of my thesis in order to help improve it. I am very grateful to have worked and learned in the MAGIC/CTA group at the University of Padua, Italy, during my Erasmus study and master project. On this note, I want to thank Mosè Mariotti, Michele Doro and Elisa Prandini for establishing the first contact, welcoming me in the group for two years and for giving me many opportunities to explore what interests me, present my work, do outreach and travel during these two years. It does not go without saying to get these numerous opportunities, thank you!

I want to express my special thanks to David Green from Max Planck Institute for Physics (MPP) in Munich, who was always available for questions and advice, provided me with valuable insights about 3D analyses and managed to really motivate me by our discussions. I also would like to thank Cosimo Nigro, Shotaro Abe and Marcel Strzys, with each of whom I had several meetings to discuss details about the `gammapy` analysis and help me understand the methods of background estimation. Thank you for your willingness, kindness and availability to answer my questions.

For the review of this thesis and many valuable suggestions, I additionally have to thank Alexander Hahn, David Green, Ivana Batković, Lea Heckmann and Martin Will. The last days of writing a thesis can be intense, but there were two kind people who supported me during these last days, hosting me and making the conclusion smooth. I do not take it for granted. Thank you for this and for your friendship, Juli and Martin!

Then, thank you very much also to my colleagues and dear friends Lea Heckmann and

Alexander Hahn from MPP. Lea, you have been a constant guidance and support for me this last year, both in professional and personal ways, and I am very thankful for that. Alex, same goes for you, thank you for always showing interest in what I do, helping with so many little things during my master work and always encouraging me.

Ivana Batković, I do not know how I would have survived this year without you as a colleague and dear friend, thank you for being who you are, always being there for me when I need it and for all the fun we had together. I will miss you.

Now, let me also thank the people inside the MAGIC and LST collaborations and at the workplace, who were not only available but happy to help, answer questions, enjoy science and time together and who made my experience during the master easier, enjoyable and unforgettable. This includes people I have met at general meetings and on shift and especially some people from the high-energy astrophysics group in Padua. One of the things I value most about the colleagues who became friends, is their humor. I will miss laughing and joking with them and I am grateful to have found such an atmosphere at the workplace, because it is not obvious. Thank you to Ivana, Joao, Arshia, Giuseppe, Ilaria, Cornelia, Sarah, Michela, Stella and Sara!

Lastly, I want to thank all the people who are important to me and made my life richer this year: Bianca, Veronika, Maja, Anna, Federico, Francesca, Angelo, Felix, Carla and Tamara, Janina, my many friends from the Bavarian Public Observatory in Munich, and many more...

Declaration of Authorship

I, Marine Pihet, hereby declare with my signature that I have composed the presented thesis independently on my own and without any other resources than the ones indicated. All parts that are taken from the specified references in exact wording or content are marked as such.

The presented thesis has not been submitted as scientific work in similar or same manner before.

Ich, Marine Pihet, erkläre hiermit durch meine eigenhändige Unterschrift, die vorliegende Arbeit selbständig verfasst zu haben und keine anderen als die angegebenen Quellen und Hilfsmittel verwendet zu haben. Alle Stellen, die wörtlich oder inhaltlich den angegebenen Quellen entnommen wurden, sind als solche kenntlich gemacht.

Die vorliegende Arbeit wurde bisher in gleicher oder ähnlicher Form noch nicht als wissenschaftliche Arbeit eingereicht.

Munich, June 9, 2024

Marine Pihet